DARK MATTER AND NEW FUNDAMENTAL PHYSICS

By
ARPAN KAR
PHYS08201504001

Harish-Chandra Research Institute, Prayagraj

A thesis submitted to the

Board of Studies in Physical Sciences

In partial fulfillment of requirements

for the Degree of

DOCTOR OF PHILOSOPHY

of

HOMI BHABHA NATIONAL INSTITUTE

April, 2021

Homi Bhabha National Institute[1]

Recommendations of the Viva Voce Committee

As members of the Viva Voce Committee, we certify that we have read the dissertation prepared by Arpan Kar entitled "*Dark Matter and New Fundamental Physics*" and recommend that it may be accepted as fulfilling the thesis requirement for the award of Degree of Doctor of Philosophy.

Chairman – Prof. Pinaki Majumdar	Pinaki Majumdar	**Date: 14-07-2021**
Guide / Convener – Prof. Santosh Kumar Rai		**Date: 14-07-2021**
Examiner – Prof. Ranjan Laha	Ranjan Laha	**Date: 14-07-2021**
Member 1- Prof. Asesh Krishna Datta		**Date: 14-07-2021**
Member 2- Prof. Anirban Basu	A. Basu	**Date: 14-07-2021**
Member 3- Prof. Prasenjit Sen	Prasenjit Sen	**Date: 14-07-2021**

Final approval and acceptance of this thesis is contingent upon the candidate's submission of the final copies of the thesis to HBNI.

I/We hereby certify that I/we have read this thesis prepared under my/our direction and recommend that it may be accepted as fulfilling the thesis requirement.

Date: 14.07.2021
Place: Prayagraj

Prof. Santosh Kumar Rai
Guide

[1] This page is to be included only for final submission after successful completion of viva voce.

STATEMENT BY AUTHOR

This dissertation has been submitted in partial fulfillment of requirements for an advanced degree at Homi Bhabha National Institute (HBNI) and is deposited in the Library to be made available to borrowers under rules of the HBNI.

Brief quotations from this dissertation are allowable without special permission, provided that accurate acknowledgement of source is made. Requests for permission for extended quotation from or reproduction of this manuscript in whole or in part may be granted by the Competent Authority of HBNI when in his or her judgment the proposed use of the material is in the interests of scholarship. In all other instances, however, permission must be obtained from the author.

Arpan Kar.

Arpan Kar

DECLARATION

I, hereby declare that the investigation presented in the thesis has been carried out by me. The work is original and has not been submitted earlier as a whole or in part for a degree / diploma at this or any other Institution / University.

Arpan Kar.

Arpan Kar

List of Publications arising from the thesis

Journal

1. "Can Square Kilometre Array phase 1 go much beyond the LHC in supersymmetry search?", Arpan Kar, Sourav Mitra, Biswarup Mukhopadhyaya, Tirthankar Roy Choudhury, *Phys. Rev. D(Rapid Communication)*, **2019**, *99*, 021302.

2. "Heavy dark matter particle annihilation in dwarf spheroidal galaxies: Radio signals at the SKA telescope", Arpan Kar, Sourav Mitra, Biswarup Mukhopadhyaya, Tirthankar Roy Choudhury, *Phys. Rev. D*, **2020**, *101*, 023015.

3. "Constraints on dark matter annihilation in dwarf spheroidal galaxies from low frequency radio observations", Arpan Kar, Sourav Mitra, Biswarup Mukhopadhyaya, Tirthankar Roy Choudhury, Steven Tingay, *Phys. Rev. D*, **2019**, *100*, 043002.

4. "Dark matter annihilation in ω Centauri: Astrophysical implications derived from the MWA radio data", Arpan Kar, Biswarup Mukhopadhyaya, Steven Tingay, Ben McKinley, Marjike Haverkorn, Sam McSweeney, Natasha Hurley-Walker, Sourav Mitra, Tirthankar Roy Choudhury, *Physics of the Dark Universe*, **2020**, *30*, 100689.

5. "Constraints on MeV dark matter and primordial black holes: inverse Compton signals at the SKA", Bhaskar Dutta, Arpan Kar, Louis E. Strigari, *JCAP*, **2021**, *03*, 011.

List of Publications not included in the thesis

Journal

1. "Search for decaying heavy dark matter in an effective interaction framework: a comparison of γ-ray and radio observations", Avirup Ghosh, Arpan Kar, Biswarup Mukhopadhyaya, *JCAP*, **2020**, *09*, 003.

2. "Dark matter, extra-terrestrial gamma-rays and the MSSM: a viability study", Arpan Kar, Sourav Mitra, Biswarup Mukhopadhyaya, Tirthankar Roy Choudhury, *JCAP*, **2018**, *02*, 045.

Conferences

1. Presented a talk “Neutralino dark matter, galactic centre gamma rays and the MSSM”, SUSY, 2017, TIFR, Mumbai, India.

2. Presented a talk “Can SKA-Phase1 go much beyond the LHC in supersymetry search?”, XXIII DAE-BRNS HEP Symposium, 2018, IIT Madras, India.

Arpan Kar.

Arpan Kar

Dedicated to

Ma, Baba and Didi

ACKNOWLEDGEMENTS

First and foremost I would like to convey my sincere gratitude to my former supervisor Prof. Biswarup Mukhopadhyaya for giving me the opportunity to pursue my research under his supervision for the last five years. I am thankful to him for introducing me to the physics topics studied in this thesis and helping me improve my knowledge on the subject matter. His guidance, critical insights and useful suggestions have helped me a lot to carry out my thesis work. Without his continuous support and encouragement the thesis would not have come to reality. I would also like to express my sincere thanks to my present supervisor Prof. Santosh Kumar Rai for guiding me during the final stage of my PhD course. His timely guidance and support have made it possible for me to complete my thesis.

I am grateful to all my collaborators who have helped me gain better understanding of the subjects discussed in this thesis. I especially want to thank Prof. Tirthankar Roy Choudhury and Dr. Sourav Mitra for sharing with me their knowledge and experience about various important aspects of astrophysics. I express my gratitude to Prof. Steven Tingay and his group for having useful discussions with me and assisting me with their important contributions in several astronomical observations presented in this thesis. I also thank Prof. Bhaskar Dutta and Prof. Louis E. Strigari for their valuable comments and suggestions; collaboration with them has helped me a lot to learn many new things.

Next I would like to thank my doctoral committee members Prof. Pinaki Majumdar, Prof. Asesh Krishna Datta, Prof. Anirban Basu and Prof. Prasenjit Sen, who have supported me during the period of my PhD. Their comments and suggestions regarding my research work have helped me clarify my understanding in many cases. I am also thankful to the former chairperson of my doctoral committee, Prof. Raj Gandhi, for providing valuable advice on some of my work. My sincere gratitude goes to Prof. Ashoke Sen, Prof. Biswarup Mukhopadhyaya, Prof. Pinaki Majumdar, Prof. Satchidananda Naik, Prof. Sandhya Choubey, Prof. Santosh Kumar Rai, Prof. Dileep Jatkar, Prof. Jayanta Bhattacharjee, Prof. Anirban Basu and Prof. Kaoru Hagiwara, for giving me the opportunity to attend the great physics courses offered by them. I am obliged to the HEP group at HRI, whose frequently organised seminars, schools and workshops were very beneficial to me.

I convey my thanks to Dr. Subhadeep Mondal, Dr. Anirban Biswas, Dr. Aritra Gupta, Dr. Nabarun Chakrabarty and Dr. Tanmoy Mondal for having useful discussions and sharing their physics expertise with me. I thank my collaborator and colleague Avirup Ghosh for discussing various physics relted issues with me and also helping and supporting me in many academic and non-academic matters during the time span of my PhD. I appreciate the favours I have received from Dr. Juhi Dutta, Dr. Indrani Chakraborty, Dr. Kasinath Das, Dr. Siddharth Dwivedi and Dr. Tousik Samui. It gives me pleasure to thank Ritabrata Bhattacharya, Dibya Kanti Mukherjee, Subhroneel Chakrabarti, Avirup Ghosh, Aritra Gupta, Nabarun Chakrabarty, Mehedi Masud, Titas Chanda, Subhadeep Mondal, Nilay Kundu, Arijit Dutta, Samiran Roy, Purusottam Ghosh, Biswajit Sahoo, Jaitra Chattopadhyay, Bidisha Roy, Nirnoy Basak and Susovan Maity for making my campus life at HRI enjoyable. I acknowledge the support provided by RECAPP for my academic travels to other institutes, schools and conferences during my PhD. In addition, I give thanks to the HRI administration, computer centre and office-staffs for taking care of various technical aspects as well as my stay at HRI.

Last, but not the least, I express my thanks to my family, especially my parents and elder sister. They have always supported me, respected my decisions and kept patience with me. Without their love, motivation, constant support and encouragement my academic journey would have been impossible.

CONTENTS

List of Figures

List of Tables

Chapter 8

Conclusions

While the existing direct search or collider experiments have not yet found any signature of a DM candidate and thus impose constraints on its microscopic properties, we show in this thesis that the indirect search of DM based on the observation of radio signals, which are induced by the electrons and positrons generated from DM initiated processes inside galaxies or galaxy clusters, may become an alternative avenue for unveiling the nature of DM. Using a few radio telescopes, we analyse the detection prospects of these radio signals for a wide range of DM mass and find that such studies can enable one to probe the regions of the DM parameter space that are difficult to access in other experiments employed for the search of DM. Furthermore, we have shown how one can use observations of DM induced signals in different frequency bands, for example, radio and gamma-ray frequencies, to constrain the coupled parameter space of DM and galactic astrophysics. A brief summary of all the studies performed in this thesis and the resulting outcomes is provided below:

- Using the upcoming radio telescope Square Kilometre Array (SKA), we have studied in Chapter 3 the prospects for observing the radio synchrotron signals that can originate in dwarf galaxies due to the pair-annihilation of MSSM lightest neutralino (which serves as the DM candidate). We consider several benchmarks in MSSM and show that the SKA, with just about 100 hours of observation in its first phase, is capable of probing such regions in the MSSM parameter space where the superparticles are heavy enough in comparison to the mass scales accessible by a high luminosity collider like the LHC. We estimate the radio signals for different values of the diffusion coefficient (D_0) and the magnetic field (B) in dSphs and find that our conclusion remains true even for conservative choices of these parameters.

- In Chapter 4, we analyse in details the effects of various physics phenomena based on which the radio synchrotron flux produced from the pair-annihilation of heavy DM particles, having masses at the TeV scale, can be detected with the SKA. For illustrating our points, we use the dSph Draco as the source of the radio signals. The radio synchrotron flux generated inside a small scale object like a dSph depends not only on the DM pair-annihilation rate, and the cascades of the annihilation products that give rise to energetic $e^{\pm}$ pairs, but also on the energy loss and the diffusion of those $e^{\pm}$ during their propagation through the interstellar medium (ISM) of the dSph. In addition, the magnetic magnetic field is always present which drives the synchrotron emission. Keeping these facts in mind, we have studied the roles of different particle physics and astrophysical parameters separately. We notice that the following three reasons are responsible for enhancing the trans-TeV DM induced radio signals:

  1. Abundance of energetic electrons and positrons in the annihilation spectrum of heavier DM particles, which after energy loss increases the $e^{\pm}$ population at low energy regions and thereby leads to an amplified radio signal in the frequency range of the SKA.

  2. Dominant annihilation into $b\bar{b}$ or $t\bar{t}$ channel which produces large amounts of $e^{\pm}$ over the entire energy range of the spectrum.

  3. A sizable annihilation rate, which is possible to achieve (maintaining the DM relic abundance correctly) in a supersymmetric scenario like the MSSM by tuning the mass parameters properly.

  We present the SKA sensitivities (assuming 100 hours of observation towards Draco) in the DM annihilation rate vs. DM mass plane for different annihilation channels and show that these limits are stronger (even for a DM mass of several TeV) than those obtained from Fermi-LAT gamma-ray and AMS-02 cosmic-ray antiproton observations. Taking a few MSSM benchmarks, where the neutralino DM mass is in the range 1 - $\sim$ 10 TeV, we show that, while constraining such benchmarks is well beyond the reach of the available indirect search observations, they are possible to probe at the SKA. Additionally, we have identified the viable regions in the magnetic field (B) - diffusion coefficient (D_0) plane of Draco, which are able to produce detectable signals at the SKA for trans-TeV DM annihilations. The corresponding DM annihilation rates are assumed to be consistent with the existing indirect search bounds. Our results indicate that the SKA can probe such values of B and D_0 that are usually very difficult to measure in the available astronomical experiments.

- Chapter 5 presents the observational constraints on the annihilating DM parameter space, which are estimated using the low-frequency radio data from the Murchison Widefield Array (MWA) telescope, a precursor to the SKA. Such radio data are corresponding to the observations of 14 dSph galaxies between declinations $+30°$ and $-55°$. After removing the point source contributions in each case, the most stringent constraints are obtained from the Bootes (Boo) dSph. While the Phase I MWA survey did not find any signature of a diffuse radio synchrotron emission related to DM annihilation and thus does not contradict the observation made by the Fermi-LAT or the AMS-02, the Phase II MWA can constrain some regions of the DM parameter space that are hitherto unexplored by existing indirect search experiments. Our analysis show that such regions may get extended up to a DM mass of ~ 1 TeV (~ 1.6 TeV) for a magnetic field value of 1 μG (2 μG). Although the future SKA is expected to probe much deeper into the parameter space, the MWA provides a valuable first step towards the SKA at low frequencies.

- Studies performed by the authors of [124] and [193] suggest that a significant portion of the total mass content of the Milky Way globular cluster ω Cen may be composed of dark matter. They have shown that one possible interpretation of the excess in the Fermi-LAT gamma-ray data from ω Cen can be in terms of the pair-annihilation of GeV scale DM particles. Using their best-fit annihilation models along with the upper limit on the radio flux obtained by the Phase I MWA survey of ω Cen, we exclude in Chapter 6 considerable parts of the $B - D_0$ plane in ω Cen. Furthermore, an independent estimation of the magnetic field at the location of ω Cen enables us to put constraints on the diffusion coefficient which is rather difficult to measure. Improvement by a factor of 10-100 on the radio limits, which is expected to be achieved in the Phase II survey of MWA as well as in the first phase of the upcoming SKA, can constrain the parameter space even more tightly.

- In Chapter 7, we study the prospects of constraining the MeV DM and primordial black holes (PBHs) at the upcoming SKA telescope. If dark matter is composed of some yet unknown weakly interacting MeV scale particles, then their pair-annihilations or decays inside a galaxy or a galaxy cluster may give rise to copious pairs of low energy electron and positron. They can also arise from the Hawking radiation of PBHs, having masses in the range $\sim 10^{15}$–10^{17} g. We show that the photon flux generated via the Inverse Compton (IC) scatterings of these low energy $e^{\pm}$ on CMB may appear as radio signals and can be detected at the SKA within a moderate observation time. We use the dSphs Segue I and Ursa Major II, the globular cluster ω-cen and the Coma cluster as targets and derive the corresponding SKA constraints (for 100 hours of observation) on the annihilation and decay rates of MeV DM as well as on the abundance of PBHs. In the MeV DM mass range ~ 1 to a few tens of MeV and for PBH masses greater than a few factors of 10^{15} to 10^{17} g, the SKA constraints are found to be stronger compared to those obtained from existing indirect search observations. Moreover, the SKA constraints obtained here do not depend on the magnetic fields of the targets. In addition, we have also marked out the viable regions in the diffusion parameter space in a dSph that lead to detectable IC signals at the SKA.

SUMMARY

This thesis is aimed at using astronomical observations, with special emphasis on radio signals, in identifying signatures of dark matter (DM) annihilation in astrophysical systems. We have shown that one can thus explore regions in the DM parameter space, which are beyond the reach of other existing DM search experiments.

A weakly interacting DM candidate is difficult to detect at high-energy collider experiments like the Large Hadron Collider (LHC), if the mass of the DM particle is close to, or higher than a TeV. On the other hand, pair-annihilation of such particles may give rise to e^+e^- pairs in dwarf spheroidal (dSph) galaxies, which in turn can lead to diffuse radio synchrotron signals that are detectable at the radio telescopes. We study the potential of the upcoming radio telescope Square Kilometre Array in the first phase (SKA1) in detecting such radio signals from dwarf spheroidals. Taking a popular scenario, namely, the minimal supersymmetric standard model (MSSM) as illustration, we show that it is possible to detect such signals for DM masses about an order of magnitude beyond the reach of the LHC, with about 100 hours of observation with the SKA1.

We further investigate the circumstances under which the complementarity between collider and radio signals of DM can be useful in probing physics beyond the Standard Model of elementary particles. Both particle physics issues and the roles of diffusion and electromagnetic energy loss of the $e^{\pm}$ are studied in detail. First, the criteria for detectability of trans-TeV DM are analysed independently of the particle physics model(s) involved. We thereafter use some benchmarks based on the MSSM and show that it is not only possible to observe the radio flux from a dSph like Draco at the SKA for DM masses up to ~ 10 TeV, but also heavier DM particles can sometimes produce signals that are larger in comparison to those resulting from lighter DM particles. In addition, the regions in the space spanned by astrophysical parameters, for which the heavier DM induced radio signals should be detectable at the SKA, are marked out.

Along with these, we also present the first observational limits on the predicted synchrotron signals from particle DM annihilation models in dSph galaxies at radio frequencies below 1 GHz. We use a combination of survey data from the Murchison Widefield Array (MWA) (a precursor to the future SKA) and the Giant Metre-wave Radio Telescope (GMRT) to search for diffuse radio emission from 14 dSphs. Even though, for an in-situ magnetic field

of 1 μG and any plausible value for the diffusion coefficient, our limits do not constrain any new DM models, for stronger magnetic fields our data might provide constraints comparable to existing limits from gamma-ray and cosmic ray observations. Predictions for the upgraded MWA show that models with DM mass up to a TeV may be constrained for a magnetic field of 1 or 2 μG.

In addition to the 14 dSphs, we present an analysis of the MWA radio telescope data from the globular cluster ω Cen, possibly a stripped dwarf spheroidal galaxy core captured by our Galaxy. Recent interpretations of Fermi-LAT γ-ray data by Brown *et al.* (2019) and Reynoso-Cordova *et al.* (2019) suggest that ω Cen may contain significant DM. We utilise their best-fit DM annihilation models, and an estimation of the magnetic field strength in ω Cen, to calculate the expected radio synchrotron signal from annihilation, and show that one can usefully rule out significant parts of the magnetic field - diffusion coefficient plane in ω Cen using our current observational limits on the radio emission.

Finally, we investigate the possibilities for probing MeV range DM particles and also primordial black holes (PBHs) (for masses $\sim 10^{15}$–10^{17} g) at the upcoming SKA, using photon signals from the Inverse Compton (IC) effect within a galactic halo. Pair-annihilation or decay of MeV DM particles (into e^+e^- pairs) or Hawking radiation from a population of PBHs generates mildly relativistic $e^\pm$ which can lead to radio signals through the IC scattering on low energy cosmic microwave background (CMB) photons. We study the ability of SKA in observing such signals coming from nearby ultra-faint dwarf galaxies Segue I and Ursa Major II as well as the globular cluster ω-cen and the Coma cluster. We find that, with approximately 100 hours of observation, the SKA can improve the Planck constraints on the DM annihilation/decay rate and the PBH abundance for masses in the range ~ 1 to few tens of MeV and above 10^{15} to 10^{17} g, respectively. Importantly, the SKA limits are independent of the assumed magnetic fields within the galaxies. Regions in the diffusion parameter space of MeV $e^\pm$ inside a dSph that give rise to observable signals at the SKA are also identified.

Chapter 1

Introduction

Dark matter has appeared as one of the major ingredients of the energy density of our universe. Various astrophysical and cosmological experiments, performed over the last several decades, have proved the existence of dark matter. Precise measurements reveal that it covers more than one-fourth of the energy density of our universe. However, all the available proofs that support the existence of dark matter are based only on its gravitational interaction. Its microscopic features are still unknown to us. The Standard Model (SM) of known elementary particle physics can not provide a satisfactory explanation for the dark matter. In this thesis, we will focus mainly on the study of various astrophysical signals that can arise from dark matter. In order to estimate such signals, one needs to have a good knowledge on the elementary particles of SM and their interactions. Therefore, before going into the discussion on dark matter, we start with a brief summary of the SM.

1.1 The Standard Model

Properties of three of the four known fundamental forces in nature (i.e., electromagnetic, weak, and strong interactions) as well as the classification of all known elementary particles including their interactions with these forces are described by the theory called the Standard Model of particle physics [1–3]. This theory has been verified many times over the last several decades in various collider experiments such as the Large Electron-Positron Collider (LEP), the Tevatron and also recently at the Large Hadron Collider (LHC). No considerable deviation from its predictions has been observed yet which shows the stunning achievements of this theory in explaining the quantum realm of elementary particles.

SM fields	$SU(3)_C$	$SU(2)_L$	$U(1)_Y$
$\begin{pmatrix} u_L \\ d_L \end{pmatrix}, \begin{pmatrix} c_L \\ s_L \end{pmatrix}, \begin{pmatrix} t_L \\ b_L \end{pmatrix}$	3	2	1/3
$u_R, \quad c_R, \quad t_R$	3	1	4/3
$d_R, \quad s_R, \quad b_R$	3	1	-2/3
$\begin{pmatrix} \nu_{e_L} \\ e_L \end{pmatrix}, \begin{pmatrix} \nu_{\mu_L} \\ \mu_L \end{pmatrix}, \begin{pmatrix} \nu_{\tau_L} \\ \tau_L \end{pmatrix}$	1	2	-1
$e_R, \quad \mu_R, \quad \tau_R$	1	1	-2
${G_\mu}^{\{1,....,8\}}$	8	1	0
${W_\mu}^{\{1,2,3\}}$	1	3	0
B_μ	1	1	0
$\phi = \begin{pmatrix} \phi^+ \\ \phi^0 \end{pmatrix}$	1	2	1

Table 1.1: The field content of the SM.

The SM is a renormalizable relativistic gauge quantum field theory whose internal symmetries are governed by the unitary product group $SU(3)_C \times SU(2)_L \times U(1)_Y$. These gauge groups correspond to the color, weak isospin and hypercharge symmetries, respectively. The field content of the SM includes 12 elementary spin-$\frac{1}{2}$ fermions; each of them has its own conjugate field. Six of these fields belong to the quark sector which is composed of three generations of up type quarks, i.e., up (u), charm (c) and top (t) quarks, together with three generations of down type quarks, viz., down (d), strange (s) and bottom (b) quarks. The other six fermion fields are categorized into three charged leptons, namely, electron (e^-), muon (μ^-) and tau (τ^-), and three neutrinos (i.e., ν_e, ν_μ and ν_τ). The SM is a chiral theory where each fermion field has both left (L) and right (R) chiral components, except the neutrinos which come with only left chirality. The left-chiral (or left-handed) components of an up and a down type quark in each generation form a doublet under the $SU(2)_L$ gauge transformation. Similarly, the pair of two left-handed leptons, i.e. a left-handed neutrino and a left-handed charged lepton, from each generation, acts as a $SU(2)_L$ doublet. On the other hand, the right-handed counterpart of any individual quark or charged lepton field transforms as a singlet under $SU(2)_L$. As for the $SU(3)_C$ gauge transformation properties of the fermions, each quark field (which can carry three different colors) behaves as a triplet, but the lepton fields, since they do not carry any color, act as singlets. The list of all elementary fermion fields along with their respective quantum numbers associated with each member of the product group $SU(3)_C \times SU(2)_L \times U(1)_Y$ is given in table 1.1. The numbers listed in the second and third columns of this table denote the dimensions of representation for each field configuration under $SU(3)_C$ and $SU(2)_L$ respectively, while the last column shows the corresponding values of the hypercharge Y. The associated electric charges are determined by the relation, $Q = I_3 + Y/2$, where Q is the electric charge, I_3 is the quantum number related to the third component of weak isospin and Y is the hypercharge value. For a $SU(2)_L$ doublet, $I_3 = +\frac{1}{2}$ and $-\frac{1}{2}$, whereas for a singlet state it is 0. Using the above relation and the quantum numbers listed in table 1.1, one obtains $Q = +\frac{2}{3}$ for the up type quarks, $Q = -\frac{1}{3}$ for the down type quarks, while $Q = -1$ for the charged leptons. The neutrinos are chargeless and thus electrically neutral.

As can be seen from table 1.1, apart from the above-mentioned fermion fields, there are spin-1 gauge boson field(s) corresponding to each gauge group in SM. The $SU(3)_C$ color group gives rise to eight gluon fields (denoted by G_μ) which transform in the adjoint representation of $SU(3)_C$ and mediate the strong interactions between the quarks. The weak isospin and hypercharge group $SU(2)_L \times U(1)_Y$ contains four gauge bosons, namely, W^1_μ, W^2_μ, W^3_μ (belonging to $SU(2)_L$) and B_μ (associated with $U(1)_Y$); their various combinations act as the mediators of the electroweak interactions. The W_μ's form a triplet under the $SU(2)_L$ transformation. The value of the hypercharge Y is 0 for all gauge bosons.

In addition, there is a scalar field ϕ (see table 1.1), which is a $SU(2)_L$ doublet but a singlet of $SU(3)_C$. It contains two complex scalars, ϕ^+ (with $Q = +1$) and ϕ^0 (with $Q = 0$), and has a hypercharge $Y = +1$. To start with, all the fermions and gauge bosons of SM are massless in order to maintain the gauge symmetry defined by the unitary product group. Their (excluding the neutrinos) masses are generated via a mechanism called spontaneous symmetry breaking [4–6], where the $SU(2)_L \times U(1)_Y$ symmetry group breaks down to an abelian gauge group $U(1)_{em}$ corresponding to the charge operator Q (the subscript *em* stands for electromagnetic). The full SM Lagrangian consists of four parts and can be written as,

$$\mathcal{L}_{\text{SM}} = \mathcal{L}_{\text{fermion}} + \mathcal{L}_{\text{gauge}} + \mathcal{L}_{\text{scalar}} + \mathcal{L}_{\text{Yukawa}}. \tag{1.1.1}$$

The Lagrangian $\mathcal{L}_{\text{fermion}}$ contains fermionic kinetic terms that give rise to strong interactions (mediated by the gluons) for quarks and electroweak interactions (mediated by the W_μ's and B_μ) for both quarks and leptons. The dynamics of the gauge bosons themselves are described by the Lagrangian $\mathcal{L}_{\text{gauge}}$; it incorporates the self interactions of the gauge bosons corresponding to the non-abelian groups $SU(3)_C$ and $SU(2)_L$. The spontaneous symmetry breaking happens in the scalar sector $\mathcal{L}_{\text{scalar}}$ which includes a scalar kinetic term, involving weak gauge bosons, as wells as a ϕ^2 and a ϕ^4 type interactions. The neutral component (ϕ^0) of the scalar field ϕ acquires a vacuum expectation value (vev), causing the electroweak symmetry breaking (EWSB) in the vacuum of the scalar potential. This mechanism gives rise to a massive real scalar field h (named as the Higgs boson) whose mass is determined by the combination of the vev and the coupling associated with the ϕ^4 term. In the broken phase, the mass terms for the W_μ and B_μ bosons arise from the scalar kinetic term. By transforming the gauge basis, containing W^3_μ and B_μ, to the mass basis, one obtains two mass eigenstates Z_μ and A_μ, where Z_μ (the Z-boson) is massive but A_μ (which represents the photon or γ) is massless. On the other hand, a linear combination of W^1_μ and W^2_μ leads to the charged gauge boson W^+_μ whose conjugate field or antiparticle is W^-_μ, having the same mass as W^+_μ. Since gluons do not couple to the scalar field ϕ, they remain massless. While W^+_μ and W^-_μ are two charge eigenstates, carrying $Q = +1$ and $Q = -1$ charges respectively, the Z-boson, the photon and the gluons are chargeless. $W^\pm_\mu$ and Z_μ mediate the weak interactions, whereas A_μ is responsible for the electromagnetic interactions.

The last term in Eq. 1.1.1 describes the Yukawa interactions of fermions involving either the scalar field ϕ or its conjugate field $\bar{\phi}$ ($\equiv i\sigma_2\phi^*$). After the symmetry breaking, this term generates mass for the quarks and the charged leptons, while the neutrinos do not get any mass. An up or a down type quark in each generation is heavier than that in the previous generation; the same is true for the charged leptons also. The diagonalization of the mass matrix in the quark sector gives rise to the Cabibo-Kobayashi-Maskawa (CKM) matrix in the charged current interaction involving W^+_μ (W^-_μ) and a pair of up and down type quarks. Elements of the CKM matrix allow the decays of heavier up (or down) type quarks into lighter down (or up) type quarks not only in the same generations but also from the higher generations to the lower ones.

The particle content of SM includes antiparticles, too. Each particle and its corresponding antiparticle carry the exact same mass, but their electric charges are opposite to each other. The antiparticles of quarks are called antiquarks (for example, the antiparticle of the bottom quark b is bottom antiquark, denoted by $\bar{b}$). The antiparticles associated with l^- (charged leptons), ν_l (neutrinos) and W^+-boson are l^+, $\bar{\nu_l}$ (antineutrinos) and W^-, respectively. Particles like Z-boson, photon (γ), gluons (g) and Higgs (h), on the other hand, are their own antiparticles. Two or more quarks, bounded together by the strong interaction, form hadrons which are color singlet and can be divided into two categories, mesons and baryons. The usual examples of mesons are charged pions ($\pi^{\pm}$), neutral pion (π^0) etc., while particles such as proton (p), neutron (n) etc., belong to the baryon category.

Limitations of the SM

Although SM is quite successful in describing various features of known elementary particles, there are several things in nature whose explanations are beyond the scope of this theory. For example, SM can not explain neutrino mass, matter-antimatter asymmetry, naturalness problem (related to the radiative divergence in the Higgs mass), hierarchy in the Yukawa couplings of fermions, etc. It also does not include gravity, one of the four fundamental forces in nature. Apart form these, as mentioned previously, the SM does not provide any suitable candidate for describing the entire observed abundance of dark matter, which is one of the biggest mysteries of our universe. In order to explore the particle nature of dark matter, one needs to go beyond the framework of SM. We discuss below different aspects of dark matter including its possible candidates and observational prospects in terrestrial as well as extraterrestrial observations.

1.2 Dark Matter

Dark matter is referred as 'dark' due to the fact that it does not seem to emit, absorb or reflect any electromagnetic radiation. The lack of its interactions with the radiation or the ordinary baryonic matter, except through gravity, makes it difficult to detect directly. Precise astronomical measurements show that it accounts for almost 27% of the energy density and approximately 85% of the total matter content of the universe. In this section let us briefly review some of the astrophysical and cosmological observations which provide strong evidences in support of the existence of the dark matter (DM).

1.2.1 Observational evidences for DM

1. **Galaxy clusters:** First observational evidence for dark matter came in the early 1930s when Fritz Zwicky and other astronomers estimated the total mass of some galaxy clusters and compared them against the mass corresponding to the luminous matter inside those clusters [7, 8]. These measurements revealed that the combined luminous mass of all the member galaxies of a cluster is much smaller than its total

mass required for binding the member galaxies gravitationally. This points towards the existence of a hitherto unknown invisible matter.

2. **Rotation curves of galaxies:** The most compelling evidence for dark matter was obtained from the behaviour of the rotation curves of spiral galaxies [9–11]. Due to the gravitational pull, arms of a spiral galaxy rotate around its center. According to Newton's law of motion and laws of gravity, the rotational velocity of stars outside the luminous core of a galaxy should be inversely proportional to the square root of the radial distance and thus should decrease if one moves away from the center of the galaxy [12]. However, astronomical observations show that, instead of falling, the rotation curve corresponding to a galaxy remains almost flat as the radial distance from the center rises [13]. Assuming Newton's laws are correct, one way to resolve this inconsistency is to accept the presence of a population of dark matter (which is non-luminous but massive) distributed beyond the luminous region of the galaxy.

3. **Velocity dispersions:** Motions of stars or gas particles in a galactic system obey the virial theorem. Using this theorem, along with the observed velocity distribution of stars, one can estimate the spatial distribution of mass inside a galaxy. In most of the cases, the measured velocity dispersion of stellar objects in a galaxy does not match the prediction obtained from the luminous mass distribution of the galaxy [14, 15]. Like in the case of galactic rotation curves, this discrepancy, too, can be resolved by postulating the presence of dark matter in the galactic systems.

4. **Cosmic microwave background (CMB):** Although dark matter is a major part of the matter content of our universe, it does not behave as ordinary matter which is mostly made of baryons. In the early universe, ordinary matter particles were in the ionized form and thus interacted strongly with the electromagnetic radiation. Such interactions determined the spectral shape of the relic radiation known as Cosmic microwave background (CMB). On the other hand, dark matter does not interact with the radiation directly, but its gravitational potential alters the velocity and density distributions of ordinary matter which in turn affect the CMB spectrum. The perturbations of ordinary and dark matters evolve differently in time and thus leave different footprints on the CMB, giving rise to its anisotropic power spectrum. The analysis of the observed spectral features [16, 17] of the CMB power spectrum helps one to determine the abundance of dark matter precisely [18].

5. **Observation of the Bullet Cluster:** Recent observation of the Bullet Cluster, in-

volving two colliding galaxy clusters, provides one of the best evidence in favour of the existence of the dark matter [19]. The gravitational lensing effect reveals that a large amount of the cluster mass, in the form of a collisionless matter, is distributed far away from the baryonic mass distribution observed in X-ray experiments [20, 21]. Such a phenomenon can easily be explained if one assumes the presence of dark matter surrounding each of the colliding galaxy clusters.

6. **Mass-to-light ratio:** The mass-to-light ratio of an astronomical object is determined by dividing the total mass of the object by its luminosity. This quantity is usually expressed in terms of its value estimated for the sun (i.e., $\frac{M_\odot}{L_\odot}$, where $M_\odot$ is the solar mass and $L_\odot$ is the solar luminosity). The measured mass-to-light ratios of typical galaxies and galaxy clusters are very high, which suggests that a considerable fraction of their mass content can be made of dark matter [10].

Apart from the above-mentioned observations, there are several more evidences, supporting the existence of dark matter. For example, the formation of galaxies, galaxy clusters and stars, which we see in today's universe, would not have been possible without the presence of the dark matter. The current abundance of dark matter in our universe can be estimated in terms of its relic density $\Omega_{\rm DM}h^2$, where $\Omega_{\rm DM}$ is the cosmological density parameter associated with the energy density of dark matter and h is the dimensionless Hubble constant. The precise measurement of the dark matter relic density gives [17, 22, 23],

$$\Omega_{\rm DM}h^2 = 0.120 \pm 0.001, \tag{1.2.1}$$

at the 68% confidence level (C.L.).

1.3 Possible candidates for DM

The astronomical observations suggest that the constituents of dark matter should be massive, non-luminous and collisionless. If one assumes the particle nature of dark matter, then the corresponding DM particles should not have any direct coupling to the SM photon (which implies they should not carry any electric charge). Also, they should not participate in the strong interaction with the SM quarks and gluons. However, they can have weak scale interaction with the SM sector, since the strength of this interaction is much weaker than that of the strong interaction. In addition, in order to describe the observed abundance of dark matter in the universe, the DM particles should be stable, at least on a cosmological time scale.

Depending on the velocity of its constituent particles, dark matter can be classified into three categories: 'cold', 'warm' and 'hot'. In this thesis, we will mostly deal with the cold dark matter (CDM) which is the most favourable scenario according to the current DM models. The term 'cold' refers to such DM particles that were non-relativistic during the matter-radiation decoupling era, which is essential for the formation of the observed galaxies [24]. In this section, we discuss in brief some of the viable candidates for CDM.

1.3.1 Weakly interacting massive particle

One of the popular candidates for CDM is the weakly interacting massive particle (WIMP). It is a new kind of massive and electrically neutral elementary particle, not included in the particle content of the SM. WIMPs are stable and interact with the SM particles only through weak interactions. Their masses are expected to lie in the range spanned from a few GeV to several TeV [25,26]. WIMPs are supposed to be in thermal equilibrium with the SM particles at the early stage of the universe when the temperature of the universe was higher than their masses. The pair-annihilations (driven by weak interactions) of WIMPs with their own antiparticles into lighter SM particles and vice versa maintain this equilibrium. As the universe gradually cools down and the temperature goes below the WIMP mass, the equilibrium number density of WIMPs starts to fall exponentially. At this situation, when the reaction rate of WIMPs lags behind the expansion rate of the universe, the WIMPs start to decouple from the thermal bath and their left over population gives rise to the relic abundance which we observe today. The time evolution of WIMP number density, during the equilibrium as well as after the thermal decoupling, is governed by the Boltzmann equation; for details see [25,27].

There are various candidates for WIMPs; however, in a R-parity conserving supersymmetric theory the WIMP DM candidate can appear naturally. We give below a very brief outline of such a model.

Minimal supersymmetric standard model

The minimal supersymmetric standard model (MSSM) is an extended version of the SM with identical symmetry groups (i.e., $SU(3)_C \times SU(2)_L \times U(1)_Y$) [28,29]. It realizes supersymmetry (SUSY) with minimum number of new particles and interactions that are consistent with phenomenology. The term 'supersymmetry' indicates the symmetry between fermions and bosons. In MSSM, it is assumed that each SM fermion is accompanied by a spin-0 bosonic super-partner (known as 'sfermion'), while each SM gauge boson comes with a corresponding spin-$\frac{1}{2}$ super-partner (called 'gaugino'). For example, up-squarks ($\tilde{u}_{L,R}$, $\tilde{c}_{L,R}$, $\tilde{t}_{L,R}$), down-squarks ($\tilde{d}_{L,R}$, $\tilde{s}_{L,R}$, $\tilde{b}_{L,R}$), charged sleptons ($\tilde{e}_{L,R}$, $\tilde{\mu}_{L,R}$, $\tilde{\tau}_{L,R}$) and sneutrinos ($\tilde{\nu}_{e_L}$, $\tilde{\nu}_{\mu_L}$, $\tilde{\nu}_{\tau_L}$) are the super-partners of up quarks ($u_{L,R}$, $c_{L,R}$, $t_{L,R}$), down quarks ($d_{L,R}$, $s_{L,R}$, $b_{L,R}$), charged leptons ($e_{L,R}$, $\mu_{L,R}$, $\tau_{L,R}$) and neutrinos (ν_{e_L}, ν_{μ_L}, ν_{τ_L}), respectively. Similarly, for the gauge bosons $G_\mu^{\{1,....,8\}}$, $W_\mu^{\{1,2,3\}}$ and B_μ, the respective super-partners are $\tilde{g}^{\{1,....,8\}}$ (gluinos), $\tilde{W}^{\{1,2,3\}}$ (winos) and $\tilde{B}$ (bino). The gauge quantum numbers of each super-partner is identical to that of its SM counterpart. In addition, the MSSM contains two $SU(2)_L$ Higgs doublets, $H_d = (H_d^0,\, H_d^-)$, which gives mass to the down-type quarks and charged leptons, and $H_u = (H_u^+,\, H_u^0)$, which gives mass to the up-type quarks. Their corresponding spin-$\frac{1}{2}$ super-partners (known as higgsinos) are $\tilde{H}_d = (\tilde{H}_d^0,\, \tilde{H}_d^-)$ and $\tilde{H}_u = (\tilde{H}_u^+,\, \tilde{H}_u^0)$, respectively. The MSSM Lagrangian includes the higgsino mass term (involving $\tilde{H}_d$ and $\tilde{H}_u$) which is proportional to the higgsino mass parameter μ. In order to avoid the lepton as well as the baryon number violations, a discrete symmetry, called R-parity (defined as R $= (-1)^{3B+L+2S}$ with B, L and S being the baryon number, the lepton number and the spin of a particle, respectively), is imposed [1]; under this all the super-particles are odd but all the SM particles including the Higgses are even. As long as supersymmetry remains intact, each individual SM particle and its respective super-partner are degenerate in mass. However, the fact that no super-particle has been observed yet compels one to add SUSY breaking terms in the MSSM Lagrangian. The SUSY breaking part contains mass terms for all the scalars (i.e., sfermions and Higgses) as well as gauginos. It also includes trilinear interaction terms, each of which involves a left and a right sfermion and a Higgs. The electroweak symmetry breaking (EWSB) in the Higgs sector gives rise to two CP-even neutral Higgses (i.e., the SM like Higgs h^0 and H^0), a CP-odd neutral scalar (A^0), along with two charged Higgses (H^+ and its antiparticle H^-). After EWSB, the trilinear coupling (A_f) associated with a sfermion ($\tilde{f}$) induces the mixing between its left and right components.

The gauginos, $\tilde{B}$ and $\tilde{W}^3$, mix with the neutral higgsinos ($\tilde{H}_d^0$ and $\tilde{H}_u^0$) after EWSB and give rise to four Majorana mass eigenstates, called neutralinos (χ_i^0, $i = 1, ..., 4$). The neutralino mass matrix contains the following parameters: bino mass (M_1), wino mass (M_2), μ and $\tan\beta$ (which is the ratio of the vevs of H_u^0 and H_d^0). On the other hand, mixing between the charged winos ($\tilde{W}^\pm$, which are combinations of $\tilde{W}^1$ and $\tilde{W}^2$) and charged higgsinos ($\tilde{H}_u^+$

[1]Note that, in the SM the lepton number and the baryon number are accidentally conserved.

and $\tilde{H}_d^-$) leads to two Dirac fermions, known as charginos ($\chi_i^\pm$, $i = 1, 2$). For detailed discussion on MSSM see [28, 29].

The lightest supersymmetric particle (LSP), which is R-parity odd, cannot decay to R-parity even lighter SM particles and hence is stable. For a large region of the MSSM parameter space, the lightest neutralino (χ_1^0) can behave as the LSP. Moreover, it is electrically neutral and interacts with rest of the MSSM particles through weak scale interactions. All these characteristics help it to become a viable candidate for WIMP DM.

1.3.2 Other candidates for CDM

Apart from the GeV/TeV scale WIMP, a MeV range beyond standard model (BSM) particle is sometimes proposed as a possible candidate for CDM. Such DM particles can be produced either thermally or non-thermally. In case of thermal production, the required coupling strengths of MeV DM with the SM particles should be much smaller than those corresponding to the weak scale interactions. Therefore, in this case one needs additional modifications [30–32]. However, for the non-thermal MeV DM particles, the production occurs mainly from the decay or scatterings of heavier particles which are in thermal equilibrium [33, 34].

Observations suggest that the DM particles need to be stable (on a cosmological time scale) in order to exist in the present universe. In most of the scenarios, the DM candidate is assumed to be absolutely stable. This stability is usually achieved via the imposition of a discrete or a continuous global symmetry. Although a discrete symmetry may still hold [35], there is no general principle that can ensure the survival of a continuous global symmetry in the low energy theory, leading to the decay of the DM particle into lighter SM particles [36]. Of course, the lifetime of decaying DM particles should be larger than the age of the universe ($\sim 10^{17}$ s) so that they can explain the observed relic abundance of DM. For MeV scale DM, achieving a lifetime larger than the age of the universe is comparatively easier due to the smaller amount of phase space available to it.

In addition to some new elementary particles, a population of massive objects such as the primordial black holes (PBHs) [37, 38] is also sometimes assumed to describe a fraction of the DM abundance of our universe [39, 40]. PBHs, which belong to the category of massive compact halo objects (MACHOs), are supposed to be formed through large density fluctuations in the very early universe. In principle, their masses can vary from a gram to a million of solar mass. However, since PBHs seem to evaporate continuously through the Hawking radiation process, only those with masses $\gtrsim 10^{15}$ g can exist in today's universe [40].

1.4 Status of DM searches

Till now, all the evidences for dark matter are obtained only through its gravitational effects which do not provide a sufficient information on its constituents. In order to get a better understanding of its microscopic identity, various types of DM search experiments have been constructed or proposed; most of them rely on its non-gravitational interactions. Depending on the search strategy, these experiments can be categorised into three different classes. We review below the status of DM search in these experiments.

1.4.1 Direct detection

Observational evidences indicate the presence of a population of DM distributed throughout our Milky Way galaxy [41–43]. If DM is composed of some sub-atomic particles, then a large number of these particles from our galactic neighbourhood should pass through every square inch of the Earth surface from all directions in per unit of time. Direct detection experiments are designed in a particular way to observe low-energy scatterings of DM particles on detector nuclei (made of protons and neutrons), assuming that the DM has tiny interactions with the ordinary matter. Such scatterings should recoil the nuclei, leading to the emission of energy in the form of a photon or a phonon signal. By probing these signals one can obtain information on the DM-nucleon scattering cross-section as well as on the DM mass. Since WIMPs are comparatively heavy and have weak scale interactions with the SM particles, they are ideal candidates to study in these kind of nuclear recoil experiments. Direct detection experiments like ZEPLIN [44], DEAP [45], DarkSide [46], PandaX [47], XENON [48], LUX [49] etc., use liquid noble gases (mainly, xenon or argon) as the targets. On the other hand, experiments such as PICO [50], PICASSO [51] etc., use fluorine based molecules. SuperCDMS [52], CRESST [53] etc., contain cryogenic detectors that are made up of semiconductor or superconductor crystals.

The rate of signal events produced by the recoils of nuclei inside the detector is proportional to the DM-nucleus scattering cross-section, the local number density of DM (i.e., the local DM mass density divided by the mass of the DM particles) as well as the velocity of the incoming DM particles. For a more accurate modeling of the event rate, a nuclear form factor should also be taken into account [12]. Depending on the nature of WIMP-nucleon couplings, the scattering cross-section can be divided into two categories, spin independent (SI) and spin dependent (SD). The cross-section becomes spin independent if the WIMP has a scalar (or a vector) coupling to the nucleons (i.e., protons and neutrons). On the other hand, an axial-vector coupling between the WIMP and the nucleons leads to a spin dependent cross-section which depends on the total spin of the target nucleus [12,54,55]. In general, a WIMP can have both spin dependent and spin independent interactions with the nucleus and thus the total cross-section should be a sum of SI and SD cross-sections. For an illustration, some of the current direct search constraints on the spin independent WIMP-nucleon cross-section as functions of the WIMP mass have been shown in the left panel of Figure 1.1 (taken from [54]) by various solid lines. The parameter space above these lines (the green shaded region) is excluded at 90% C.L. The 'ν-floor' (shown by the orange dashed line), arising due to the irreducible background generated from coherent scatterings of neutrinos and nucleus, makes the lower part of the parameter space inaccessible. XENON1T, PandaX-II and LUX provide stringent limits for heavier WIMP masses (i.e., above ~ 10 GeV to ~ 1 TeV), whereas in the lower mass range (i.e., below 5 GeV) bounds from DarkSide-50 etc., dominate. No promising evidence for a WIMP DM candidate has been found yet in these experiments [2]. Apart form the spin independent case, limits on the WIMP-nucleon cross-section for spin dependent scenario can also be obtained. As an example, some of such constraints on the WIMP-proton scattering cross-section as functions of the WIMP mass are presented in the right panel of Figure 1.1 (taken from [54]). In this case, if the WIMP mass is below ~ 100 GeV, the most stringent bounds arise from PICO-60, Super-Kamiokande (for $\tau^+\tau^-$ channel) [57] and PICASSO, while for WIMP masses $\gtrsim 100$ GeV, the limit obtained from the IceCube experiment in the $\tau^+\tau^-$ channel [58] is the dominant one. Experiments like XENON1T provide the tightest constraints on the WIMP-neutron spin dependent scattering cross-section. For details readers are referred to [54].

If the DM mass becomes very high, the number density of incoming DM particles gets depleted, causing a suppression in the expected number of signal events. Due to this fact, the direct search experiments start losing their sensitivity as the DM mass approaches near a TeV. On the other hand, a light (for example a MeV) DM can not transfer enough energy to the detector nucleus to produce a detectable signal. Therefore, one needs to depend on the electronic recoils caused by the DM-electron scatterings to constrain the parameter space of such a low mass DM particle. However, the constraints are very weak in comparison to those obtained for a GeV scale DM. For existing direct search constraints on MeV scale DM, see [54].

[2]The DAMA and some other experiments have claimed to detect an annual modulation in the event rate [56]; however, their interpretations (shown by two contours in Figure 1.1) are in contradiction with the results obtained form other experiments.

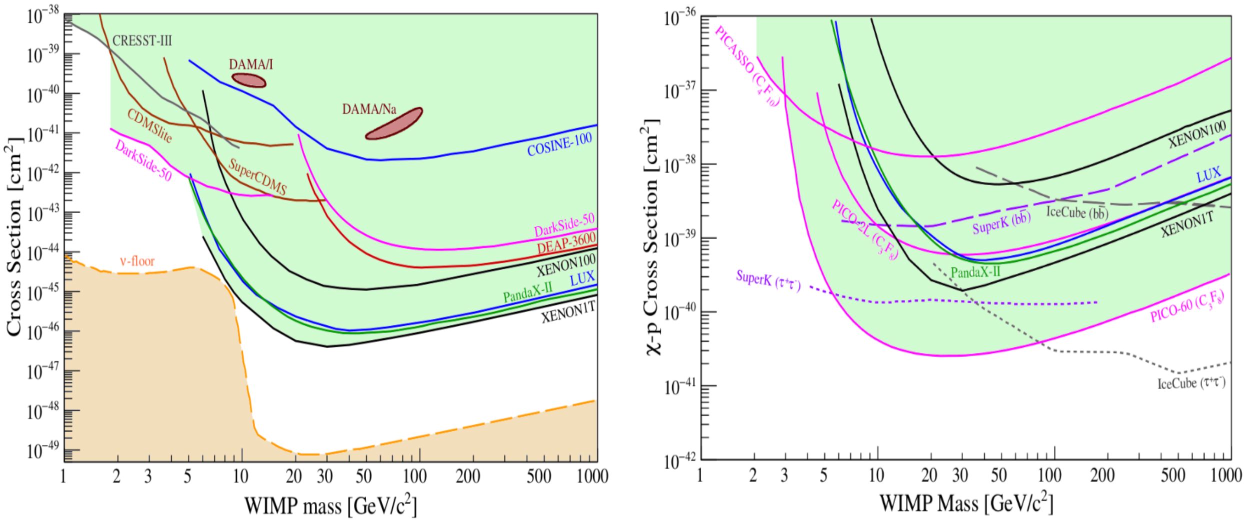

Figure 1.1: Existing direct search constraints on spin independent (left panel) and spin dependent (right panel) WIMP-nucleon cross-sections as functions of the WIMP mass. Figures taken from [54].

1.4.2 Collider searches

Another possible way of detecting the dark matter particles is to produce them in the collider experiments. Even if such particles are produced in the collision of initial state particles inside a collider, they can not be detected directly due to their negligible interactions with the detector materials. However, the momenta of the accompanying visible final state particles can be used to extract information on the DM particles. In a hadronic collider experiment like the Large Hadron Collider (LHC), the momenta of the incoming partons (i.e., quarks and gluons) along the beam axis are unknown, while the momenta in the transverse directions are assumed to be zero. According to the principle of momentum conservation, the total transverse momentum vector ($\vec{P}_T^{inv}$) associated with the produced invisible particles (like the DM) is equal and opposite to that of the visible final state particles (i.e., $\vec{P}_T^{vis}$), the absolute value of which is defined as the missing transverse energy $\not{E}_T$ ($= |\vec{P}_T^{vis}|$). By removing the SM contribution (coming from neutrinos), the quantity $\not{E}_T$ can be used to constrain the new physics scenarios involving DM.

In a supersymmetric model like the R-parity conserving MSSM, the production of colored superparticles (squarks/gluions) at the LHC via strong interaction may be followed by decays in cascade leading to the pair-production of the lightest SUSY particle (LSP), e.g., the lightest neutralino χ_1^0, which serves as DM. Such events are usually characterised by substantial $\not\!\!E_T$ signals. Non-observation of these kind of signals has put constraints on the MSSM parameter space. An example of such constraints in the neutralino mass vs. gluino mass plane is shown in Figure 1.2 (taken from [59]), in the context of the p-p collision at the LHC. This result is obtained by analysing the data collected by the CMS detector during the run 2 of LHC with p-p center-of-mass energy of 13 TeV and integrated luminosity $\int \mathcal{L}dt = 137$ fb^{-1}. The relevant process in deriving the constraint is the pair-production of gluino which subsequently decays into a neutralino in association with a $b\bar{b}$ pair. The black solid lines represent the observed limits (including the higher order corrections in the strong coupling) and associated 1-σ theoretical uncertainties. The parameter space enclosed by the black lines are excluded at 95% C.L, while the shaded region outside is beyond the reach of the current run of the LHC. Since the gluino pair-production cross-section decreases rapidly with the increase in its mass (see [60]), the limits falls sharply above the gluino mass of $\sim$ 2.2 TeV. Increasing the luminosity may push the limit slightly towards the heavier mass range [60]. Limits obtained from the LHC in the MSSM parameter space [61] are comparatively stronger than those provided by other collider experiments like the LEP [62].

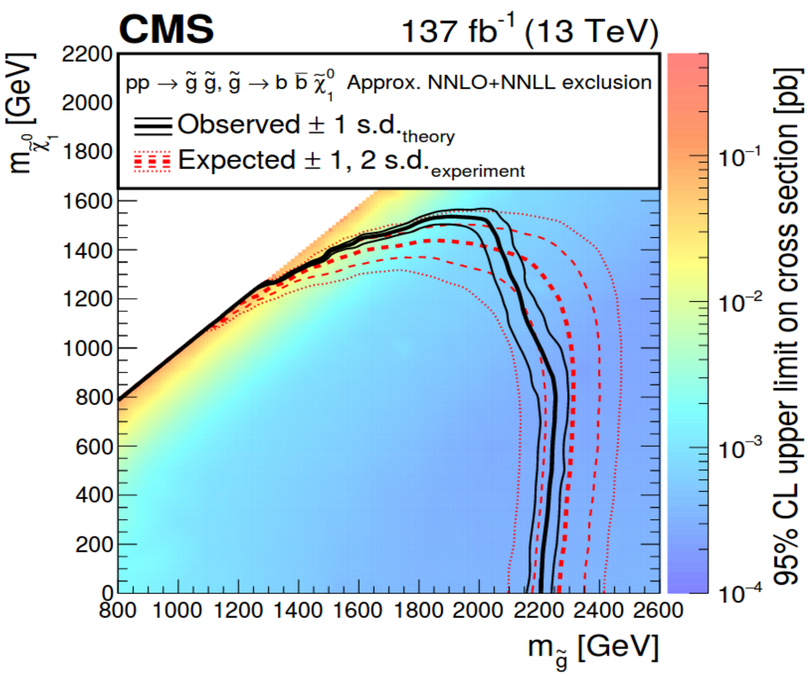

Figure 1.2: Existing LHC constraints on the MSSM parameter space spanned by the lightest neutralino mass and the gluino mass. Figure taken from [59].

On the other hand, for a scenario where the DM particle couples only to the weak sector particles, production at the LHC has to depend mostly on Drell-Yan processes where the rate gets suppressed by the square of the subprocess centre-of-mass energy and also by the parton distribution function at high x. Hence, in such cases, the corresponding limits on the DM parameter space are considerably weaker [63, 64]. If the DM mass is in the sub-GeV range, the detection prospects using the standard $\not{E}_T$ signal at the LHC are not so promising. However, several low energy e^+e^- collider experiments (like BABAR), beam-dump experiments, fixed target experiments etc., have better sensitivities for such light DM candidates [65].

1.4.3 Indirect detection

Since any signature of a weakly interacting massive DM particle has not been observed yet in direct search or collider search experiments, one may think of an additional search strategy of DM, called indirect detection, which is mainly based on the study of various astrophysical signals that can arise from the annihilation or decay of its constituent particles. According to the observational evidences (for example, measurements of galactic rotation curves), the dark matter distributions in galaxies (including our own) or in galaxy clusters form dark halos [41, 66–69] which can be treated as spherical in shape without much error [3]. In the dense environment of the halos, two DM particles can annihilate each other, giving rise to pairs of SM particles (for example, $b\bar{b}$, $\tau^+\tau^-$, W^+W^-, $t\bar{t}$, e^+e^-, $\gamma\gamma$, $\nu\bar{\nu}$ etc.). Particles like $t(\bar{t})$, $W^+(W^-)$, $b(\bar{b})$, $\tau^+(\tau^-)$ etc., subsequently decay and produce photons, electrons (positrons), protons (antiprotons), neutrinos (antineutrinos) etc. The abundance of the final state particles is determined by the DM pair-annihilation rate, the number density of DM particle pairs in the source halo as well as by the nature of the annihilation channel. Therefore, by analysing the spectra of such particles or the astrophysical signals resulting from their interactions with the galactic or cluster environments, one can indirectly obtain information on the properties of DM itself. Since WIMPs are supposed to have sizable annihilation rate in order to produce the relic density correctly, they are ideal candidates for indirect search related studies. However, these types of studies are not restricted to WIMPs only and can be extended to any scenario where the interactions of the DM particle with the SM particles are assumed.

Photons produced in the annihilation of massive DM particles may show up in the gamma-ray observations. As photons travel from the source to the observer along the straight line

[3] In general, DM halos are ellipsoidal in nature. However, in most of the indirect detection studies, one can use spherical halos because the difference caused in the DM signals due to the ellipsoidal shape is very small (not more than 10%).

without much deflection, indirect search for DM through gamma-ray observations are very prominent. Nowadays, there are many gamma-ray telescopes, some of them are space based (for example, Fermi-LAT [70, 71], COMPTEL [72, 73], EGRET [74] etc.), while others are placed on the ground (e.g., H.E.S.S. [75], MAGIC [76], HAWC [77]). The existing Fermi-LAT gamma-ray constraints on the velocity-averaged annihilation rate ($\langle\sigma v\rangle$) of DM as a function of the DM mass (in the range $\sim$ 1 GeV to 10 TeV) are shown in Figure 1.3, for two annihilation channels, $b\bar{b}$ and $\tau^+\tau^-$ [70]. These limits are corresponding to six years of LAT data from dwarf spheroidal galaxies (dSphs). In addition, projected sensitivities of the upcoming high-energy gamma-ray telescope CTA have also been presented [78, 79]. The Fermi-LAT limits are comparatively strong below the DM mass of a few hundreds of GeV, beyond which CTA is expected to dominate. If the annihilating DM particles are in the mass range of a few MeV to a few hundreds of MeV, better gamma-ray constraints come from low energy gamma-ray experiments such as COMPTEL, EGRET, INTEGRAL etc. [80–82].

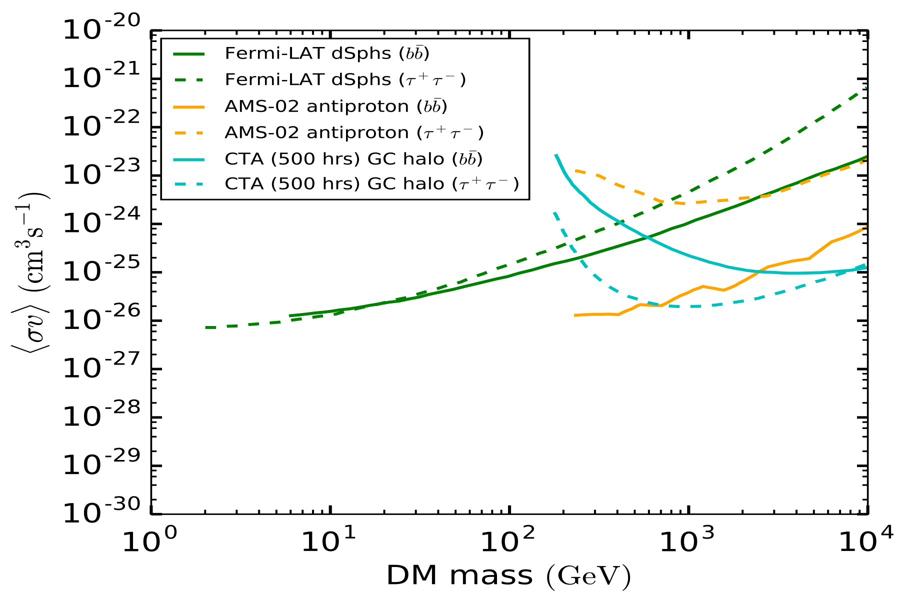

Figure 1.3: Constraints in the DM annihilation rate vs. DM mass plane obtained from Fermi-LAT gamma-ray observation of dSphs [70] and AMS-02 antiproton data [83]. The projected sensitivities of the upcoming gamma-ray telescope CTA has also been shown [78]. All limits are at 95% C.L.

The particles like e^-, e^+, p, $\bar{p}$ etc., once produced in the DM annihilation inside the Milky Way (MW) halo, propagate through the interstellar medium of the galaxy, facing diffusion and energy losses [84–86]. The excess in the observed flux of any of such particles in the cosmic-rays may indicate the possibility of DM annihilation in the MW galaxy. However, these particles can also be produced from some additional sources, the detailed information on which are not known yet. Also, we do not have sufficient knowledge of various astrophysical parameters such as diffusion, energy loss, galactic magnetic field, solar modulation etc., which affect the cosmic-ray propagation. There are various cosmic-ray measurement experiments like AMS [87], PAMELA [88], BESS [89], BESS-Polar [90] etc. Recently, AMS-02 has published precise data on cosmic-ray antiproton flux [87]. The constraints obtained in the annihilating DM parameter space [83] by analysing these data are shown in Figure 1.3 alongside the gamma-ray limits. As one can see, such constraints are usually more effective for heavy DM particles (i.e., above a few hundreds of GeV). On the other hand, electron-positron data from satellite experiments like VOYAGER [91] provide stringent limits on the MeV DM parameter space [92].

In addition, annihilations of DM particles in the early universe may inject energy in the form of photons or $e^{\pm}$ which can affect the CMB. Using the Planck data on CMB anisotropies, one can constrain the DM annihilation rate for different DM masses [93]. However, such constraints are more stringent when the mass of the DM particles are considered to be in the MeV range. Apart from this, observations of galactic or extra-galactic neutrino flux through various neutrino telescopes such as IceCube, KM3NeT etc., can also constrain the DM parameter space [94, 95].

An alternative approach to explore the particle nature of dark matter is to look for the diffuse radio photon signal that may arise from DM induced processes. The energetic $e^{\pm}$, produced from the pair-annihilation of GeV or TeV scale DM particles inside a galaxy or a galaxy cluster, are expected to generate such low-frequency photon signals via the process called synchrotron emission which involves the magnetic field present inside the galaxy or the galaxy cluster. The current experiments, discussed above, have not found yet any compelling evidence for a weakly interacting DM candidate and therefore set constraints on its parameter space. The study of DM induced radio signals, based on the observations of high-sensitivity radio telescopes, may open up the possibility of exploring the DM parameter space that lies beyond the reach of the existing experiments. In this thesis, this will be our main focus. In the next few chapters, we will discuss in detail the production mechanism of DM induced radio flux, the related particle physics and astrophysical processes, the prospects of observing such radio signals using some current and upcoming radio telescopes, and the the corresponding constraints on the DM parameter space as well as on the astrophysical parameters that are involved in generating the radio signals.

Chapter 2

Dark matter induced radio signal

As mentioned in the introduction, weakly interacting dark matter (DM) particles can annihilate in pairs while moving (at a low speed) inside compact DM halos surrounding our own galaxy and also other extra-galactic sources such as dwarf spheroidal (dSph) galaxies, galaxy clusters, etc. Such annihilations can pair-produce various Standard Model (SM) particles which include three generations of quarks and leptons, gauge and scalar bosons and their corresponding antiparticles. For $2 \to 2$ annihilation (as has been considered here), their energies are dictated by the mass of the annihilating DM candidate. These particles may then lead to further cascades and give rise to charged particles like electrons (e^-), positrons (e^+), protons (p) and antiprotons ($\bar{p}$) as well as neutral particles like photons (γ) etc., as the secondary products of the annihilation [70, 83, 84, 95–106]. While the initial step should involve some new physics interactions, the latter step is governed by SM interactions. The stable particles like electrons, positrons and photons may also be produced directly in the annihilation [84, 93, 107]. Depending on the mass of the annihilating DM particles and the annihilation channel, the energy distributions of the produced electrons, positrons and photons will be different [84]. The electrons and positrons, after going through various electromagnetic interactions with the interstellar medium (ISM) of the parent galaxy or galaxy cluster, lead to radio photon emission which can be tried to observe in a radio telescope. In the next few sections of the present chapter, we will discuss in detail the physics phenomena that are involved in the production of such DM induced radio signals. In the last section of the chapter, we will describe the features of some current and upcoming radio telescopes used in our analysis as well as in previous works in the context of indirect DM searches.

2.1 Source function

The energy spectrum of electrons/positrons, generated from DM pair-annihilation inside a galaxy or a galaxy cluster, is obtained by using the source function (Q_e) which can be expressed as [101, 108–111],

$$Q_e(E,r) = \langle \sigma v \rangle \left(\frac{\rho_\chi^2(r)}{2m_\chi^2} \right) \left\{ \sum_f \frac{dN_f^e(E)}{dE} B_f \right\}. \tag{2.1.1}$$

Here $\langle \sigma v \rangle$ is the velocity averaged pair-annihilation rate of the DM particle χ in today's universe (assuming that χ covers the entire observed abundance of DM), m_χ is the DM mass and $\rho_\chi(r)$ is the DM density at a radial distance r from the center of the DM halo that surrounds the target galaxy or galxy cluster. The spectral distribution $\frac{dN_f^e(E)}{dE}$ describes the number of electrons or positrons produced with energy E, per DM annihilation, in an annihilation channel f which consists of a pair of SM particles such as $b\bar{b}, t\bar{t}, \tau^+\tau^-, W^+W^-, ZZ$ etc. Since the annihilating DM particle is electrically neutral, one may assume without loss of generality that the charged particles that are direct products of pair-annihilation are particle-antiparticle pairs. However, particles like the Z-boson (Z), the photon (γ), the Higgs (h) or the gluon (g) may be produced asymmetrically, so long as the known conservation principles are satisfied. For such annihilation final states, one needs to calculate separately the two different $e^\pm$ spectra arising from two distinct SM particles and add them up in each energy bin. In order to make a specific annihilation channel kinematically allowed, the center-of-mass energy of the incoming DM pair should exceed or match the combined mass of the SM particles in that channel. The total electron(positron) distribution is obtained by summing the spectrum $\frac{dN_f^e(E)}{dE}$ over all possible annihilation channels, each of which has a branching fraction or weightage B_f that measures the ratio of the annihilation rate associated with that particular channel to the total annihilation rate $\langle \sigma v \rangle$. The ratio $\frac{\rho_\chi^2(r)}{2m_\chi^2}$ in Eq. 2.1.1 represents the number density of DM pairs at a radius r inside the DM halo (i.e., the square of the number of DM particles per unit volume). An extra factor of 2 has been introduced in the denominator to take into account the over-counting of two identical particles in an annihilating DM pair. We give below a brief description of some important quantities that appear in the expression for the source function.

Annihilation rate $\langle \sigma v \rangle$

For a given DM model, the total pair-annihilation cross-section σ in Eq. 2.1.1 is estimated by adding the cross-sections corresponding to all possible annihilations of the type $\chi\chi \to S_1 S_2$, where S_1 and S_2 are two SM particles. Each of these cross-sections should depend on the effective couplings of χ to SM particles, the particle spectrum of the underlying particle physics model and also on the internal degrees of freedom of χ. The DM particle χ can be a fermion as well as a scalar or a vector boson. The quantity $\langle \sigma v \rangle$ is obtained by averaging σ over the velocity distribution of DM particles inside a galactic halo [27]. For a typical galaxy such as the Milky Way (MW), the mean value of this velocity distribution in the galactic rest frame is around 10^{-3}c (where c is the speed of light in vacuum) [112]. Depending on the mass spectrum of the particle physics model, $\langle \sigma v \rangle$ may get a significant contribution from the resonant annihilation, where the mass of the particle that mediates the annihilation is close to twice the DM mass m_χ [27]. In a scenario like R-parity conserving minimal supersymmetric standard model (MSSM), there are scopes for co-annihilation of the lightest SUSY particle (which serves as a DM candidate) with other heavier SUSY particles which are spaced closely with it [113]. Such processes are more effective in the early universe and play crucial roles in determining the relic abundance of DM. However, since the heavier SUSY particles are supposed to be decayed already into the lightest SUSY particle state and therefore do not exist in today's universe, the co-annihilation effect is unlikely to contribute to the annihilation processes that are happening inside galactic halos. While for most of our analysis we have treated $\langle \sigma v \rangle$ as a free parameter (considering one annihilation channel, which contains a SM particle and the associated antiparticle, is dominant at a time) and tried to constrain it via radio observations, in some cases (as has been shown in Chapters 3 and 4) we have dealt with such values of $\langle \sigma v \rangle$ that are obtained through rigorous numerical calculations for various benchmark points in MSSM.

Energy spectrum $\frac{dN^e}{dE}$

The $e^{\pm}$ energy distribution $\frac{dN^e}{dE}$, resulting from a particular annihilation channel, is a non-trivial function of the DM mass m_χ. On the other hand, for a fixed m_χ, the shape of the distribution varies a lot depending on the types of annihilation channels involved [84]. All possible annihilations in our case can be divided mainly into two categories, i.e., annihilation into a pair of SM fermions $F\bar{F}$ (e.g., $b\bar{b}, t\bar{t}, \tau^+\tau^-$) and a pair of SM gauge bosons $V\bar{V}$ (e.g., W^+W^-, ZZ). Each SM particle in such pairs is produced with energy $\sim m_\chi$. In case of DM annihilation into a pair of Higgs bosons, each Higgs particle in the pair decays dominantly into the pairs of fermions (like $b\bar{b}, \tau^+\tau^-$ and $c\bar{c}$) or gauge bosons (such as $\gamma\gamma$ and gg). In addition, as mentioned earlier, there may be involvement of other annihilation channels which are asymmetric (for example, $Z\gamma, Zh$ etc.). In these cases, the spectrum corresponding to each individual particle determines the shape of the final $e^\pm$ distribution.

For $F\bar{F}$ dominated annihilation, there are three major sources of $e^\pm$:

1. First generation prompt spectrum: This includes the contributions coming from the decay processes such as $t(\bar{t}) \to e^+(e^-)$, $b(\bar{b}) \to e^-(e^+)$, $c(\bar{c}) \to e^+(e^-)$, $\tau^\pm \to e^\pm$ etc. Note that, if m_χ is less than ~ 173 GeV, the $t\bar{t}$ production will be kinematically disfavoured. The electrons(positrons) generated in these processes populate mainly the high energy part of the spectrum $\frac{dN^e}{dE}$.

2. Second generation prompt spectrum: This type of spectrum arises due to the leptonic decays of the particles produced in the decays of primary annihilation products. For example, if a $b\bar{b}$ pair is produced in the first step of the annihilation, then the electron/positron generated in the process $b(\bar{b}) \to c(\bar{c}) \to e^+(e^-)$ will belong to this category.

3. Decay of charged pions: The SM particles produced from DM annihilation may give rise to pions ($\pi^\pm$, π^0) via showering followed by hadronization. Subsequent decays of charged pions ($\pi^\pm$) through $\pi^\pm \to \mu^\pm \nu_\mu(\bar{\nu_\mu})$ along with $\mu^\pm \to e^\pm, \bar{\nu_\mu}(\nu_\mu), \nu_e(\bar{\nu_e})$ lead to comparatively low energetic $e^\pm$ pairs.

Detailed discussions on different energy spectra mentioned above can be found in refs. [114] and [115]. In addition, DM particles can also annihilate directly into e^+e^- pairs causing a sharp peak in the energy spectrum at $E \sim m_\chi$ [84, 116, 117].

For $\chi\chi \to W^+W^-(ZZ)$ kind of annihilation also, the resulting $e^\pm$ spectrum gets contributions from three different processes, i.e., (a) direct decay of $W^\pm$ or Z into $e^+(e^-)$ which produces a spectrum that is nearly uniform within certain kinematic limits (see [118]) and is negligibly small outside; (b) decay of a gauge boson (for example W^+) through $W^+ \to \tau^+ \to e^+$ or $W^+ \to c \to e^+$ which gives rise to a continuum spectrum at $E \lesssim \frac{m_\chi}{2}$; (c) decays of charged pions (produced in the hadronic decay modes of $W^\pm$ or Z) via the decay chains mentioned previously, leading to a soft $e^\pm$ spectrum at $E \lesssim \frac{m_\chi}{2}$. For the spectral shape of the energy distribution in each case, see [114, 118]. Additionally, DM annihilation into $\gamma\gamma$ final state is also possible. In this case, the electron and positron originate mainly due to the splitting of one virtual primary photon [84].

Variation of the $e^{\pm}$ energy distribution from one annihilation channel to another and the way it affects the radio fluxes resulting from different DM masses will be discussed in detail in Chapter 4. The spectrum $\frac{dN^e}{dE}$ corresponding to any annihilation channel described above can be obtained by using the package, called Pythia [119], which is a MonteCarlo code and takes care of processes like showering and hadronization that result from the cascades of various SM particles produced in the DM annihilation. Tabulated forms of these spectra for a wide range of DM mass are available inside the Micromega package [120, 121] and also in various other tools provided in the literature [84].

DM density profile $\rho_\chi(r)$

The astrophysical quantity which plays an important role in determining the abundance of $e^{\pm}$ produced from DM annihilation inside an astronomical object is the DM density distribution of the halo associated with that object. This density distribution is usually described by a spherically symmetric profile $\rho_\chi(r)$, where r is the radial distance of a point inside the galaxy or the cluster. The functional form or the shape of $\rho_\chi(r)$ can be predicted by N-body simulations of cold dark matter (CDM) based on the ΛCDM model for structure formation [101, 109]. The functional form involves two or more free parameters which one can restricts, for a specific galaxy or a galaxy cluster, by using the corresponding stellar kinematics data, i.e., the information of the line-of-sight velocity dispersion of the member stars or the member galaxies [101, 122–124]. Among various types of DM profiles studied in the literature, those which have been mostly used in our case are the Navarro-Frenk-White (NFW) [125] and the Einasto profiles [126]. Their respective analytic forms are,

$$\rho_\chi^{\mathrm{NFW}}(r) = \frac{\rho_s}{\left(\frac{r}{r_s}\right)^{\delta}\left(1+\frac{r}{r_s}\right)^{3-\delta}} \quad \text{with } \delta = 1, \tag{2.1.2}$$

which corresponds to a cuspy NFW profile, and

$$\rho_\chi^{\mathrm{Einasto}}(r) = \rho_s \exp\left\{-\frac{2}{\alpha}\left[\left(\frac{r}{r_s}\right)^{\alpha} - 1\right]\right\} \quad \text{with } \alpha \simeq 0.3. \tag{2.1.3}$$

These profiles are often used for our local dSphs in the context of various indirect search observations [108, 116, 117, 122, 123, 127]. The parameters r_s and ρ_s are called, respectively, the scale radius and the characteristic density of the DM halo. For a dwarf galaxy like Draco, assuming a cuspy NFW profile (i.e., Eq. 2.1.2), typical values of these parameters are $r_s \sim 1$

kpc and $\rho_s \sim 1.4$ GeVcm^{-3}, which are compatible with the kinematical observation of this galaxy [122, 123, 128].

Additionally, in order to examine the variation of the DM induced signal with the DM distribution inside a dwarf galaxy, we have used two other DM profiles, i.e., the profile proposed by Diemand et al. 2005 [129] (thus labeled as D05), whose functional form is similar to the one shown in Eq. 2.1.2 but with $\delta \simeq 1.2$ [128], and the Burkert profile, which has a form described by [128, 130],

$$\rho_{\chi}^{\text{Burkert}}(r) = \frac{\rho_s}{\left(1 + \frac{r}{r_s}\right)\left(1 + \left(\frac{r}{r_s}\right)^2\right)}. \tag{2.1.4}$$

For galaxy clusters such as Coma, a DM profile studied by Navarro et al. 2004 [131] (therefore labeled as N04) is sometimes used [101]; it is similar to the Einasto profile (shown in Eq. 2.1.3) but with $\alpha \simeq 0.17$.

In addition to their mean DM distributions discussed above, DM halos can contain various sub-structures inside them which are denser than the corresponding parent DM structures and thus cause enhancements in the signals produced from DM pair-annihilations. The sub-structure contributions are usually more prominent for large scale systems like galaxy clusters [101, 109], while for dwarf galaxies they can boost the annihilation induced signals up to a factor of $3-4$ [109]. For simplicity, the analyses presented in the next few chapters for small scale objects like dSphs do not consider sub-structure effects which would increase the DM signals predicted in our case by a few factors.

2.2 Transport equation

The source function Q_e, shown in in Eq. 2.1.1, describes the rate at which the pair-annihilation of DM particles injects energetic electron-positron pairs in per unit volume of an astronomical object such as a dSph galaxy. These $e^{\pm}$, after being produced, propagate through the medium of the galaxy which consists mostly of interstellar magnetic field, various radiation fields (like cosmic microwave background (CMB) photons, infrared photons, optical starlight etc.) as well as plasma of charged particles. While traveling through this medium, the electrons and positrons face spatial diffusion and lose energy via various electromagnetic processes. Their combined effects reshape the initial energy distribution of $e^{\pm}$ (generated from DM annihilation) in a non-trivial fashion and give rise to an equilibrium number density $\frac{dn}{dE}$ which can be obtained as a function of the radius r and the electron(positron) energy E by solving the following transport equation [101, 108, 109, 128],

$$D(E)\nabla^2\left(\frac{dn}{dE}(E,r)\right)+\frac{\partial}{\partial E}\left(b(E)\frac{dn}{dE}(E,r)\right)+Q_e(E,r)=0. \tag{2.2.1}$$

Here $D(E)$ is the diffusion term and $b(E)$ denotes the energy loss of charged particles like $e^{\pm}$ in a galactic environment due to various electromagnetic processes. For simplicity, we have assumed a spherically symmetric system[1] and considered the parameters $D(E)$ and $b(E)$ as independent of the spatial coordinates. We have further assumed a steady state condition which in general holds for systems like dwarf galaxies where the typical timescales for the alterations of the source function and the propagation conditions are quite large in comparison to the timescale of the propagation itself [84, 108, 128]. Note that, in addition to the diffusion and energy loss, there may be some additional effects present due to convection and re-acceleration; however they are not included in our case since those effects are usually very suppressed for $e^{\pm}$ [132]. Before we go into the methodology for solving Eq. 2.2.1, let us first discuss briefly the important astrophysical parameters, i.e., $b(E)$ and $D(E)$, that govern this equation and determine the shape of the final $e^{\pm}$ density distribution $\frac{dn}{dE}$.

Energy loss term $b(E)$

The term $b(E)$ that describes the energy loss of $e^{\pm}$ inside a dSph galaxy or a galaxy cluster can be parameterised as [101, 108, 109, 128, 133],

$$\begin{aligned} b(E) \;&=\; b^0_{IC}\left(\frac{E}{\text{GeV}}\right)^2+b^0_{Synch}\left(\frac{E}{\text{GeV}}\right)^2\left(\frac{B}{\mu G}\right)^2 \\ &\quad +b^0_{Coul}n_e\left[1+\frac{\log\left(\frac{E/m_e}{n_e}\right)}{75}\right]+b^0_{Brem}n_e\left[\log\left(\frac{E/m_e}{n_e}\right)+0.36\right]. \end{aligned} \tag{2.2.2}$$

It encapsulates the effects of various energy loss processes such as Inverse Compton scattering on the ambient photon baths, synchrotron effect, Coulomb interaction and Bremsstrahlung. Values of the corresponding energy loss coefficients are taken to be $b^0_{IC}\simeq 0.25$, $b^0_{Synch}\simeq 0.0254$, $b^0_{Coul}\simeq 6.13$ $b^0_{Brem}\simeq 1.51$, all in units of 10^{-16} GeVs^{-1} [101, 108, 109, 128]. The

[1]Note that, the assumption of a spherical symmetry goes well for objects such as dSph galaxies [108, 110, 116, 117, 128]. However, while considering the propagation of charged particles in the Milky Way, one usually assumes a cylindrical shape diffusion region [84–86].

energy loss due to synchrotron effect is proportional to the square of the in-situ magnetic field B (in μG). The quantities m_e and n_e (in the expressions of loss terms related to Coulomb and Bremsstrahlung processes) are, respectively, the electron rest mass and the average thermal electron density inside a galaxy or a galaxy cluster (value of n_e for a typical dSph is $\sim 10^{-6}$, in the unit of cm^{-3} [108, 128]).

The IC and the synchrotron energy losses in Eq. 2.2.2 arise because of the scatterings of energetic $e^{\pm}$ with the background photons (such as the CMB) contained within a galactic system and the present magnetic field B, respectively [84, 133]. For a fixed B-field, the synchrotron loss term always goes as E^2. The IC loss term, on the other hand, deviates from the E^2 dependence when the electron energy E becomes so large (above $\sim 10^6$ GeV) that the electron-photon scattering no longer remains in the Thomson regime and enters into the Klein-Nishina regime [84, 133]. The Coulomb loss term in the expression of $b(E)$ originates due to the coulomb interaction of $e^{\pm}$ with the electrostatic potential created by other charged particles in the thermal plasma which also deflects the trajectories of the $e^{\pm}$ and makes them radiate photons in terms of the bremsstrahlung emission [84, 101, 133]. The energy losses resulting from IC scattering and synchrotron radiation are significant for high E (i.e., $E > 1$ GeV), whereas for E in the sub-GeV range these processes usually become less effective and Coulomb and Bremsstrahlung losses start to dominate.

The astrophysical parameter that drives the energy loss due to synchrotron effect is the ambient magnetic field B. It is extremely difficult to get insights (say, through polarization experiments) for the magnetic field properties of local dSph galaxies. The lack of any strong observational evidence suggests that the magnetic fields could be, in principle, extremely low. On the other hand, there could be various effects which can significantly contribute to the magnetic field strengths in dSph. In fact, numerous theoretical arguments have been proposed for values of B at the μG level. It has been argued, for example, that the observed fall of B from the center of the Milky Way to its peripheral region can be linearly extrapolated to nearby dSph's, leading to $B \gtrsim 1$ μG. Such an assumption is based on the observation of giant magnetized outflows from the central region of the Milky Way pointing towards a B-field which is larger than $10\mu G$ at a distance ~ 7 Kpc from the Galactic plane [134]. In addition, the possibility of the own magnetic field of a dSph has also been suggested. For detailed discussions readers are referred to [135]. For various sources that are within or in the vicinity of the Milky Way, the value of B can in principle be as high as ~ 10 μG [136]. A strong B-field allows the energetic electrons and positrons to lose energy at a large rate and increases their population at lower energies. The effects of B on the equilibrium $e^{\pm}$

distribution $\frac{dn}{dE}$ inside a dwarf galaxy as well as on the final radio flux resulting from such distribution will be analysed in details in Chapter 4.

Diffusion term $D(E)$

While considering a small scale object like a dSph, diffusion plays a major role in determining the density distribution of DM induced electrons/positrons by allowing them to diffuse over a length scale that is comparable to the size of the object itself. Because of their very low luminosity, the exact nature of diffusion in local ultra-faint dSphs is difficult to understand. Following [108, 116, 117, 128, 135, 137], we have parameterised the diffusion term $D(E)$ for electrons and positions in dSph galaxies as,

$$D(E) = D_0 \left(\frac{E}{\text{GeV}}\right)^{\gamma}, \tag{2.2.3}$$

where D_0 is the diffusion coefficient and γ is the diffusion index. In case of the local dwarf galaxies, the index γ can vary from 0 to 1 [137]. For simplicity, choices like $\gamma = 0.3$ (which corresponds to a Kolmogorov form) and $\gamma = 0.7$ are sometimes used in the literature [108, 109, 116, 117, 128, 135] in analogy with its value predicted for the Milky Way [84].

The coefficient D_0 is also very hard to constrain from astronomical observations. Refs. [138, 139] have studied the impact of stochastic gas motions on the diffusion properties of metals in a number of galaxy clusters. From their analysis it is found that D_0 in galaxy clusters can be around $10^{29}\text{cm}^2\text{s}^{-1}$ which is about an order of magnitude higher than the values used for the Milky Way galaxy [84]. As shown in [137], assuming D_0 scales in a similar way from clusters down to the scale of galaxies, the value of the diffusion coefficient in dSph galaxies can be an order of magnitude lower than that assumed for the Milky Way. For a galaxy of size L, the timescale of diffusion within the galaxy and the associated diffusion velocity can be parameterised as $t_\text{d} \sim \frac{L^2}{D(E)}$ and $v_\text{d} = \frac{D(E)}{L}$, respectively. In order to make the diffusion timescale corresponding to $L = 1$ kpc (which is the usual size of the diffusion zone in a typical dSph) smaller than the age of the universe (i.e., $\sim 10^{17}$ s), one should choose $D_0 \gtrsim 10^{26}\text{cm}^2\text{s}^{-1}$ for an electron energy $E = 1$ GeV. With the similar conditions, requiring to have a diffusion velocity that is lower than the speed of light (c), one obtains $D_0 \lesssim 10^{32}\text{cm}^2\text{s}^{-1}$ [135]. In all of our analyses, presented in the next few chapters in the context of dSph galaxies, we have used various values of D_0 in this aforementioned range and simultaneously tried to see its effects on the observable signals by scanning the full parameter space. A higher value of D_0 forces the energetic $e^{\pm}$ to leave the periphery of a galaxy more quickly and thus causes suppression in the signal. Detailed discussions on this phenomenon will be carried out in Chapter 4. For a large system like Coma cluster, where the diffusion timescale is much larger than the usual timescales for energy loss processes, the effect of diffusion in Eq. 2.2.1 is sub-dominant and the $e^{\pm}$ distribution $\frac{dn}{dE}$ is governed mainly by the energy loss term $b(E)$ [101, 108].

Solution to the transport equation

The transport equation 2.2.1 has a generic solution of the form [101, 108, 116, 117, 128],

$$\frac{dn}{dE}(r, E) = \frac{1}{b(E)} \int_{E}^{m_\chi} dE' G(r, \Delta v) Q_e(E', r). \tag{2.2.4}$$

Here $G(r, \Delta v)$ is the Green's function of the equation and is given by [101, 108],

$$\begin{aligned} G(r, \Delta v) \quad = \quad & \frac{1}{\sqrt{4\pi\Delta v}} \sum_{n=-\infty}^{n=\infty} (-1)^n \int_0^{r_h} dr' \frac{r'}{r_n} \left(\frac{\rho_\chi(r')}{\rho_\chi(r)} \right)^2 \\ & \left[\exp\left(-\frac{(r' - r_n)^2}{4\Delta v} \right) - \exp\left(-\frac{(r' + r_n)^2}{4\Delta v} \right) \right], \end{aligned} \tag{2.2.5}$$

with $r_n = (-1)^n r + 2nr_h$, where r_h is the radius of the diffusion zone of a galaxy. Following [84, 108, 116, 117, 128], we have imposed boundary conditions such that the density $\frac{dn}{dE}$ vanishes at $r = r_h$, beyond which electrons and positrons propagate freely and escape. The quantity Δv is expressed as,

$$\Delta v = \int_E^{E'} d\widetilde{E} \frac{D(\widetilde{E})}{b(\widetilde{E})}. \tag{2.2.6}$$

The square root of Δv ($\sqrt{\Delta v}$), which has a dimension of length, determines the distance traveled by an electron or positron before it loses its energy from E' to E. For a large scale object like a galaxy cluster, the electrons/positrons generated from DM annihilation lose all of their energies before reaching the boundary of the diffusion zone. On the other hand, for a small scale object like a dwarf galaxy, energetic electrons and positrons can pass through the diffusion radius before fully radiating their energies [101, 108]. Detailed analysis of the solution to Eq. 2.2.1 and effects of various parameters will be discussed in Chapter 4.

2.3 Emissivity and final radio flux

For relativistic $e^{\pm}$, dominant DM induced photon signal at radio frequencies arises in terms of the synchrotron radiation. In the presence of a galactic magnetic field B, the energetic electrons(positrons) move in a cycloid motion and emit synchrotron radiation at a rate which is governed by the synchrotron power. For a emission frequency ν that is much above the non-relativistic gyro-frequency and the plasma frequency, the synchrotron power (averaged over the directions of emission) is given by [101, 108, 109, 128, 140],

$$P_{Synch}(\nu, E, B) = \sqrt{3} r_0 m_e c \nu_0 \int_0^{\pi} d\theta \frac{sin\theta}{2} 2\pi\, sin\theta\, F\left(\frac{x}{sin\theta}\right). \tag{2.3.1}$$

Here θ is the pitch angle and r_0 $(= \frac{e^2}{m_e c^2})$ and ν_0 $(= \frac{eB}{2\pi m_e c})$ denote, respectively, the classical electron radius and the non-relativistic gyro-frequency. Respective forms of x and F are,

$$x \equiv \frac{2\nu m_e^2}{3\nu_0 E^2}\left[1 + \left(\frac{E\nu_p}{m_e \nu}\right)^2\right]^{3/2}, \tag{2.3.2}$$

where ν_0 $(\simeq 9 \left(\frac{n_e}{\mathrm{cm}^{-3}}\right)^{1/2}$ KHz) is the plasma frequency, and

$$F(s) \equiv s \int_s^{\infty} d\eta K_{5/3}(\eta) \simeq 1.25 s^{1/3} \exp(-s) \left[s^2 + 648\right]^{1/12}. \tag{2.3.3}$$

The synchrotron emissivity, induced by the electrons and positrons generated from DM annihilation inside a galaxy or a galaxy cluster, is obtained by folding the equilibrium $e^{\pm}$ density $\frac{dn}{dE}(r, E)$ with the synchrotron power P_{Synch} as [101, 108, 109, 128],

$$J_{Synch}(\nu, r) = 2 \int_{m_e}^{m_\chi} dE \frac{dn}{dE} P_{Synch}(\nu, E, B). \tag{2.3.4}$$

Here a factor of 2 has been multiplied to take into account the contributions of both electron and positron. Note that a high B-field increases the synchrotron power and thus produces a large emissivity. Using the emissivity, one can calculate the corresponding surface brightness distribution $I(\nu, \Theta)$ which is a function of the observed frequency ν and the angle Θ between the line-of-sight (los) l and the direction of the center of the target galaxy or the galaxy cluster:

$$I(\nu, \Theta) = \int_{\text{los}} dl\, J_{Synch}(\nu, r(l, \Theta)). \tag{2.3.5}$$

Finally, the integrated synchrotron flux density $S_\nu(\nu)$ is estimated by integrating the surface brightness over the solid angle Ω corresponding to the emission region of the target, i.e.,

$$S_\nu(\nu) = \frac{1}{4\pi} \int d\Omega\, I(\nu, \Theta). \tag{2.3.6}$$

If the size of the emission region is much smaller than the distance of the target, then Eq. 2.3.6 can be approximated as [108],

$$S_\nu(\nu) = \frac{1}{L^2} \int drr^2 J_{Synch}(\nu, r), \tag{2.3.7}$$

where L is the luminosity distance of the target. Observational prospects for such DM induced radio synchrotron flux in various existing and upcoming radio telescopes as well as its different features resulting due to the effects of individual particle physics and astrophysical parameters will be studied in Chapters 3 - 6.

In addition to the synchrotron emission, electrons and positrons produced from DM annihilation inside a halo can give rise to another type of photon signal via the Inverse Compton (IC) scattering process. In this case, electrons and positrons scatter off the background photon bath present within the halo and lead to a spectrum of energetic photons. If the DM mass is at the GeV/TeV scale, frequencies of the corresponding IC photons are much higher than the usual radio frequencies and therefore can not be detected in radio telescopes [101, 108, 109]. On the other hand, while MeV range DM particles are considered, mildly relativistic $e^\pm$ generated from their pair-annihilations scatter on low energy CMB photons leading to a IC spectrum that falls (at least partially) within the radio frequency range. Such IC fluxes can be estimated by folding the $e^\pm$ density $\frac{dn}{dE}(r, E)$ (originating from MeV DM) with the IC power $P_{\text{IC}}(\nu, E)$ and integrating over the line-of-sight of the target halo. An analytic expression for the IC power, resulting from the scattering of $e^\pm$ on the CMB photons, is given in Appendix A. Further discussion on this topic including the possibility of observing such IC signals using a radio telescope will be carried out in Chapter 7.

2.4 Radio telescopes

Study of DM induced radio signals based on the observations conducted by radio telescopes may enable us to constrain the properties of DM annihilation in a galactic or an extragalactic source and also help us to get better understanding of various astrophysical parameters involved in the production of radio fluxes. There exist a number of radio telescopes, e.g., Australia Telescope Compact Array (ATCA), MeerKAT, Australian SKA Pathfinder (ASKAP), Murchison Widefield Array (MWA), KAT-7, Low-Frequency Array (LOFAR), Green Bank Telescope (GBT), located at different places around the world. They have been studied many times in the literature in the context of various astrophysical and cosmological probes [110, 111, 116, 117, 141, 142]. Apart from these, another radio observation project, namely, the Square Kilometre Array (SKA), has been planned and is expected to start its operation in the forthcoming years [143]. One common feature of every radio telescope is the noise added by the telescope system itself which defines the system sensitivity. The rms noise level of a radio telescope can be estimated as [111, 144, 145],

$$N_{rms} = \frac{\sqrt{2} K_B T_{sys}}{A_{eff}\sqrt{\Delta\nu\, \Delta t}}, \tag{2.4.1}$$

where K_B is the Boltzmann's constant, A_{eff} is the effective area of the telescope, $\Delta\nu$ is the frequency bandwidth and Δt is the observation time. The parameter T_{sys} is the system temperature which takes contributions from microwave and galactic backgrounds, atmospheric emission, spill-over, antenna receiver etc. In this thesis, we have mostly used the upcoming Square Kilometre Array (SKA) and the Murchison Widefield Array (MWA) radio telescopes for the DM related study. We provide below a short description of these two telescopes.

A projected mega-telescope: the square Kilometre Array (SKA)

The SKA is an upcoming radio telescope proposed to be built in Australia and South Africa. It is expected to play an important role in various fields of cosmology and astrophysics including the studies of DM [146–148]. The main advantage of the SKA lies not only in its capability of observing radio signal for a large frequency range (50 MHz - 50 GHz) which helps to constrain DM for a wide mass domain, but also in its inter-continental baseline lengths which can well resolve the astrophysical foregrounds. The SKA has a large effective area which helps it to obtain a significantly high surface brightness sensitivity [143]. For example, with a typical bandwidth of 300 MHz, the value of its rms noise level for 1 GHz frequency and 100 hours of observation time is $\sim 10^{-7}$ Jy [2], which corresponds to a two order of magnitude gain in the sensitivity with respect to other radio observations [111]. Due to such high sensitivity, the SKA can improve the existing bounds on DM properties; we will discuss this thoroughly in Chapters 3, 4 and 7.

A precursor to the SKA: the Murchison Widefield Array (MWA)

The MWA radio telescope, a precursor to the SKA, is a part of the Murchison Radio-astronomy Observatory located at Western Australia. It operates in the frequency range 80 - 300 MHz with a maximum baseline length of few Km [149]. The size of the Phase I MWA beam in the frequency range used for our work (i.e., ~ 200 MHz) is approximately 2 arcmin. The proposed Phase II survey is expected to provide an improvement in the beam size by several factors, leading towards the possibility of a deeper probe of the extra-terrestrial radio signals. Detailed analysis of the MWA radio data and the resulting constraints on the DM parameter space are presented in Chapters 5 and 6. While analysing the MWA data, we have used the observation of another radio telescope, namely, the Giant Metre-wave Radio Telescope (GMRT) [150], whose relatively small field of view helped us to subtract the point sources from diffuse radio structures of interest.

[2] 1 Jy = 10^{-23} erg cm^{-2}s^{-1}Hz^{-1}.

Chapter 3

Can SKA–Phase 1 go much beyond the LHC in supersymmetry search?

3.1 Introduction

In this chapter, we show that the upcoming radio telescope, Square Kilometre Array Phase 1 (SKA1), can well surpass the Large Hadron Collider (LHC) reach in unveiling new physics responsible for dark matter (DM). The physics features of the conclusions are general in nature, as will become more evident from the discussions in the next chapter. However, we use in this chapter as illustration the minimal supersymmetric standard model (MSSM) where the lightest neutralino (χ_1^0) is the DM candidate (i.e., $\chi_1^0 \equiv \chi$). We recall from our discussion in Chapter 1 that the LHC is unlikely to see signatures of supersymmetry (SUSY) for $m_{\chi_1^0} \gtrsim 1$ TeV, especially for coloured superparticle masses above $\simeq$3 TeV [60, 151–153]. However, DM annihilation in dwarf spheroidal (dSph) galaxies can lead to radio synchrotron emission which clearly rises above the SKA1 detection threshold with 10-100 hours of observation, for $m_{\chi_1^0}$ up to at least 10 TeV. We scan the MSSM parameter space and predict the synchrotron radiation spectra for three such galaxies, for DM annihilation corresponding to the aforesaid SUSY breaking scales. Even with conservative parameter values, the SKA1 should see signals, for DM masses one order higher than the reach of the LHC with $\int \mathcal{L} dt = 3000$ fb^{-1} [60, 151–153].

As has been outlined in Chapter 2, the SKA1 is expected to address many important questions in astrophysics and cosmology [146]. It has relevance in the physics of elementary particles, too. Foremost in this context is the issue of DM, provided it is constituted of elementary particle(s). While there is no unique candidate theory yet, the MSSM shows a logically satisfactory way to obtain a stable neutral particle, especially the lightest neutralino (χ_1^0), which satisfies the requirements of DM. As mentioned in Chapter 1, the LHC, however, has not found any signals of it so far, up to coloured new particle masses $\gtrsim$ 2 TeV [154,155]. On the other hand, spectra in the multi-TeV range can be phenomenologically allowed and satisfy all requirements of DM, if one defers judgements on the somewhat fuzzy issue of naturalness. While the LHC cannot see such heavy superparticles, and the fate of any future collider is uncertain, we show below that the SKA1 in its first phase itself can detect diffuse radio synchrotron signals of DM annihilation for such high $m_{\chi_1^0}$.

3.2 Scheme of analysis

As we discussed in Chapter 2, in astrophysical objects like dSph galaxies, DM-pairs annihilate into Standard Model (SM) particles such as $b\bar{b}, t\bar{t}, W^+W^-, \tau^+\tau^-$ etc. The subsequent cascades produce copious e^+e^- pairs whose energy distribution is determined by the source function $Q_e(E, r)$, given in Eq. 2.1.1 as a function of the $e^\pm$ energy E and the distance r from the center of the galaxy. The source function depends on particle physics quantities like $\langle \sigma v \rangle$ (DM annihilation rate in today's universe), DM mass m_χ ($\equiv m_{\chi_1^0}$ in MSSM) and $\frac{dN_f^e(E)}{dE}$ (which denotes the energy distribution of the $e^\pm$ produced per annihilation in any of the aforementioned annihilation channels which has a finite weightage B_f). It also involves the astrophysical quantity $\rho_\chi(r)$ that represents the DM density profile of the target galaxy. Here we have considered three dSph galaxies, namely, Draco, Ursa Major II and Segue 1. We have used the NFW profile [125] for Draco [108, 128] and Ursa Major II [116], and the Einasto profile [126] for Segue 1 [117], with the parameters of the profile chosen such that they are consistent with the kinematical observations of these galaxies [122,123]. For detailed information on these DM profiles see Chapter 2.

Prediction of the synchrotron signal produced by the e^+e^- pairs (generated in DM annihilation) requires tracking their propagation through galactic media. This process is governed by Eq. 2.2.1 ([101, 108]) shown in Chapter 2. The solution of this equation, $\frac{dn}{dE}(E, r)$, describes the steady state $e^\pm$ distribution and depends on two important astrophysical parameters $b(E)$ and $D(E)$. The parameter $b(E)$ denotes the energy loss due to various radiative processes like the inverse Compton scattering, synchrotron radiation (which involves the ambient magnetic field B), Coulomb losses and bremsstrahlung. The other parameter $D(E)$ characterizes the diffusion in the system and is assumed to have the Kolmogorov form

$D(E) = D_0 E^\gamma$ [108, 116, 117, 128], D_0 being the diffusion coefficient. One finally obtains the frequency spectrum (S_ν) of observed photons by folding $\frac{dn}{dE}$ with the synchrotron power spectrum (whose mathematical expression is provided in Chapter 2 ([101, 108, 109])) and integrating over the line-of-sight of the target dSph.

Nearby ultra-faint dSphs are appropriate for studying such diffuse radio signals as their low star formation rate minimises the uncertain contribution of astrophysical processes. Their relative proximity (most of them are satellites of the Milky Way) and high DM content, as inferred from the observed mass-to-light ratios within their half-radii, are of further advantage. Some of these dSphs have been observed using existing radio telescopes with the aim of recording such diffuse emission, although no signal has materialised so far [110,111,116,117,156]. The ultra-faint nature of these galaxies necessitates a more sensitive telescope like SKA1 for detecting the radio synchrotron signal [148]. Here we predict the diffuse signal considering the parameters for Draco dSph mainly because the various relevant parameters like the J-factor are better constrained for this object [122], though even higher flux is expected out of the nearer dSphs such as Segue 1 and Ursa Major II, as shown later in this chapter.

3.3 Results and discussions

For a χ_1^0 DM in MSSM, the observed radio flux (obtained via the velocity averaged quantity $\langle \sigma v \rangle$ (calculated using micrOMEGAs 4.3.1 [157])) depends on not only $m_{\chi_1^0}$ but also the particle spectrum and other MSSM parameters that determine the annihilation rates and branching ratios, and also the energy of $e^\pm$ transported across the dSph. Some recent works [108, 148, 158] have treated m_χ and $\langle \sigma v \rangle$ as two free parameters, and studied the consequences of different 'dominant' annihilation channels. We instead select various MSSM benchmark regions, especially those with heavy superparticles undetectable at the LHC [60, 151–153], and use the full dynamics of the model in terms of the emergent annihilation channels. These benchmarks are listed in Tables 3.1 and 3.2. There are four broad classes. (A) has all squarks/gluinos and sleptons well above LHC detection limits, but with a hierarchy between squarks and sleptons. (B) includes somewhat lighter but still undetectable superparticles, but with no hierarchy between coloured and colourless ones. (C) and (D) have similar spectra as in (A) and (B) but with lighter top squarks in each case. (E) and (F) correspond to ultra-high χ_1^0 masses close to 10 TeV. These regions identify DM candidates beyond the commonly conceived domain of naturalness. Further categories within each class reflect different combinations of other MSSM parameters which drive annihilation in different channels. In addition, spectra with χ_1^0 beyond the LHC detection limit have been juxtaposed with relatively light ones for comparison. All benchmarks satisfy the constraints coming from collider [154, 155, 159–161] and direct DM searches [49, 162], relic density [1] [23, 163, 164], lightest neutral Higgs mass [165] (calculated at the two-loop level), flavour physics [166, 167], $(g-2)_\mu$ [168] etc.

Cases	$m_{\widetilde{l}}$ (TeV)	$m_{\widetilde{Q}_{1,2,3}}$ (TeV)	$m_{\widetilde{q_R}}$ (TeV)	A_t (TeV)	$m_{\widetilde{t_R}}$ (TeV)	$m_{\widetilde{g}}$ (TeV)
A	5-5.5	10	10	-2	10	10
B	4-4.5	5	5	-4	5	5
C	4-4.5	5	5	-4	1.95	5
D	5-5.5	10	10	-2	2.05	10
E	10	10	10	-2	10	10
F	15	20	20	-1	20	20

Table 3.1: Parameters characterizing different classes of benchmarks. $m_{\widetilde{l}}$ stands for all three slepton families, except in A1c (see Table 3.2) where $m_{\widetilde{\tau}_1}$ has been fixed at $= 1.03\ m_{\chi_1^0}$ to emphasize the $\tau^+\tau^-$ annihilation channel.

Figure 3.1 shows the minimum $\langle\sigma v\rangle$ required in various channels for detection with 100 hours (bandwidth = 300 MHz) at the SKA1, for the dSph Draco. The corresponding annihilation channel has to dominate in each case, for the lower limit to hold. We also indicate the model-independent upper limits on annihilation rates in these channels as functions of the DM particle mass, obtained from cosmic ray antiproton data [83]. The regions bounded by the upper and lower limits represent the area where DM annihilation in this galaxy can certainly be detected within 100 hours. For Draco, with the NFW profile and a galactic magnetic field (B) of 1.0 μG, $D_0 = 3 \times 10^{28}\text{cm}^2\text{s}^{-1}$ and $\gamma = 0.3$ [128], all of our benchmark points whose samples are shown as black spots (mostly beyond the LHC reach [60, 151–153]) fall in the detectable range. Remarkably, this pushes the radio search limit up to $m_{\chi_1^0} \sim 8.5$ TeV. The reach goes up to even 10 TeV if there is substantial annihilation in the $b\bar{b}$ channel.

[1]We have demanded that the relic density should lie within stipulated *upper and lower limits*, as is expected in a single-component DM scenario. The $\langle\sigma v\rangle$ required for relic density calculation needs to be evaluated in a way appropriate for the decoupling temperature, including co-annihilation channels.

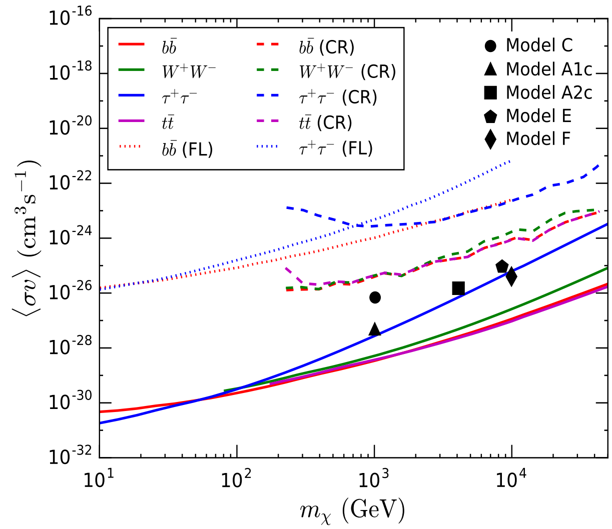

Figure 3.1: Lower limits (solid lines) of observability of radio flux from Draco in the $\langle \sigma v \rangle - m_\chi$ ($m_{\chi_1^0}$ in MSSM) plane at SKA1 with 100 hours, for various DM annihilation channels. Dashed and dotted lines denote the corresponding 95% C.L. upper limits from cosmic-ray (CR) antiproton observation and 6 years of Fermi LAT (FL) data [70] respectively.

The frequency spectra of the predicted radio signals are shown in Figure 3.2. The expected SKA1 sensitivities in the frequency range 350 MHz – 50 GHz [143] are also shown for observations over 10, 100 and 1000 hours.[2] Although the curves are drawn using the NFW profile for Draco, we have checked that the predictions remain very similar for other profiles such as Burkert and D05 [128]. Also, we have assumed no halo substructures which can in principle enhance the flux even further [109]. As per current understanding, significant radio signals from from astrophysical processes are unlikely, as dSphs are mostly devoid of gas and have almost no intrinsic sources of high energy $e^\pm$. The other possible sources of contamination are the astrophysical foregrounds, however, they too are expected to be sub-dominant for the SKA1 as the large baselines will help in resolving out these objects. On the whole, detection is almost certain for each case within 100 hours; there are several benchmark points where even 10 hours should suffice. Note that the flux depends on $m_{\chi_1^0}$, $\langle \sigma v \rangle$ and B_f. Thus MSSM dynamics crucially decides detectability. Overall, the SKA1 clearly goes beyond the LHC in SUSY-DM search [60, 151–153]. As Figure 3.1 shows, a neutralino DM with mass

[2]It is possible that the SKA1 design may undergo minor changes in the future, leading to gaps in the frequency coverage and revisions in the sensitivity estimates. This should not affect our main conclusion, since the predicted signals are well above the sensitivity limits.

on the order of 10 TeV (or perhaps more) may be rendered visible in the process.

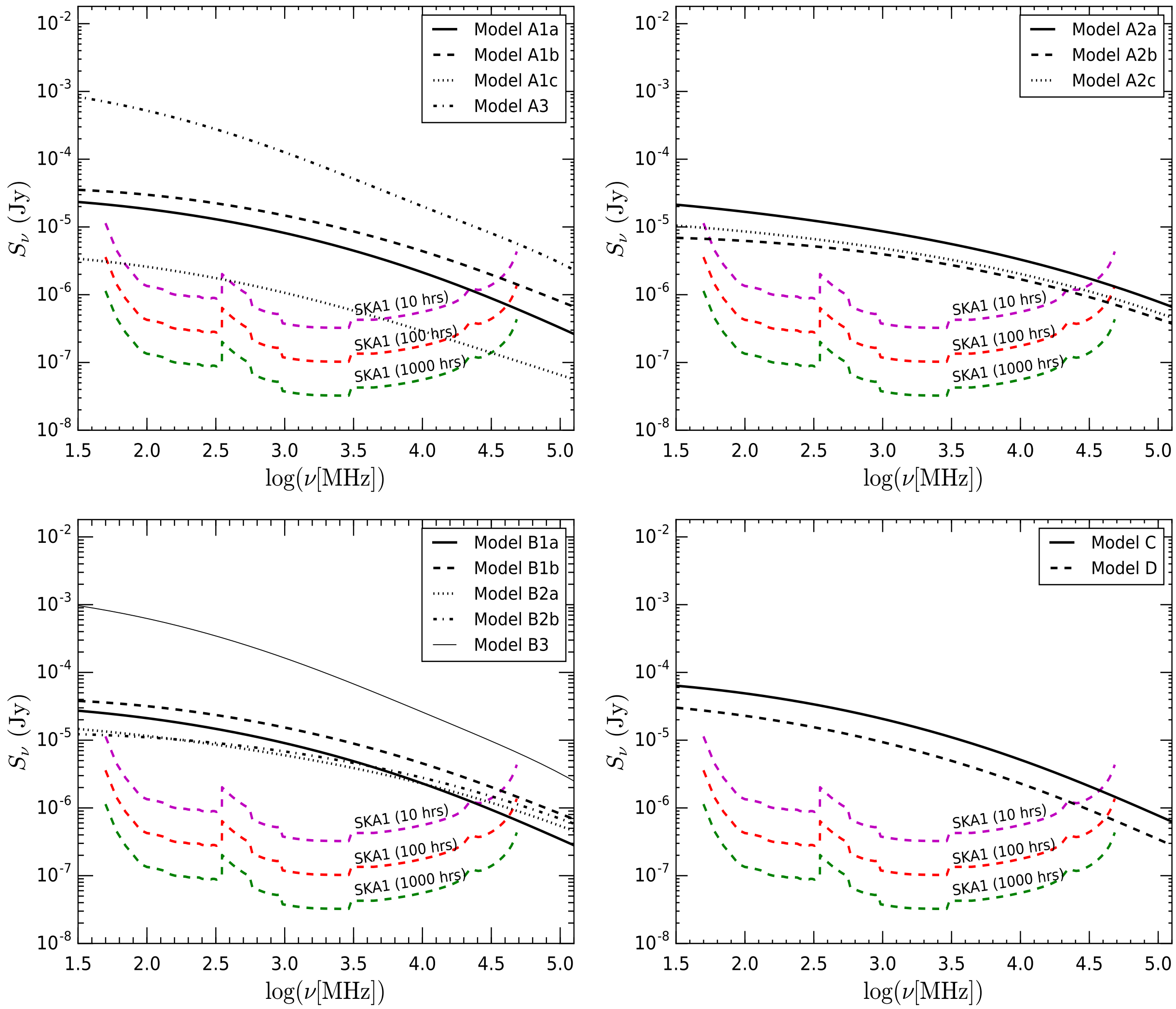

Figure 3.2: Synchrotron fluxes (S_ν, in Jy) for various models (listed in Table 3.1 and 3.2) in the Draco dSph galaxy ($D_0 = 3 \times 10^{28}\mathrm{cm}^2\mathrm{s}^{-1}$, $B = 1\ \mu G$). The SKA1 sensitivity curves for 10, 100 and 1000 hrs are also shown for bandwidth = 300 MHz.

While the above results are presented for $B = 1.0\ \mu G$ (typical of a dSph like Draco where the magnetic field has been measured [169]), the predictions with other values, namely, $B = 10.0$ and $0.1\ \mu G$, are presented in Figure 3.3 (left). We thus see that even for the pessimistic value of $0.1\ \mu G$, the signals are detectable up to $10^{3.4}(10^{3.8})$ MHz for 100 (1000) hours of observation. Figure 3.3 (right) shows the effect of different D_0. We once more include the 'unfavourable' value of $D_0 = 3 \times 10^{29}\mathrm{cm}^2\mathrm{s}^{-1}$, $\gamma = 0.3$, for which detectability should be rather high in the range 10^{2-4} MHz, for a neutralino mass $\sim$ 4 TeV, with the coloured particle masses at 10 TeV.

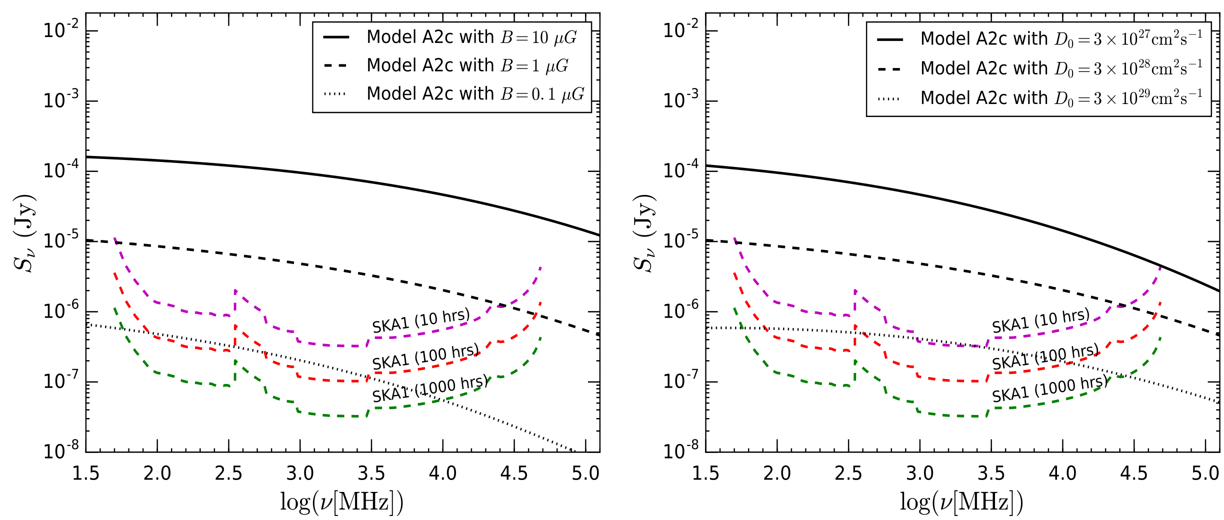

Figure 3.3: *Left:* Synchrotron fluxes for Model A2c for Draco ($D_0 = 3 \times 10^{28}\mathrm{cm}^2\mathrm{s}^{-1}$) with various magnetic fields $B = 10.0$, 1.0 and 0.1 μG. *Right:* Synchrotron fluxes for Model A2c for Draco ($B = 1\ \mu G$) with different $D_0 = 3 \times 10^{27}, 3 \times 10^{28}$ and $3 \times 10^{29}\mathrm{cm}^2\mathrm{s}^{-1}$.

We finally show in Figure 3.4 some predictions for galaxies nearer than Draco, namely, Ursa Major II and Segue 1, with $B = 1.0\ \mu G$, $D_0 = 3 \times 10^{26}\mathrm{cm}^2\mathrm{s}^{-1}$, and appropriate values of γ [108,116,117,128]. Benchmark A1a is used for illustration. While detectability is much above threshold here, a comparison with Draco tells us that Segue 1 and Ursa Major II hold high hopes for DM annihilation detection, even with larger $m_{\chi_1^0}$. Even if SKA1 succeeds in setting upper limits on the flux for for most of our benchmark points, it will be possible to probe and constrain regions of hitherto unexplored regions in the MSSM parameter space well. Observations of the signal in different wavebands, say, radio and γ-ray frequencies, from any dSph may enable also us to break the degeneracies between the MSSM parameters and B, D_0.

Table 3.3 shows the annihilation cross-sections of the χ_1^0 DM for all our benchmark points, for which the corresponding χ_1^0 masses are supplied in Table 3.2. Side by side, the new particles apart from χ_1^0, which play the most crucial roles in annihilation are listed, along with their masses for the corresponding benchmarks. As we can see, such role is mostly played among superparticles by the $\chi_1^\pm$ and χ_2^0 on the one hand, and the $\widetilde{t}_1$, $\widetilde{b}_1$, and $\widetilde{\tau}_1$, on the other. The masses for these particles evidently lie beyond the reach of the LHC for an integrated luminosity of 3000 fb^{-1}.

For some benchmark points, the neutral pseudoscalar Higgs (A^0) has an important role.

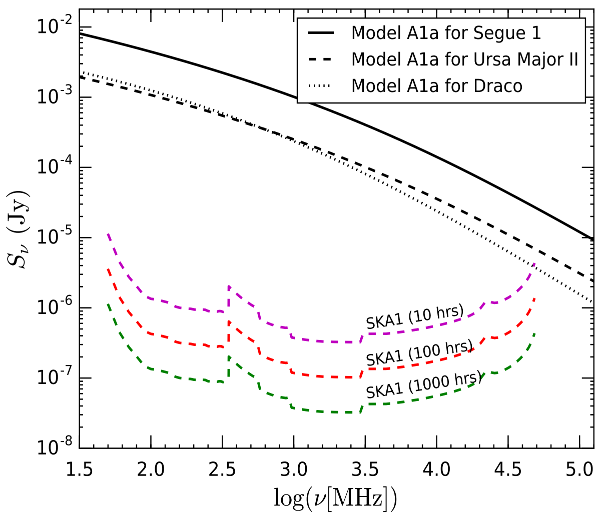

Figure 3.4: Comparison of synchrotron fluxes in Model A1a among Draco, Ursa Major II and Segue 1 with $D_0 = 3 \times 10^{26}\mathrm{cm}^2\mathrm{s}^{-1}$ and $B = 1\ \mu G$.

While the corresponding M_A in each case is currently allowed by all data, they (with the appropriate values of $tan\beta$ as in Table 3.2) are unlikely to be seen in any direct signal even at the high-luminosity run.

It is true that some representative MSSM parameters values have included in our sixteen benchmarks. It is of course possible to carry out a similar analysis with a simplified SUSY model containing fewer free parameters. However, we have not restricted ourselves to such scenarios, since our main point is made more emphatically in the general case. The point is that *the general MSSM parameter space contains a wide range when not only the* χ_1^0 *DM but also the (super)particles responsible for its annihilation within dSph's lie beyond the LHC reach.* This is evident form Table 3.3; one is now looking at scenarios with $m_{\chi_1^\pm}$, $m_{\chi_2^0} \in$ [1150 GeV, 4100 GeV], $m_{\widetilde{\tau}_1} \in$ [1000 GeV, 5500 GeV], $m_{\widetilde{t}_1} \in$ [1750 GeV, 5000 GeV], $m_{\widetilde{b}_1} \simeq 5000$ GeV, $M_A \in$ [670 GeV, 20000 GeV]. All of these (excepting perhaps $M_A \simeq 670$ GeV) are beyond the LHC reach [60, 151–153, 161].

3.4 Conclusions

We thus conclude that the SKA1, mostly with 100 hours of observation, should be able to detect radio synchrotron signals of MSSM DM annihilation, for cases where the superparticle masses are well above the reach of the LHC. Even neutralinoes below a TeV, which the LHC cannot probe due to overwhelming backgrounds, are covered by such observation. This holds even for conservative values of astrophysical parameters, and thus underscores a new potential of the SKA. An analysis in further detail of the physics underlying such optimism is presented in the next chapter.

Model	M_1 (GeV)	M_2 (GeV)	μ (GeV)	M_A (GeV)	$tan\beta$	annihilation channel (with B_f [in %])	$m_{\chi_1^0}$ (GeV)
A1a	1020.0	2000.0	1180.0	2113.0	20	$b\bar{b}(85\%)$, $\tau^+\tau^-(14\%)$	1000.6
A1b	2097.2	-3536.3	1134.8	7022.6	20	$W^+W^-(55\%)$, $ZZ(45\%)$	1163.0
A1c	1030.0	3000.0	1150.0	2200.0	5	$\tau^+\tau^-(38\%)$, $t\bar{t}(37\%)$, $b\bar{b}(22\%)$, $W^+W^-(1.7\%)$, $ZZ(1.3\%)$	1006.7
A2a	3932.4	3645.7	-3427.5	7001.2	20	$b\bar{b}(76\%)$, $\tau^+\tau^-(15\%)$, $t\bar{t}(4\%)$, $W^+W^-(3\%)$, $ZZ(2\%)$	3459.4
A2b	5537.0	-2976.8	-3372.3	6517.9	20	$W^+W^-(91\%)$, $b\bar{b}(7.6\%)$, $\tau^+\tau^-(1.4\%)$	3085.4
A2c	4477.6	3977.5	4330.9	8293.9	20	$b\bar{b}(53.4\%)$, $W^+W^-(35\%)$, $\tau^+\tau^-(11\%)$	4090.6
A3	-312.0	1000.0	400.0	690.8	10	$t\bar{t}(79.4\%)$, $b\bar{b}(16.3\%)$, $\tau^+\tau^-(2.2\%)$, $W^+W^-(1\%)$	302.0
B1a	-1013.8	2022.0	1150.0	2113.0	20	$b\bar{b}(72\%)$, $t\bar{t}(16\%)$, $\tau^+\tau^-(12\%)$	1000.0
B1b	-3884.7	3550.0	1132.7	3627.7	20	$W^+W^-(55\%)$, $ZZ(45\%)$	1153.4
B2a	-3485.5	4177.9	3354.3	6820.0	20	$b\bar{b}(76\%)$, $\tau^+\tau^-(15\%)$, $W^+W^-(3\%)$, $t\bar{t}(3\%)$, $ZZ(2.8\%)$	3368.0
B2b	-3930.2	-2598.1	-2957.	5752.4	20	$W^+W^-(94.2\%)$, $b\bar{b}(5\%)$	2662.0
B3	-295.0	1000.0	400.0	668.0	20	$b\bar{b}(50\%)$, $t\bar{t}(42\%)$, $\tau^+\tau^-(7\%)$	286.0
C	-1012.0	3000.0	2000.0	2033.5	10	$b\bar{b}(63.6\%)$, $t\bar{t}(26\%)$, $\tau^+\tau^-(10.2\%)$	1012.4
D	1015.0	3000.0	2000.0	2047.0	10	$b\bar{b}(60\%)$, $t\bar{t}(30\%)$, $\tau^+\tau^-(10\%)$	1015.4
E	8600.0	10000.0	8500.0	17035.0	20	$b\bar{b}(79.1\%)$, $\tau^+\tau^-(18.3\%)$, $t\bar{t}(2.5\%)$	8498.0
F	11000.0	9700.0	9965.0	20000.0	20	$b\bar{b}(78.5\%)$, $\tau^+\tau^-(17.8\%)$, $t\bar{t}(1.9\%)$, $W^+W^-(1.6\%)$	9947.4

Table 3.2: Parameters in different benchmark Models within the classes listed in Table 3.1, and the corresponding DM masses and annihilation channels.

Model	$\langle\sigma v\rangle$ $(10^{-26}\mathrm{cm}^3\mathrm{s}^{-1})$	BSM particles dominantly responsible for annihilation, and their masses(GeV)
A1a	0.27	$A^0(2113.0)$, $\widetilde{\tau}_1(5497.0)$
A1b	0.77	$\widetilde{\chi_1^{\pm}}(1163.5)$, $\widetilde{\chi_2^0}(1163.4)$
A1c	0.05	$\widetilde{\tau}_1(1037.0)$, $A^0(2200.0)$
A2a	1.76	$A^0(7001.2)$, $\widetilde{\tau}_1(5490.0)$
A2b	1.01	$\widetilde{\chi_1^{\pm}}(3085.5)$, $A^0(6517.9)$
A2c	1.47	$A^0(8293.9)$, $\widetilde{\chi_1^{\pm}}(4090.8)$, $\widetilde{\tau}_1(5487.2)$
A3	1.16	$A^0(690.8)$
B1a	0.3	$A^0(2113.0)$, $\widetilde{b}_1(5159.4)$, $\widetilde{t}_1(5047.0)$, $\widetilde{\tau}_1(4496.7)$
B1b	0.79	$\widetilde{\chi_1^{\pm}}(1153.8)$, $\widetilde{\chi_2^0}(1154.8)$
B2a	1.19	$A^0(6820.0)$, $\widetilde{b}_1(5150.6)$, $\widetilde{\tau}_1(4488.3)$, $\widetilde{t}_1(5015.2)$
B2b	1.3	$\widetilde{\chi_1^{\pm}}(2662.2)$, $A^0(5752.4)$
B3	1.3	$A^0(668.0)$
C	0.69	$A^0(2033.5)$, $\widetilde{t}_1(2041.0)$, $\widetilde{b}_1(5085.5)$, $\widetilde{\tau}_1(4497.3)$
D	0.31	$A^0(2047.0)$, $\widetilde{t}_1(1788.0)$, $\widetilde{\tau}_1(5497.5)$
E	9.12	$A^0(17035.0)$
F	3.83	$A^0(20000.0)$

Table 3.3: Annihilation rates ($\langle\sigma v\rangle$) for all the benchmark points along with the list of (super)particles dominantly responsible for χ_1^0 DM annihilation for any particular benchmark point.

Chapter 4

Heavy dark matter particle annihilation in dwarf spheroidal galaxies: radio signals at the SKA telescope

4.1 Introduction

Detectability of the weakly interacting massive particle (WIMP) dark matter (DM) candidate at colliders and also in direct search experiments, depends on its mass as well as its interaction cross-section. In particular, detection becomes rather difficult if the WIMP mass approaches a TeV [49, 60, 162]. While a near-TeV DM particle still admits of some hope at the LHC in the minimal supersymmetric standard model (MSSM) [60, 151–153], the reach is considerably lower for most other scenarios where the 'dark sector' is at most weakly interacting [63, 64]. On the other hand, the annihilation of such heavy DM particles in our galaxy as well as in extra-galactic objects leads to gamma-ray signals [102–106, 170, 171] as well as positrons, antiprotons etc [96–99]. Constraints have been imposed on DM annihilation rates in various ways out of the (non)-observation of such signals [70, 71, 83, 172]. As we have discussed in Chapters 2 and 3, an alternative avenue to explore is that opened by radio synchrotron emission from galaxies, arising out of electron-positron pairs generated from DM annihilation [110, 116, 117, 156].

While the prospect of radio fluxes unveiling DM annihilation has been explored in earlier works [110, 111, 116, 117, 148, 156, 173], it was pointed out in Chapter 3 that the upcoming Square Kilometre Array (SKA) radio telescope [143] opens up a rather striking possibility [174]. The annihilation of trans-TeV DM pairs in dwarf spheroidal (dSph) galaxies lead to electron-positron pairs which, upon acceleration by the galactic magnetic field, produces such radio synchrotron emission. dSph's are suitable for studying DM, since star formation rates there are low [175, 176], thus minimising the possibility of signal originating from astrophysical processes. Their generic faintness prompts one to concentrate on such galaxies which are satellites of the Milky Way. The SKA can ensure sufficient sensitivity required to detect the faint signal from the sources, and at the same time, will have high enough resolution to remove the foregrounds [143]. It was shown in Chapter 3 that about 100 hours of observation at the SKA can take us above the detectability threshold for radio signals from the annihilation of DM particles in the 5-10 TeV range [174]. Of course, the compatibility of such massive WIMP with the observed relic density [23] requires a dark sector spectrum with enough scope for co-annihilation in early universe, as was demonstrated in Chapter 3 in the context of the MSSM [174]. What one learns from such an exercise is that the probe of at least some DM scenarios should thus be possible on a time scale comparable with the running period of the LHC, and that the reach of the LHC [60, 151–153] for WIMP detection may be exceeded considerably through such a probe. It was also found that cases where SKA could observe radio fluxes from a dSph were consistent with limits from γ-ray observations [70] as well as antiparticles in cosmic rays [83].

In order to ascertain which scenarios are more accessible in such radio probes, one needs to understand in detail the mechanisms whereby high-mass DM particles can produce higher radio fluxes, and also the effects of astrophysical processes that inevitably affect radio emission. This is the task undertaken in the present chapter.

The spectrum as well as the dynamics of the particle physics scenario, along with the DM profile in a dSph, is responsible for DM annihilation as well as the subsequent cascades leading to electron-positron pairs.[1] The electron(positron) energy distribution at the source function level is also the determined by the above factors [101, 108, 177]. However, they subsequently pass through the interstellar medium (ISM) of the galaxy, facing several additional effects.

[1]In principle, electron-positron pairs may also be directly produced in a complete model-independent scenario. We have referred to cascade since our benchmarks (shown in Chapter 3) correspond to $b\bar{b}, t\bar{t}, W^+W^-$ and $\tau^+\tau^-$ as dominant annihilation channels, inspired by the MSSM where direct e^+e^- is not found to dominate for high DM masses.

As discussed in Chapter 2, these include diffusion as well as electromagnetic energy loss in various forms, including Inverse Compton effect, Synchrotron loss, Coulomb effect and Bremsstrahlung effect [101, 108, 109, 128]. Besides, the galactic magnetic field is operative all along. The way these affect the final e^+e^- energy distribution is highly inter-connected and nonlinear. For example, while the magnetic field causes electrons to lose more energy in synchrotron radiation, it puts a check on the reduction of the flux through diffusion by confining them longer within the periphery of the dSph. This check applies to electrons at lower energies at the cost of those at higher energies. Also, electromagnetic energy loss enhances the population of low-energy electrons and positrons, the enhancement being more when they have higher kinematic limits, enabled by higher mass of the DM particle. Such low-energy e^+e^- pairs enhance the flux in the frequency range appropriate for a radio telescope.

In the following sections, we analyse the various ingredients in the radio flux generation process, as outlined above. We first do this for fixed DM particle masses, and for values of their annihilation cross-sections fixed by hand. The relative strengths of the effects of the particle theoretical scenario as well as diffusion and radiative process are thus assessed. This also serves to evolve an understanding of the dependence on the diffusion coefficient, parameters involved in electromagnetic energy loss, and, of course, the strength of the galactic magnetic field. If the nature of the DM particle(s) is known in independent channels, then the observation of the observed radio flux may be turned around to improve our understanding of these astrophysical parameters, using the results presented here.

Finally, we use some theoretical benchmark points from Chapter 2 to demonstrate the usefulness of the SKA in probing trans-TeV DM. A few sample MSSM spectra are used, largely because they offer the scope of co-annihilation that is so essential for maintaining the right relic density [174]. Using the minimum annihilation cross-section required for any DM mass for detection at SKA (in 100 hours), and the maximum value of this cross section that is compatible with limits from γ-ray and cosmic-ray data, we show that several benchmark points with DM mass in the 1-8 TeV range, which are yet to be ruled out by any observation can be investigated in 100 hours of SKA observation. In parallel, we also demonstrate how in some of these cases the combined effects of particle physics and various astrophysical processes can help the heavier DM particles to produce radio signals stronger (over the entire SKA frequency range) than those originating from the lighter ones.

We have organised the chapter as follows. In section 4.2 we recapitulate in somewhat brief manner the essential processes for the production of synchrotron fluxes from DM annihilation inside a dSph. In section 4.3 we have analysed the effects of various astrophysical parameters in different steps of the production of radio flux. Section 4.4 describes the features of heavy DM. In section 4.5 we have shown the detectability curves or threshold limits for observing radio flux in SKA, in both model independent as well as model dependent way. We have also shown the final radio fluxes for some theoretical benchmarks. Finally in section 4.6 we conclude.

4.2 Essential Processes

Since one of the main goals of the present chapter is to analyse numerous effects caused by various particle physics and astrophysical phenomena in generating radio signals, we start with a brief resume of sequence of processes that leads to radio flux from a dSph, as discussed in detail in Chapter 2 ([101, 108, 109, 116, 117, 128]). We know that dark matter pair annihilation inside of a dSph can produce SM particle pairs such as $b\bar{b}, \tau^+\tau^-, W^+W^-, t\bar{t}$ etc. These particles then cascades and give rise to large amount of $e^{\pm}$ flux. The resulting energy distribution of which can be obtained from the source function $Q_e(E, r)$ provided in Eq. 2.1.1 ([108, 177]). It is determined by the following quantities: DM annihilation rate $\langle\sigma v\rangle$, DM mass m_χ, weightage or branching fraction B_f of the annihilation channels and $N_{pairs}(r)\left(= \frac{\rho_\chi^2(r)}{2m_\chi^2}\right)$ which denotes the number density of DM pairs inside the dSph. The differential distribution $\frac{dN_f^e(E)}{dE}$ in the equation of the source function estimates the number of $e^{\pm}$ produced with energy E per annihilation in any of the aforementioned SM channels f. For our analysis we have taken Draco[2] dSph assuming a Navarro-Frenk-White (NFW) profile [125] (see Chapter 2), with the values of the halo scale density and halo scale radius as, $\rho_s = 1.4$ GeVcm^{-3} and $r_s = 1.0$ kpc, respectively [108, 128].

Figure 4.1 shows the electron energy distribution for four different annihilation channels ($b\bar{b}, \tau^+\tau^-, W^+W^-, t\bar{t}$) and for two DM masses, namely, $m_\chi = 300$ GeV (*upper left panel*) and 5 TeV (*upper right*). For all cases $\langle\sigma v\rangle$ has been assigned a fixed value (10^{-26}cm^{3}s^{-1}), and the branching fraction corresponding to each channel has been set at 100%. In addition, a comparison between cases with the two above-mentioned masses has also been shown in the lower panel for $b\bar{b}$ and $\tau^+\tau^-$ channels. The predictions for $t\bar{t}$ and W^+W^- fall in between those curves. All these energy distributions are obtained using the micrOMEGAs [120, 121]. Further discussions on these curves will be taken up in section 4.4.

[2]Here we have used the dSph Draco to illustrate our points, primarily because the relevant parameters such as the J-factor are somewhat better constrained for this object [122]. However, similar conclusions apply to other dSph's such as Seg1, Carina, Fornax, Sculptor etc. [122, 123, 178]

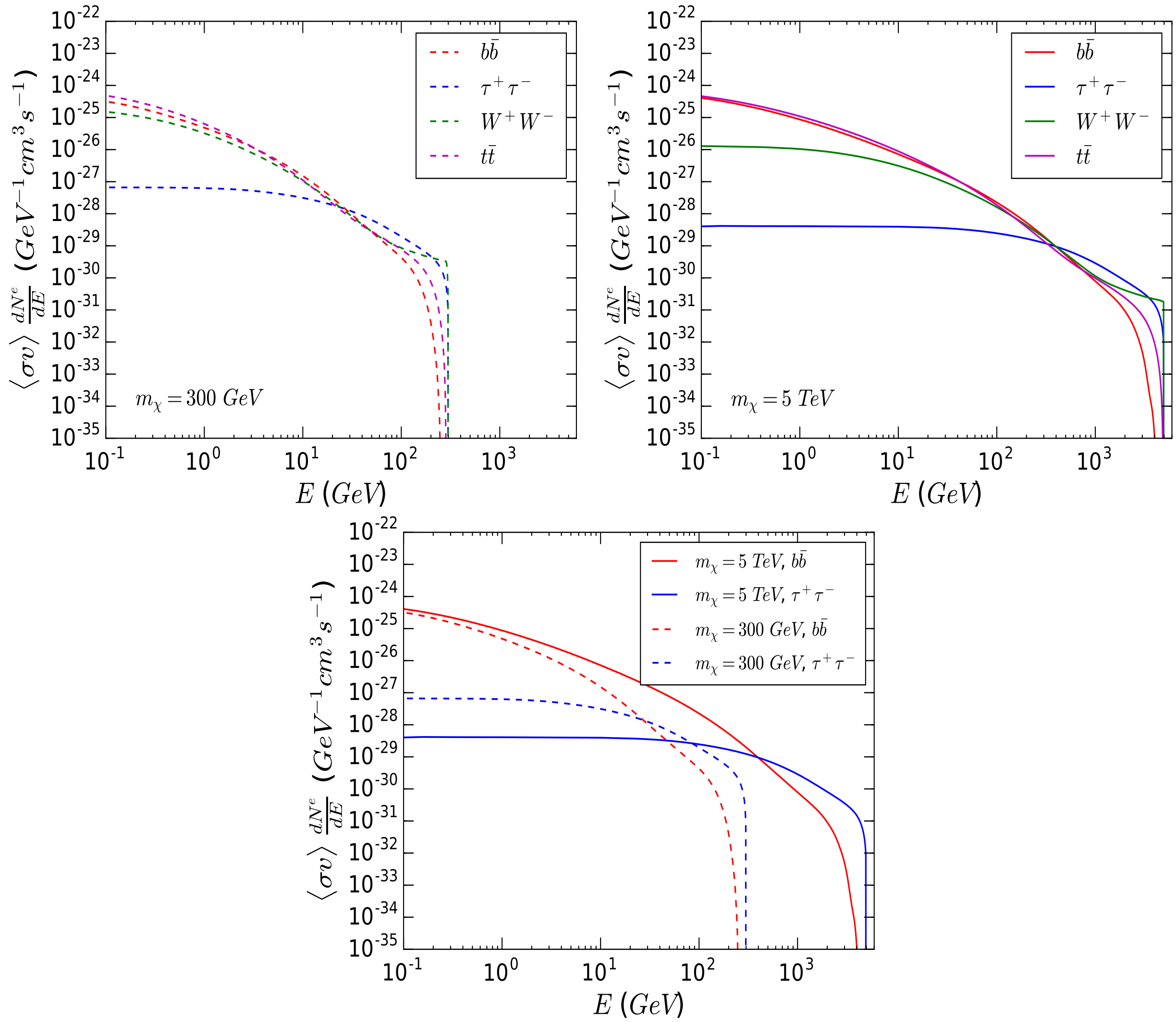

Figure 4.1: *Upper panel:* Source functions per unit annihilation ($\langle\sigma v\rangle\ \frac{dN^e}{dE}$) vs. electron energy ($E$) in different annihilation channels for two DM masses, 300 GeV (upper left panel) and 5 TeV (upper right panel). *Lower panel:* Comparison of the same for two DM masses, 300 GeV (dashed curves) and 5 TeV (solid curves) in two annihilation channels, $b\bar{b}$ (red lines) and $\tau^+\tau^-$ (blue lines). Annihilation rate for each panel is $\langle\sigma v\rangle = 10^{-26}\mathrm{cm}^3\mathrm{s}^{-1}$.

The propagation of the produced electrons-positrons through the interstellar medium (ISM) in the galaxy follows the mechanism described in Chapter 2. Assuming a steady state and homogeneous diffusion, the equilibrium $e^{\pm}$ distribution $\frac{dn}{dE}$ can be obtained by solving the transport equation 2.2.1 ([101,108,109,116,128,179]) which involves the diffusion parameter $D(E)$ and the energy loss term $b(E)$. As pointed out in section 2.2 of Chapter 2, the exact form of $D(E)$ is not known for dSphs due to their very low luminosity; hence for simplicity, we assume it to have a Kolmogorov spectrum $D(E) = D_0 \left(\frac{E}{\mathrm{GeV}}\right)^{0.3}$, where D_0 is the diffusion coefficient [108, 128, 156]. A choice like $D_0 = 3 \times 10^{28}\mathrm{cm}^2\mathrm{s}^{-1}$ is by and large reasonable for a dSph such as Draco [128], although higher values of D_0, too, are sometimes used as benchmark [111]. We have mostly used $D_0 = 3 \times 10^{28}\mathrm{cm}^2\mathrm{s}^{-1}$, and demonstrated side by side the effect of other values of this largely unknown parameter. Following the explanation in [116,117,137], D_0 for a dSph can also in principle have a value one order lower than that in the Milky Way [180]. However, the present study is not restricted to this value, mainly $D_0 \lesssim 3 \times 10^{28}\mathrm{cm}^2\mathrm{s}^{-1}$. The detectability of the radio flux for higher D_0, too, has been studied by us, as will be seen when we come to Figure 4.13.

As mentioned earlier, the energy loss term $b(E)$ takes into account all the electromagnetic energy loss processes such as Inverse Compton (IC) effect, Synchrotron (Synch) radiation, Coulomb loss (Coul), bremsstrahlung (Brem) etc. Their combined effect is shown in Eq. 2.2.2 ([101, 108, 109]). In a dSph like Draco, the first two terms (i.e. IC and Synch) in the expression of $b(E)$ (Eq. 2.2.2) dominate over the last two terms (i.e. Coul and Brem) for $E > 1$ GeV [116]. $b(E)$ depends on the galactic magnetic field (B) through the synchrotron loss term which goes as B^2. From our discussion in section 2.2 we recall that, due to the lack of observational data, the estimation of the magnetic field properties of dSph is extremely difficult. There are some theoretical arguments which suggest μG level B-fields in the local dSphs galaxies [135]. For the dSph considered here, we have mostly used $B = 1\ \mu G$ [108, 128, 156], but more conservative values like $B \sim 10^{-1} - 10^{-3}\ \mu G$ have also been considered. The manner in which diffusion and electromagnetic processes affect our observables will be discussed in detail in sections 4.3 and 4.5. The overall potential of the SKA in probing regions in the $D_0 - B$ space in a correlated fashion will be reported in section 4.5.

The general solution to the transport equation 2.2.1 can be obtained in terms of the Green's function method, shown in Eq. 2.2.4 and 2.2.5 ([101, 108, 116, 128]), by imposing a boundary condition $\frac{dn}{dE}(r_h) = 0$, where r_h is the radius of the diffusion zone. For Draco, r_h is taken to be 2.5 kpc [108,128]. The Green's function $G(r, \Delta v)$ is a function of the diffusion length scale $\sqrt{\Delta v(E', E)}$ which determines the distance traveled by an electron as it loses energy from E' to E. For the mathematical expression of Δv, see Eq. 2.2.6. For small galaxies like dSphs, the mean value of this length scale is expected to be larger than r_h even for non-conservative choices of D_0 and B. We shall discuss this in detail in section 4.3.

After interacting with the magnetic field B present inside the galaxy, the equilibrium distribution $\frac{dn}{dE}$ emits synchrotron radiation (with frequency ν) at a rate governed by the synchrotron emission power $P_{Synch}(\nu, E, B)$ [101, 108, 109, 128, 179], an analytic expression of which is given in Chapter 2.

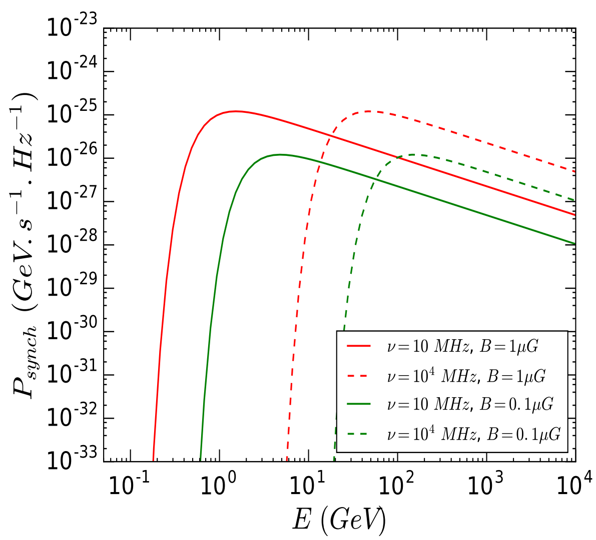

Figure 4.2: Synchrotron power spectrum (P_{Synch}) vs. energy (E) at two frequencies; 10 MHz (solid lines) and 10^4 MHz (dashed lines), with two different magnetic fields; $B = 1$ μG (red) and 0.1 μG (green).

In Figure 4.2, we have shown the dependence of the synchrotron emission power on the electron energy E for two different magnetic fields ($B = 1$ and 0.1 μG) and for two frequencies ($\nu = 10$ and 10^4 MHz). For each frequency shown, it is clear that a stronger magnetic field always intensifies the power spectrum.

Finally, following Eqs. 2.3.4 and 2.3.6, the radio synchrotron flux $S_\nu(\nu)$ (in Jy) can be obtained by folding $\frac{dn}{dE}(r, E)$ with $P_{Synch}(\nu, E, B)$ and integrating over the line-of-sight of the dSph [101, 108, 109, 128, 179].

4.3 Effects of various astrophysical parameters

Let us now take a closer look at the astrophysical effects encapsulated in Eqs. 2.2.1 and 2.2.2. Such effects are driven by the diffusion coefficient D_0 and the electromagnetic energy loss coefficient $b(E)$, which determine the steady state $e^{\pm}$ distribution $\frac{dn}{dE}(r, E)$ for a given $\frac{dN^e}{dE}$. As has been already mentioned, $b(E)$ depends on the galactic magnetic field B.

We use again the two DM masses (m_χ = 300 GeV and 5 TeV) for studying the effects of D_0 and $b(E)$. To have some idea on these effects separately, as well as their contribution in an entangled fashion, we have considered the implication of Eq. 2.2.1 for three different scenarios:

- NSD: considering only the effect of energy loss term $b(E)$ and neglecting the spatial diffusion $D(E)$ (i.e. solution of Eq. 2.2.1 by setting $D(E) = 0$).
- Nb: considering the effect of diffusion parameter D_0 and neglecting the energy loss term $b(E)$ (i.e. solution of Eq. 2.2.1 by setting $b(E) = 0$).
- SD+b: considering the effects of both the diffusion parameter D_0 and the energy loss term $b(E)$ (i.e. the complete solution as explained in Eq. 2.2.4).

For the NSD scenario, solution of Eq. 2.2.1 has a simpler form [101]:

$$\frac{dn}{dE}(r, E)\bigg|_{\text{NSD}} = \frac{1}{b(E)} \int_E^{m_\chi} dE' Q_e(E', r). \tag{4.3.1}$$

Note that, $b(E)$ increases with E (from Eq. 2.2.2). Its effect on the number density in different energy regions is more prominent for this NSD scenario where we neglect the effect of distribution. The number density decreases in the high energy region due to the combined effect of the $\frac{1}{b(E)}$ suppression as well as the lower limit of the integration in Eq. 4.3.1. This can also be seen from Figure 4.3 where we have plotted the ratio of $\frac{dn}{dE}$ and the source function Q_e (which determines the initial electron flux due to DM annihilation) against E. The term $\frac{dn}{dE}\frac{1}{Q_e}$ (in unit of s^{-1}) essentially determines how the shape of the initial distribution Q_e gets modified due to the effect of various astrophysical processes. As discussed in section 4.2, the energy loss term $b(E)$ depends on the square of the magnetic field B through synchrotron loss. Thus $b(E)$ increases with increase of B, which in turn reduces the $\frac{dn}{dE}$ at all E. This phenomenon can also be observed in Figure 4.3 where the red and magenta lines indicate the distributions for $B = 1$ and 10 μG[3], respectively. For comparison, we have also shown the cases for $B = 0.1$ μG (green lines). Note that, the later case coincides with the case for $B = 1$ μG. This is due to the fact that the magnetic field dependence (through synchrotron loss) in the energy loss term $b(E)$ gets suppressed by the Inverse Compton (b_{IC}) term for lower B ($B < 1$ μG), which can be clearly seen from Eq. 2.2.2. Also, for heavier DM masses the energetic electrons are produced in greater abundance (as seen from Figure 4.1) which can lead to a larger $\frac{dn}{dE}\frac{1}{Q_e}$. The effects of two different DM masses, $m_\chi = 300$ GeV and 5 TeV, have been shown in this figure by dashed and solid lines respectively.

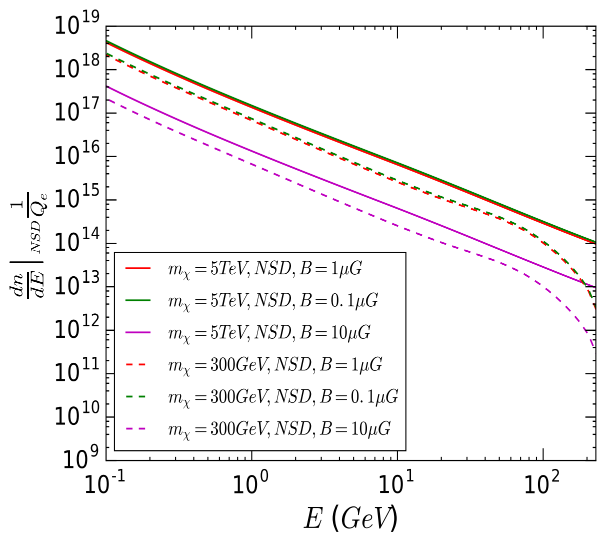

Figure 4.3: $\frac{dn}{dE}\frac{1}{Q_e}$ vs. electron energy E plot for two DM masses, 5 TeV (solid lines) and 300 GeV (dashed lines) with magnetic fields $B = 1$ μG (red), 0.1 μG (green) and 10 μG (magenta) in the scenario where diffusion in the system has been neglected (NSD). Annihilation channel is $b\bar{b}$ with annihilation rate $\langle \sigma v \rangle = 10^{-26} \mathrm{cm}^3\mathrm{s}^{-1}$.

Now, for the Nb scenario, the solution becomes

$$\frac{dn}{dE}(r,E)\Big|_{\mathrm{Nb}} = \frac{1}{D(E)} f(r, r_h) Q_e(r, E), \tag{4.3.2}$$

with the same boundary condition as what we assumed for Eq. 2.2.4. Here

[3] $B = 10$ μG has been used in this Figure for the sake of comparison with 1 μG, just to see the effect of 'large B'. In our prediction on observable radio flux, more conservative (and perhaps realistic) values of B have been used.

$$f(r, r_h) = \int_{r'=r}^{r_h} dr' (\frac{1}{r'^2}) \left\{ \int_{\widetilde{r}=0}^{r'} d\widetilde{r}\, \widetilde{r}^2 \left(\frac{\rho_\chi(\widetilde{r})}{\rho_\chi(r)} \right)^2 \right\}. \tag{4.3.3}$$

Since the effect of $b(E)$ is absent in this case, the distribution $\frac{dn}{dE}$ will not depend on the magnetic field B. Figure 4.4 shows the comparison between the NSD case (cyan lines) and the Nb case (black lines) at two different radii ($r = 0.1$ kpc; left panel and $r = 2$ kpc; right panel) for $B = 1\ \mu G$ and $D_0 = 3 \times 10^{28}\mathrm{cm}^2\mathrm{s}^{-1}$. It is clear from Eq. 4.3.2 that the ratio $\frac{dn}{dE}\frac{1}{Q_e}$ for the Nb scenario will not depend on the initial spectrum Q_e and its energy profile will follow the energy dependence of $\frac{1}{D(E)}$. This presence of $D(E)$ in the denominator leads to $\frac{dn}{dE}\frac{1}{Q_e} \sim E^{-0.3}$ in the limit $b(E) \to 0$. This can also be verified from the relatively flat curves for Nb cases in this figure.

We should mention here that neglecting diffusion is not a bad assumption where the length scale ($\sqrt{\Delta v}$) over which the $e^\pm$ losses energy is much shorter than the typical size of the system [101, 108]. However, for smaller systems like dSphs the effect of diffusion cannot be neglected. This can be justified from Figure 4.4 where we have plotted the SD+b case (i.e. taking diffusion into account along with energy loss effect; shown by red curves) along with the two previously mentioned scenarios. It is clear that the NSD scenario is strikingly different from the one which takes diffusion into account. Addition of diffusion in the system essentially suppresses the $e^\pm$ distribution, especially in the low energy energy region. As a result, the plots for the SD+b case closely match the Nb one at lower energy, but diverge following the NSD scenario at higher energies where the effect of $b(E)$ dominates. This phenomenon can also be explained in terms of the diffusion length scale ($\sqrt{\Delta v}$) which is a result of combined effects of diffusion and energy loss (Eq. 2.2.6). It is indicative of the length covered by an electron as it loses energy from the source energy E' to the interaction energy E and is typically larger than the size of the dSph. In order to determine the minimum energy that an electron can possess before escaping the diffusion radius, we have plotted the interaction energy E vs. $\sqrt{\Delta v}$ in Figure 4.5 for different sets of D_0 and B. The left and right panels correspond to the source energy $E' = 1$ TeV and 100 GeV respectively. The diffusion radius (for Draco) $r_h = 2.5$ kpc is shown by the black solid lines for both cases. The minimum energy is thus calculated from the point where the model crosses this line. A higher D_0 increases this minimum value of interaction energy and as a result reduces the $e^\pm$ number density by making them leave the diffusion zone earlier. Note that, the cases with $B = 0.1\ \mu G$ practically coincide with that for $B = 1\ \mu G$. This is due to the fact that $b(E)$ remains unchanged for $B \leq 1\ \mu G$, as already been mentioned. On the other hand, we have explicitly checked that, a larger value of B (say $B = 10\ \mu G$; not shown in the plot) will help the electron in losing energy more quickly before escaping the diffusion zone, causing a suppression in the number density of high energy electrons and an enhancement of the low energy electrons.

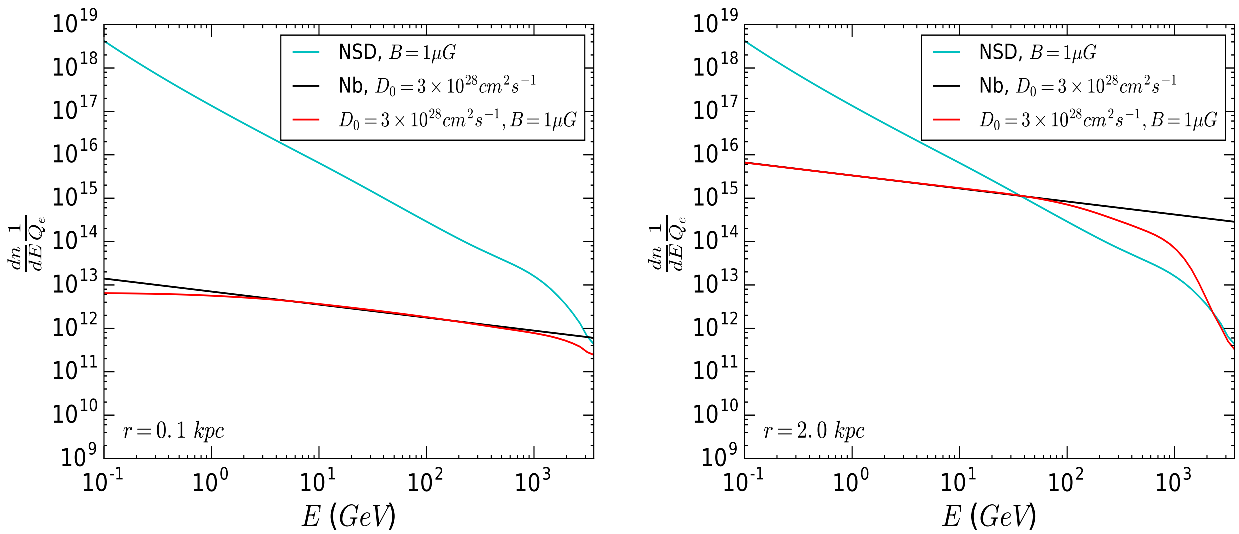

Figure 4.4: $\frac{dn}{dE}\frac{1}{Q_e}$ vs. electron energy E at two different radii, $r = 0.1$ kpc (*left panel*) and $r = 2.0$ kpc (*right panel*) for $m_\chi = 5$ TeV in three scenarios, NSD, Nb and SD+b. Cases including diffusion (Nb and SD+b) have $D_0 = 3\times10^{28}\text{cm}^2\text{s}^{-1}$ and cases including energy loss effect (NSD and SD+b) have magnetic field $B = 1\ \mu G$. For all cases annihilation channel is $b\bar{b}$ with annihilation rate $\langle\sigma v\rangle = 10^{-26}\text{cm}^3\text{s}^{-1}$.

Similar conclusions can also be drawn from Figure 4.6. To illustrate the effects of D_0 and B in the SD+b scenario, we have plotted $\frac{dn}{dE}\frac{1}{Q_e}$ against E for the DM masses 5 TeV (upper panels) and 300 GeV (lower panels) at two different radii 0.1 kpc (left panels) and 2 kpc (right panels). For all cases, the dominant annihilation channel has been assumed to be $b\bar{b}$ with $\langle\sigma v\rangle = 10^{-26}\text{cm}^3\text{s}^{-1}$. Cases with different D_0 and B are indicated by different colors, as mentioned in the insets of the corresponding figures. Similarly, Figure 4.7 shows the variation of the same with respect to radius r for those two DM masses ($m_\chi = 5$ TeV $-$ left panel and $m_\chi = 300$ GeV $-$ right panel). For each DM mass we have assumed two different combinations of energies, one being low ($E = 0.1$ GeV for both DM masses) and the other one is high ($E = 1$ TeV for $m_\chi = 5$ TeV and $E = 100$ GeV for $m_\chi = 300$ GeV). In both panels, the black line indicates the diffusion radius (2.5 kpc) for Draco. One can see that, large D_0 (blue curves) implies a lower density distribution compared to the corresponding

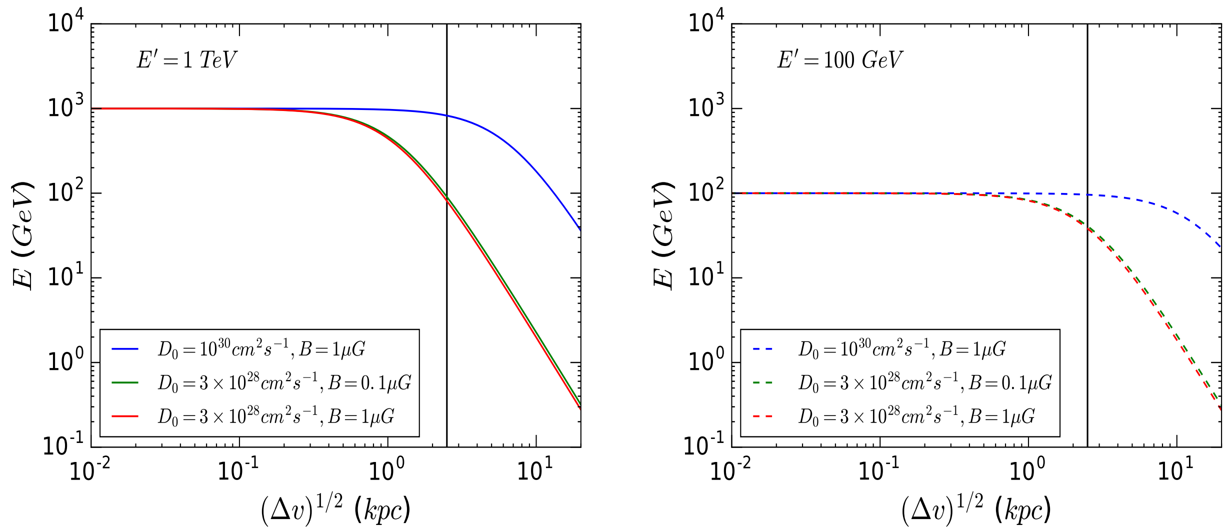

Figure 4.5: Electron interaction energy E (GeV) vs. diffusion length scale $\sqrt{\Delta v}$ (kpc) for two different source energies, $E' = 1$ TeV (*left panel*) and $E' = 100$ GeV (*right panel*). The vertical black solid lines indicate the diffusion size of the galaxy ($r_h = 2.5$ kpc). Here three different sets of astrophysical parameters have been chosen, $D_0 = 3\times10^{28}\mathrm{cm}^2\mathrm{s}^{-1}$, $B = 1\ \mu G$ (red); $D_0 = 10^{30}\mathrm{cm}^2\mathrm{s}^{-1}$, $B = 1\ \mu G$ (blue) and $D_0 = 3\times10^{28}\mathrm{cm}^2\mathrm{s}^{-1}$, $B = 0.1\ \mu G$ (green).

cases with smaller diffusion coefficient. The difference is more prominent for low energy.

The effects of diffusion coefficient and magnetic field on the final radio flux S_ν can be seen from Figure 4.8. The radio flux corresponding to higher diffusion coefficient ($D_0 = 10^{30}\mathrm{cm}^2\mathrm{s}^{-1}$) will be suppressed compared to the lower diffusion case ($D_0 = 3\times10^{28}\mathrm{cm}^2\mathrm{s}^{-1}$) due to the escape of a large number of $e^\pm$ from the stellar object, as discussed above. This suppression is slightly larger in the lower frequency region, since the number density $\frac{dn}{dE}$ decreases more in the low energy regime (see Figure 4.6). For, a constant D_0, say, $3\times10^{28}\mathrm{cm}^2\mathrm{s}^{-1}$, a relatively lower value of B ($0.1\ \mu G$) reduces the radio flux by about an order of magnitude in all frequency ranges. This is solely due to the fact that, although $\frac{dn}{dE}$ has similar values for different values of B (1 and $0.1\ \mu G$), the synchrotron power spectrum P_{Synch} decreases with decrease in B (as evident from Figure 4.2). We further emphasise that, though this analysis assumes an NFW profile for Draco, the choice of other profiles such as Burkert [128, 130] or Diemand et al. (2005) [129] (therefore labeled as D05) [128] keep our predictions similar, as can be seen in Figure 4.9.

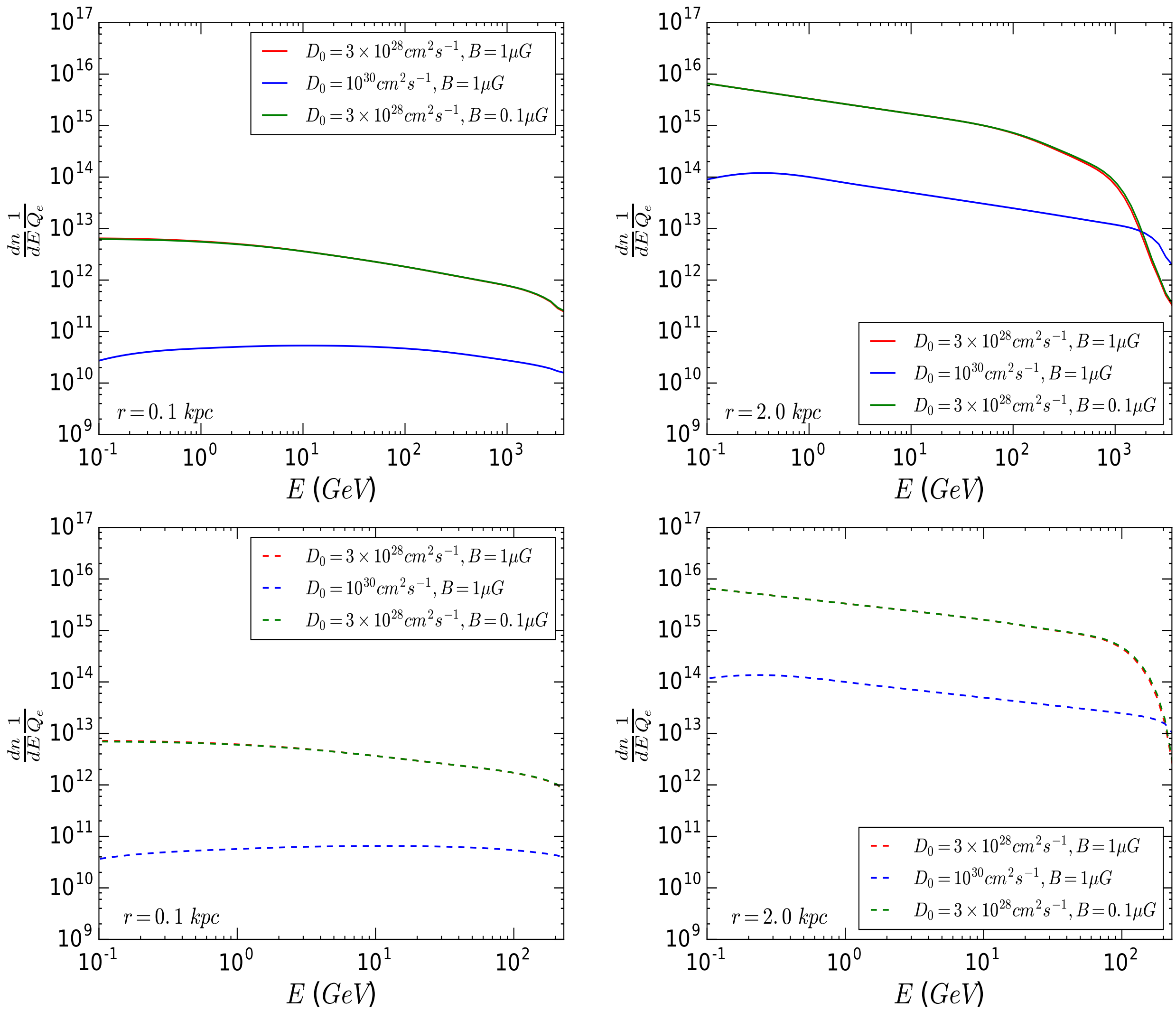

Figure 4.6: $\frac{dn}{dE}\frac{1}{Q_e}$ vs. electron energy E at two different radii, r = 0.1 kpc (*left panel*) and r = 2.0 kpc (*right panel*) for two DM masses, 5 TeV (*upper panels* – solid lines) and 300 GeV (*lower panels* – dashed lines) in the SD+b scenario. Astrophysical parameters considered here have been mentioned in the corresponding legends. For all cases annihilation channel is $b\bar{b}$ with annihilation rate $\langle \sigma v \rangle = 10^{-26}\text{cm}^3\text{s}^{-1}$.

4.4 Heavy DM particles

The radio flux obtained in terms of DM annihilation from a dSph crucially depends on the source function $Q_e(E, r)$ (Eq. 2.1.1). Let us try to explain why one can get higher radio flux (obtained via $\frac{dn}{dE}$ through integration of $Q_e(E, r)$) for higher DM masses in some cases [174]. For this to happen, Q_e corresponding to energetic $e^{\pm}$ is intuitively expected to go up for

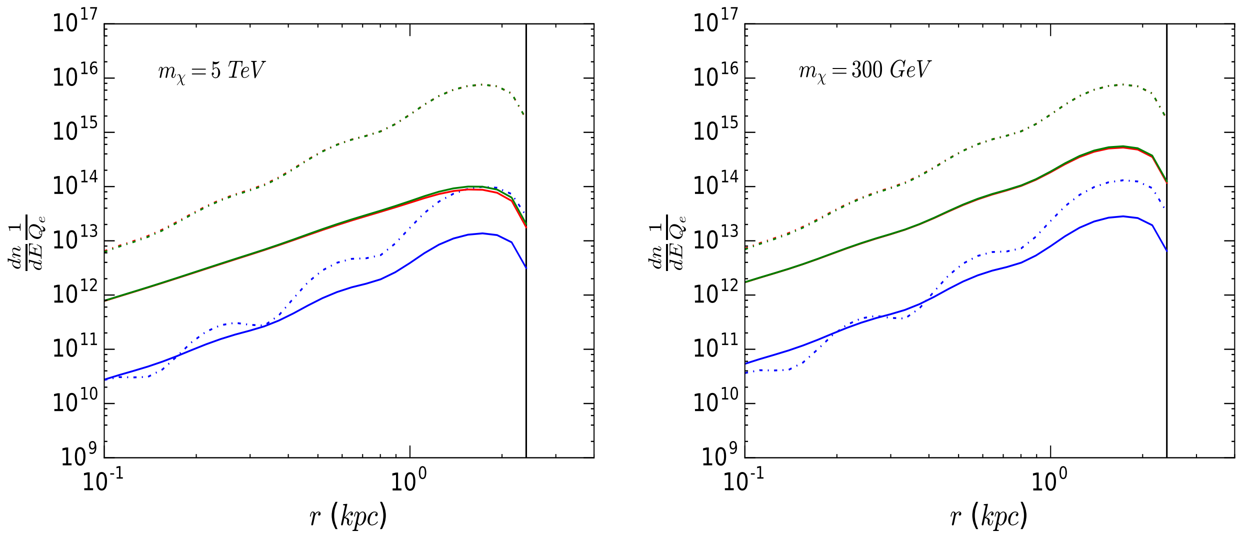

Figure 4.7: *Left panel:* $\frac{dn}{dE}\frac{1}{Q_e}$ vs. r plot for $m_\chi = 5$ TeV at two different electron energies, $E = 0.1$ GeV (dashed dotted lines) and $E = 1$ TeV (solid lines) in the SD+b scenario. The vertical black solid line indicates the diffusion size (r_h) of the dSph. Three different sets of astrophysical parameters have been considered, $D_0 = 3 \times 10^{28}\text{cm}^2\text{s}^{-1}$, $B = 1\ \mu G$ (red); $D_0 = 10^{30}\text{cm}^2\text{s}^{-1}$, $B = 1\ \mu G$ (blue) and $D_0 = 3 \times 10^{28}\text{cm}^2\text{s}^{-1}$, $B = 0.1\ \mu G$ (green). Annihilation channel is $b\bar{b}$ with annihilation rate $\langle\sigma v\rangle = 10^{-26}\text{cm}^3\text{s}^{-1}$. *Right panel:* Same as the *left panel* but at $E = 0.1$ GeV (dashed dotted lines) and $E = 100$ GeV (solid lines) for $m_\chi = 300$ GeV.

higher m_χ. One may consider contributions of several components in the expression of $Q_e(E, r)$:

- $\langle\sigma v\rangle$: For a trans-TeV thermal DM χ, the factors affecting $\langle\sigma v\rangle$ are its mass (m_χ) and the effective couplings to SM particle pairs. While we are concerned here with the annihilation cross sections for χ within a dSph, one also needs consistency with the observed relic density [23]. In general, the expression for the relic density (Ωh^2) indicates inverse proportionality to $\langle\sigma v\rangle$, and $\frac{1}{m_\chi^2}$ occurs as the flux factor in the denominator of the latter [27]. Thus a factor of m_χ^2 occurs in the numerator. Therefore, $m_\chi \gtrsim 1$ TeV may make the relic density unacceptably large. One way to alleviate this is to ensure the possibility of resonant annihilation [27], as is possible in the MSSM through the participation of a pseudoscalar of appropriate mass [113]. This also serves to enhance the observed radio flux, as we shall see later. In addition, the annihilation of χ in the early universe may involve channels other than those in a dSph, through

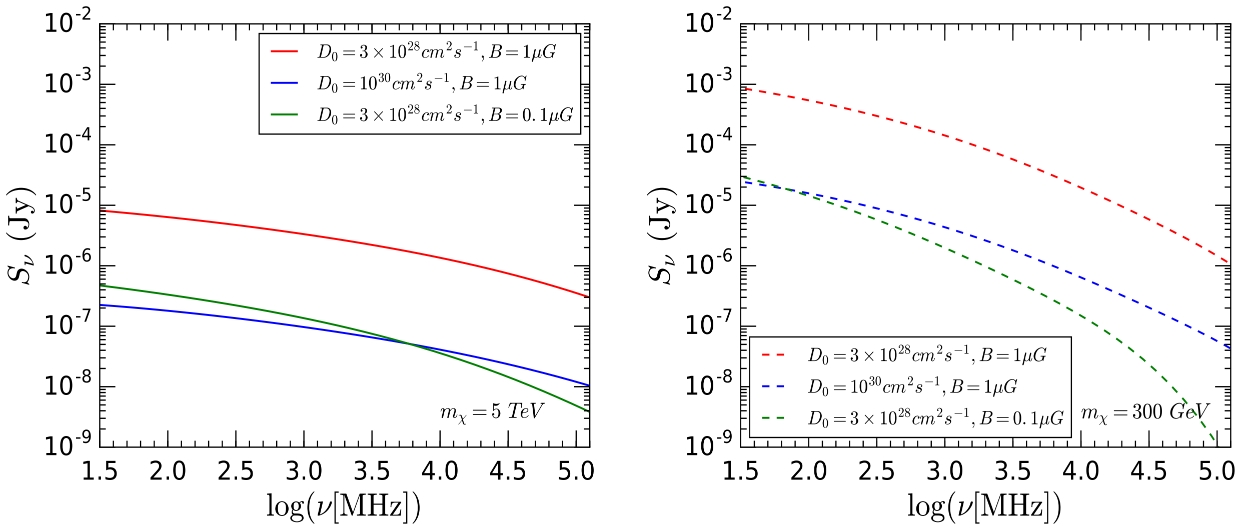

Figure 4.8: Radio synchrotron flux (S_ν) vs. frequency (ν) for two DM masses, 5 TeV (*left panel*) and 300 GeV (*right panel*) with different choices of astrophysical parameters (D_0 and B) mentioned in the legends. Annihilation channel is $b\bar{b}$ with annihilation rate $\langle \sigma v \rangle = 10^{-26}\mathrm{cm}^3\mathrm{s}^{-1}$.

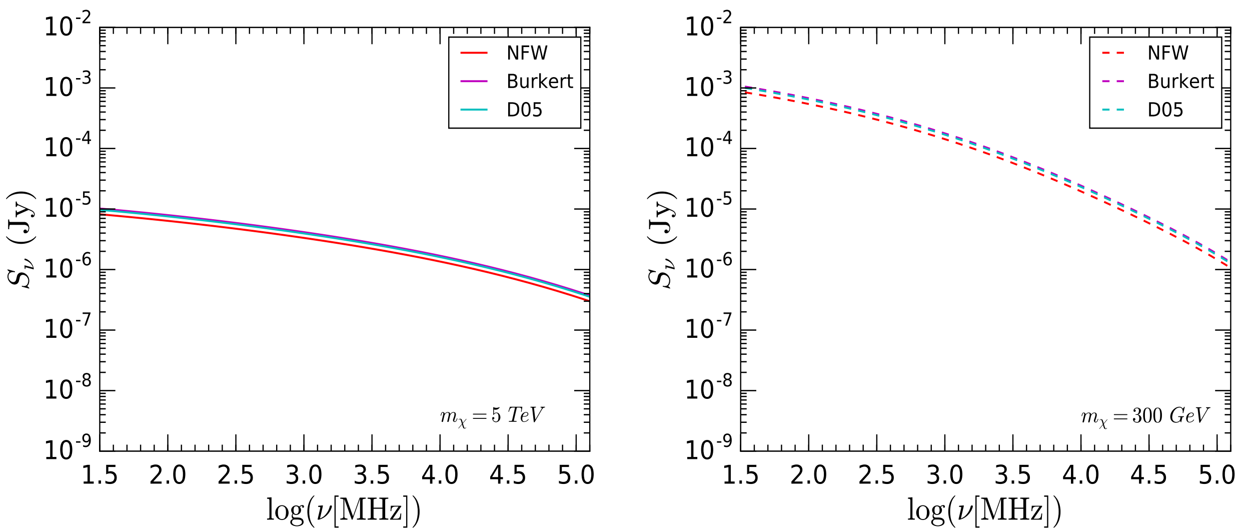

Figure 4.9: *Left panel:* Radio synchrotron flux $S_\nu(\nu)$ for Draco assuming three different DM profiles, NFW (red), Burkert (magenta) and D05 (cyan) [128]. DM mass is $m_\chi = 5$ TeV and annihilation channel is $b\bar{b}$ with annihilation rate $\langle \sigma v \rangle = 10^{-26}\mathrm{cm}^3\mathrm{s}^{-1}$. The values of diffusion coefficient and magnetic fields are $D_0 = 3 \times 10^{28}\mathrm{cm}^2\mathrm{s}^{-1}$ and $B = 1\ \mu G$, respectively. *Right panel:* Same as left panel, but for $m_\chi = 300$ GeV.

co-annihilation with particles spaced closely with it [113]. Once either of the above mechanisms is effective for the relevant particle spectrum, a trans-TeV DM particle remains consistent with all data including the relic density. This ensured, the pair-annihilation of a trans-TeV DM particle in dSph's enables the production of relatively energetic $e^{\pm}$ pairs which in turn reinforce the radio signals in the desired frequency range.

- $N_{pairs}(r)\left(=\frac{\rho_\chi^2(r)}{2m_\chi^2}\right)$: The numerator is supplied by observation. For higher m_χ, the denominator suppresses the number density of DM in the dSph. Thus this term tends to bring down the flux for higher DM masses.

- $\frac{dN_f^e(E)}{dE}B_f$: This has to have a compensatory effect for higher mass if the suppression caused by the previously mentioned term has to be overcome. Of course, the branching fractions B_f in different channels have a role. $\frac{dN^e}{dE}$ is often (though not always) higher for higher DM masses. This feature is universal at higher energies. This is basically responsible for a profusion of higher energy electrons produced via cascades, after annihilation in any channel has been taken place. More discussion will follow on this point later. It should be noted that $\frac{dN^e}{dE}$ represents the probability that an electron (positron) produced from the annihilation of *one pair* of DM. This gets multiplied by the available number density of DM. Thus, for comparable value of B_f in two benchmark scenarios, higher $\frac{dN^e}{dE}$ along with higher $\langle\sigma v\rangle$ in the dSph (when that is indeed the case), can cause enhancement of $Q_e(E,r)$ for higher m_χ.

Finally, the available electron energy distribution $\frac{dn}{dE}$ (which, convoluted with the synchrotron power spectrum, yields the radio flux (i.e. Eqs 2.3.4 and 2.3.6)), is obtained by solving Eq. 2.2.1 which has a generic solution (Eq. 2.2.4). Therefore, higher values of the source function ($Q_e(E,r)$) can produce higher radio flux at higher m_χ.

As mentioned above, the annihilation of heavier DM particles will produce more energetic $e^{\pm}$, as can be seen by comparing the upper-left and the upper-right panels of Figure 4.1 where we have shown $\frac{dN^e}{dE}$ in different channels ($b\bar{b}$, $\tau^+\tau^-$, W^+W^-, $t\bar{t}$). The lower panel shows the comparison of this $e^{\pm}$ spectrum for two DM masses (300 GeV and 5 TeV) arising from $b\bar{b}$ and $\tau^+\tau^-$ annihilation channels. Note that, the values of $\frac{dN^e}{dE}$ for $m_\chi = 300$ GeV and 5 TeV are differently ordered for the $\tau^+\tau^-$ and $b\bar{b}$ annihilation channels. The spectrum for $b\bar{b}$ channel is the steepest one, while $\tau^+\tau^-$ is the flattest. In fact, $\frac{dN^e}{dE}$ for the $b\bar{b}$ channel is governed mostly by charged pion ($\pi^{\pm}$) decay at various stages of cascade. For the $\tau^+\tau^-$ channel, on the other hand, there is a relative dominance of 'prompt' electrons. There remains a difference in the degree of degradation in the two cases. Such degradation is reflected more in the low-energy part of the spectrum, and leads to different energy distributions, which in turn is dependent on m_χ via the energy of the decaying b or τ. The reader is referred to see references [114, 115, 118] for more detailed explanations.

The presence of energetic $e^\pm$ in greater abundance, which is a consequence of higher m_χ, enhances the resulting radio signal obtained through Eqs. 2.2.4 and 2.3.4. As a result of this, the final radio flux S_ν (Eq. 2.3.6) gets positive contribution for higher DM masses compared to that for relatively lower masses for most of the annihilation channels (especially $b\bar{b}$, W^+W^-, and $t\bar{t}$). This can easily be seen if one compares the quantity $S_\nu \times 2m_\chi^2$ (i.e. removing the effect of the multiplicative factor $\frac{1}{m_\chi^2}$ present in the expression of N_{pairs}) for two DM masses, 300 GeV and 5 TeV, in the $b\bar{b}$ annihilation channel (left panel of Figure 4.10). If one chooses same annihilation rate (e.g. $\langle\sigma v\rangle = 10^{-26}\text{cm}^3\text{s}^{-1}$), the higher DM mass will give higher $S_\nu \times 2m_\chi^2$ (mainly in the high frequency region) for this channel. We have explicitly shown this for different choices of astrophysical parameters as indicated by different colors in the figure.

In scenarios where $\langle\sigma v\rangle$ corresponding to a particular m_χ is calculated from the dynamics of the model, it can happen that for some particular benchmark the annihilation rate ($\langle\sigma v\rangle$) is higher for larger m_χ (as mentioned earlier and will be discussed further in the next section). In those cases larger $\langle\sigma v\rangle$ can at least partially compensate the effect of $\frac{1}{m_\chi^2}$ suppression (coming from N_{pairs}) for higher m_χ. Thus one can get higher radio fluxes (S_ν) for larger DM masses compared to the smaller one.

For the $\tau^+\tau^-$ channel the situation is somewhat different. In this case, as we have already seen from the lower panel of Figure 4.1, there is a large degradation of the $e^\pm$ flux ($\frac{dN^e}{dE}$) in the low energy region for higher m_χ. This degradation in the source spectrum for higher m_χ will continue to present in the equilibrium distribution $\frac{dn}{dE}$. After folding this density distribution with power spectrum (see Eq. 2.3.4), the final frequency distribution will be suppressed for higher m_χ, mainly in the low frequency range. In the higher frequency range, the flux is still high for higher m_χ (similar to that in the other annihilation channel, e.g., $b\bar{b}$), because higher m_χ corresponds to higher electron distribution in the high energy range. All these phenomena are evident from the red curves (solid and dashed), shown in the right panel of Figure 4.10. Note that, these curves are for the choice of astrophysical parameters $D_0 = 3\times10^{28}\text{cm}^2\text{s}^{-1}$, $B = 1\ \mu G$. If one decreases the magnetic field B to 0.1 μG or increases the diffusion coefficient D_0 to $10^{30}\text{cm}^2\text{s}^{-1}$, the corresponding effect can be seen from the green and blue curves respectively.

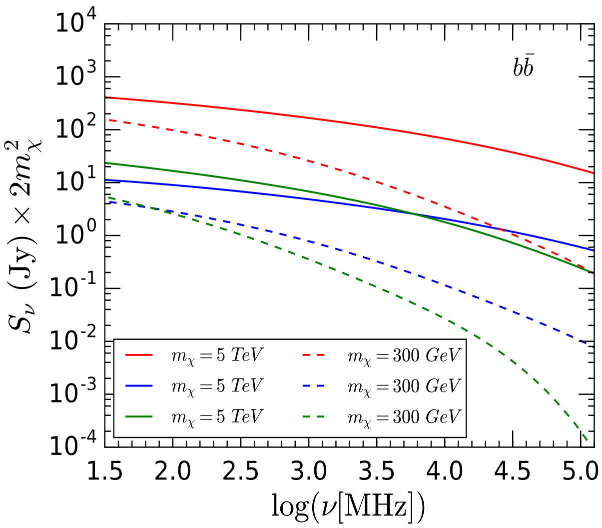

Figure 4.10: $S_\nu(\text{Jy}) \times 2m_\chi^2$ vs. frequency (ν) plot for two DM masses, 300 GeV (dashed lines) and 5 TeV (solid lines) in two different annihilation channels, $b\bar{b}$ (*left panel*) and $\tau^+\tau^-$ (*right panel*). Here three different sets of astrophysical parameters have been considered, $D_0 = 3 \times 10^{28}\text{cm}^2\text{s}^{-1}$, $B = 1\ \mu G$ (red); $D_0 = 10^{30}\text{cm}^2\text{s}^{-1}$, $B = 1\ \mu G$ (blue) and $D_0 = 3 \times 10^{28}\text{cm}^2\text{s}^{-1}$, $B = 0.1\ \mu G$ (green). Annihilation rate $\langle\sigma v\rangle = 10^{-26}\text{cm}^3\text{s}^{-1}$ for all cases.

To summarise, one can expect high radio flux for trans-TeV dark matter annihilation from a dSph, based on the following considerations:

- The high-mass DM candidate has to be consistent with the relic density, for which $\langle\sigma v\rangle$ at freeze-out is the relevant quantity.

- Such sizable $\langle\sigma v\rangle$ can still be inadequate in maintaining the observed relic density. Co-annihilation channels may need to be available in these cases, though such co-annihilation does not occur in a dSph. This in turn may necessitate a somewhat compressed trans-TeV spectrum.

- The high mass DM candidate should have appropriate annihilation channels which retain a higher population of $e^\pm$. This not only off sets the suppression due to large m_χ but also enhances, through the energy loss term $(b(E))$, the $e^\pm$ density at energies low enough to contribute to the radio signals observable at the SKA [143].

- Higher magnetic fields will be more effective in producing synchrotron radiation by compensating the suppression caused by a large galactic diffusion coefficient. As we have checked through explicit calculation, this happens even after accounting for electromagnetic energy loss of the $e^{\pm}$ through synchrotron effects.

4.5 Detectability Curves and Final Radio Flux

As mentioned earlier in Chapter 2, due to its large effective area and better baseline coverage, the SKA has a significantly higher surface brightness sensitivity compared to existing radio telescopes. Since the focus of this chapter is on the diffuse synchrotron signal from dSphs, we estimate the instrument sensitivity corresponding to the surface brightness and compare with the predicted signal. To calculate the sensitivity for a given source dSph, we need to know the baseline distribution of the telescope. The sensitivity can also be affected by the properties of the sky around the source, e.g., whether there exists any other bright source in the field of view.

Since the detailed design of the SKA is yet to be finalised, it is difficult to estimate the noise in the direction of a given source. For our purpose, however, it is sufficient to estimate the approximate values of the sensitivity using the presently accepted baseline design. In order to do so, we make use of the documents provided in the SKA website [143]. The calculations presented in the document allow us to compute the expected sensitivity near zenith in a direction well away from the Galactic plane for all the frequencies relevant to the SKA, i.e., for both SKA-MID and SKA-LOW. These include contribution from the antenna receiver, the spill-over and the sky background (consisting of the CMB, the galactic contribution and also the atmospheric contribution). Note that we have assumed that all other observational systematics, such as the presence of other point sources in the field, the effect of the primary beam, pointing direction-dependence of the sky temperature etc are already corrected for and hence are not included in the calculation of the thermal noise.

From the above calculation, we find that typical values of the SKA surface brightness sensitivity in the frequency range 50 MHz – 50 GHz for 100 hours of observation time is 10^{-6} – 10^{-7} Jy with a bandwidth of 300 MHz [143,148,174]. This may allow one to observe very low intensity radio signal coming from ultra-faint dSph's. While comparing the predicted signal with the telescope sensitivity, we have assumed that the SKA field of view is larger than the galaxy sizes considered here and hence all the flux from the galaxy will contribute to the detected signal. This assumption need not be true for the SKA precursors like the Murchison Widefield Array (MWA) where the effect of the primary beam needs to be accounted for while computing the expected signal [178].

Till date, people do not have clear understanding about either the DM particle physics model which governs the production of initial stage $e^{\pm}$ spectrum, or the astrophysical parameters like galactic diffusion coefficient (D_0), magnetic field (B) etc. which are responsible for the creation of the radio synchrotron flux. Thus in this analysis, we have constrained the regions in the DM parameter space that are responsible for producing detectable radio signals at the SKA, for particular choices of astrophysical parameters which are on the conservative side for a typical dSph like Draco [128]. On the other hand, assuming some simplified DM model scenarios with trans-TeV DM masses, we have estimated the limits on the $B - D_0$ plane, required for the radio signal from Draco to be observed at SKA.

Figure 4.11 shows the minimum $\langle\sigma v\rangle$ required for any m_χ in four different annihilation channels ($b\bar{b}$, $\tau^+\tau^-$, W^+W^-, $t\bar{t}$) for detection of DM annihilation induced radio signal from Draco with 100 hours of observation at SKA assuming a typical band width 300 MHz. The radio signal has been taken to be detectable when the observed flux in any frequency bin rises three times above the noise so as to ensure that the detection is statistically significant and is not affected by spurious noise features. We vary the DM mass over a wide range of 10 GeV to 50 TeV, assuming 100% branching fraction (B_f) in one annihilation channel at a time. The predictions here are for a conservative choice of the diffusion coefficient ($D_0 = 3 \times 10^{28}\text{cm}^2\text{s}^{-1}$) [128]. The bands are due to the variation of the galactic magnetic field B from 1 μG (lower part of the band) to a more conservative value 0.1 μG (upper part of the band). As expected, the minimum $\langle\sigma v\rangle$ required will be larger for lower magnetic fields as lower B reduces the the radio synchrotron frequency distribution (S_ν). These limits are the detection thresholds for SKA to observe radio signal from Draco. For $m_\chi \sim 1$ TeV this limit could be as low as $\langle\sigma v\rangle \sim 3 \times 10^{-29}\text{cm}^3\text{s}^{-1}$. For lower values of the diffusion coefficient such as $D_0 = 3\times10^{26}\text{cm}^2\text{s}^{-1}$ [116,117,137], the detectability threshold band comes down even further. Moreover, we have not considered any halo substructure contributions which are expected to enhance the radio flux [109] or lower the threshold limits even more. Along with these lower limits, we have also shown the model-independent upper limits (in 95% C.L.) on $\langle\sigma v\rangle$ in various channels from cosmic-ray (CR) antiproton observation (dashed curves) [83] and from 6 years of Fermi LAT (FL) γ-ray data (dotted curves) [70]. Note that the upper bounds from cosmic-ray antiproton observations are the strongest ones. For each annihilation channel, the area bounded by the upper and lower limits represents the region in the $\langle\sigma v\rangle - m_\chi$ plane which can be probed or constrained by SKA with 100 hours of observation. It is clear from the figure that even with conservative choices of astrophysical parameters, for $m_\chi \approx 50$ TeV there are significantly large regions of the parameter space which can be probed in the SKA. In such extreme cases, it is of course necessary to have a dark sector that allows high co-annihilation rates, so that the observed relic density bound is not excluded.

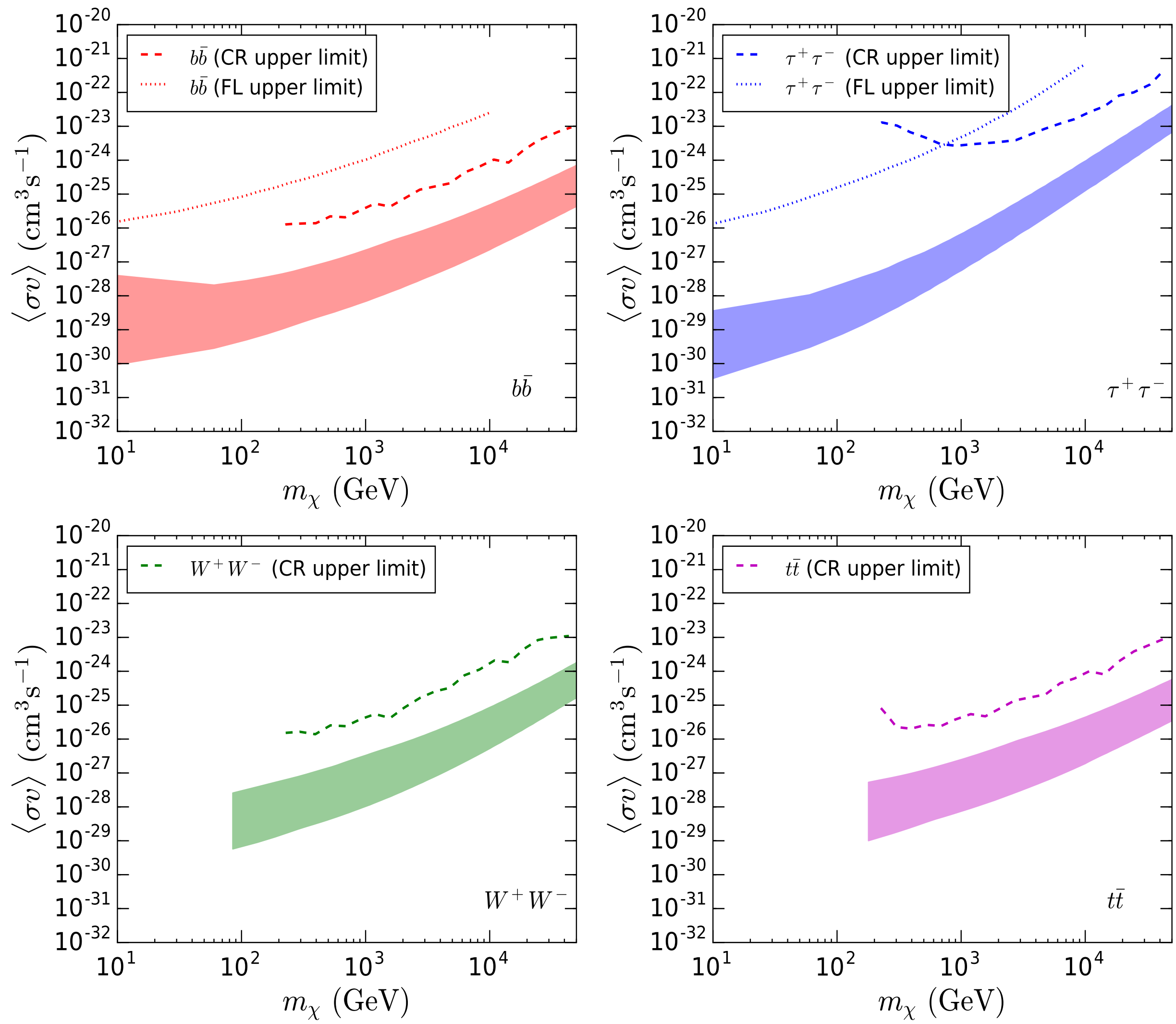

Figure 4.11: Lower limits (colored bands) in $\langle\sigma v\rangle - m_\chi$ plane to observe a radio signal from Draco dSph at SKA with 100 hours of observation for various DM annihilation channels ($b\bar{b}$ - *upper left*, $\tau^+\tau^-$ - *upper right*, W^+W^- - *lower left*, $t\bar{t}$ - *lower right*). For comparison, 95% C.L. upper limits from Cosmic-ray (CR) antiproton observation (dashed lines) [83] and 6 years of Fermi-LAT (FL) data (dotted lines) [70] have also been shown. The bands represent the variation of the magnetic field from $B = 1\ \mu G$ (lower part of the bands) to a more conservative value $B = 0.1\ \mu G$ (upper part of the bands). For all cases the value of the diffusion coefficient (D_0) is 3×10^{28}cm^{2}s^{-1}.

In the context of model-dependent analysis, three benchmark points, named as Model A1a, B2a and E [174], from Chapter 3, have been considered here. These benchmarks correspond to the minimal supersymmetric standard model (MSSM) scenario where the lightest neutralino (χ_1^0) is the DM candidate (χ). Table 4.1 contains the possible annihilation channels with branching fractions, DM masses ($m_{\chi_1^0}$) and annihilation rates ($\langle\sigma v\rangle$) calculated in those benchmark points. All these quantities have been calculated using publicly available package micrOMEGAs [120, 157]. Masses of neutralino and all other supersymmetric particles in these three cases are in the trans-TeV range. All of these benchmarks produce relic densities within the expected observational limits [23,163,164] and satisfy constraints coming from direct DM searches [49, 162], collider study [161], lightest neutral Higgs mass measurements [165] and other experiments [166, 167]. These benchmarks have been discussed in further detail in Chapter 3 ([174]). Figure 4.12 shows the detectability of these benchmarks for Draco dSph in SKA after 100 hours of observations. The predicted flux in each case falls within the area which is still allowed by the data and is at least 3 times above the observation threshold of SKA. The upper limits here are taken from cosmic-ray antiproton observation at 95% C.L [83] and the lower limits have been calculated for $D_0 = 3 \times 10^{28}\mathrm{cm^2s^{-1}}$ and $B = 1\ \mu G$. Along with these we have indicated the values of the total $\langle\sigma v\rangle$ (listed in third column of table 4.1) for different benchmarks by various black points. It should be noted that each of such benchmarks allows more than one annihilation channel. Consistently, the total cross-section in any of these cases is obtained by taking a sum over different channels. It is clear that all these high mass cases, which are allowed by cosmic-ray antiproton data, can easily be probed in SKA with 100 hours of observations. This is due to the following reason:

- $\langle\sigma v\rangle$ is more effective in offsetting $\frac{1}{m_\chi^2}$ suppression (present in the expression for number density of DM pair; Eq. 2.1.1) partially, though not fully.

- A greater abundance of high-energy $e^\pm$ is created by high m_χ. This, via electromagnetic energy loss driven by the term proportional to $b(E)$ in Eq. 2.2.1, generates a bigger flux of radio synchrotron emission, as evinced in the expression for $J_{Synch}(\nu, r)$ (Eq. 2.3.4).

- The cases where one predicts more intense radio flux for higher m_χ have DM annihilation mostly into the $b\bar{b}$ channel, as against the $\tau^+\tau^-$ channel. The corresponding cascade branching ratios as well as the three-body decay matrix elements and their energy integration limits are responsible for bigger radio flux.[4]

Model	annihilation channel (B_f)	$m_{\chi_1^0}$ (GeV)	$\langle\sigma v\rangle$ ($10^{-26}\mathrm{cm^3 s^{-1}}$)
A1a	$b\bar{b}(85\%)$, $\tau^+\tau^-(14\%)$	1000.6	0.27
B2a	$b\bar{b}(76\%)$, $\tau^+\tau^-(15\%)$, $W^+W^-(3\%)$, $t\bar{t}(3\%)$, $ZZ(2.8\%)$	3368.0	1.19
E	$b\bar{b}(79.1\%)$, $\tau^+\tau^-(18.3\%)$, $t\bar{t}(2.5\%)$	8498.0	9.12

Table 4.1: Lightest neutralino mass ($m_{\chi_1^0}$) and its pair annihilation rate ($\langle\sigma v\rangle$) inside a dSph along with branching fractions (B_f in percentage) in different annihilation channels for the selected MSSM benchmark points from [174] (shown in Chapter 3). Lightest neutralino is the DM candidate ($m_{\chi_1^0} = m_\chi$).

Figure 4.11 shows how the detectability threshold at the SKA varies with the galactic magnetic field B, for a fixed value of D_0. However, the values of these two parameters for the dSphs are quite uncertain. In view of this, it is also important to find out which regions in the astrophysical parameter space are within the scope of the SKA with 100 hours of observation, when both B and D_0 vary over substantial ranges. The detectability of the signal in the $B - D_0$ space is shown in Figure 4.13 for some illustrative DM scenarios. These correspond to DM masses of 1 (red curve) and 5 (blue curve) TeV. Cases where the dominant annihilation channel is $b\bar{b}$ are shown in the left panel, while the curves on the right panel capture the corresponding situations with $\tau^+\tau^-$ as the main channel. The solid line of each color corresponds to the maximum value of $\langle\sigma v\rangle$ for the chosen m_χ, consistent with the cosmic-ray upper limit. All points above and on the left of the curve correspond to the combinations of B and D_0 that make the radio signals detectable over 100 hours of observations with the SKA. Points for higher B in this region correspond to models that are detectable even with lower values of $\langle\sigma v\rangle$. Similarly, the detectable models having progressively lower $\langle\sigma v\rangle$ are arrived at, as one moves to lower D_0 for a fixed value of B. *It is evident from both the $b\bar{b}$ and $\tau^+\tau^-$ channels (chosen for illustrations in Figure 4.13) that consistent values of $\langle\sigma v\rangle$ can lead to detectability with 100 hours at SKA, for $B \gtrsim 5\times10^{-4}\,\mu G$ for $D_0 \sim 10^{27} cm^2 s^{-1}$. On the other hand, for larger values of $D_0 \sim 10^{30} cm^2 s^{-1}$, we need*

[4]Such effects can in principle be also expected if the $t\bar{t}, W^+W^-$ branching ratios dominate.

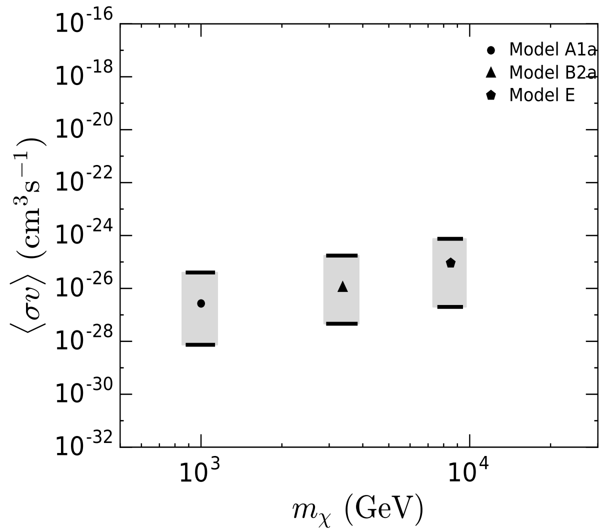

Figure 4.12: Location of various MSSM benchmark points (Model A1a, B2a, E; listed in table 4.1) in the $\langle\sigma v\rangle - m_\chi$ plane. The upper bars represent the 95% C.L. upper limits on $\langle\sigma v\rangle$ corresponding to these benchmark points from cosmic-ray (CR) antiproton observation [83]. The lower bars show the minimum $\langle\sigma v\rangle$ required for those benchmark points for the observation of radio flux from Draco dSph at SKA with 100 hrs of observations. The diffusion coefficient and the magnetic field have been assumed as, $D_0 = 3 \times 10^{28}\text{cm}^2\text{s}^{-1}$ and $B = 1$ μG respectively.

$B \gtrsim 10^{-2}$ μG for the signal to be detectable.

Finally, we show in Figure 4.14 the final radio fluxes in two of the MSSM benchmarks listed in table 4.1. For illustration we have taken the benchmark points A1a ($m_\chi \sim 1$ TeV) and E ($m_\chi \sim 8.5$ TeV). The annihilation is $b\bar{b}$-dominated for both cases. The yellow band here represents the SKA sensitivity [143], with a bandwidth of 300 MHz. The band is due to the variation of the observation time from 10 hours (upper part of the band) to 100 hours (lower part of the band) [143, 174]. The choice of the diffusion coefficient and the magnetic field is on the conservative side ($D_0 = 3 \times 10^{28}\text{cm}^2\text{s}^{-1}$ and $B = 1$ μG). We have already shown the detectability of these benchmarks in Figure 4.12. From this figure we can see that, even for 10 hours of observation, these high-m_χ benchmarks can easily be observed in SKA over most of its frequency range.

One important feature of Figure 4.14 is that, in a wide range of frequency (300 MHz – 50 GHz), suitable for the SKA, S_ν for the high mass case (Model E) is higher than that for the low mass case (Model A1a). Though the DM mass in Model E is larger, the annihilation

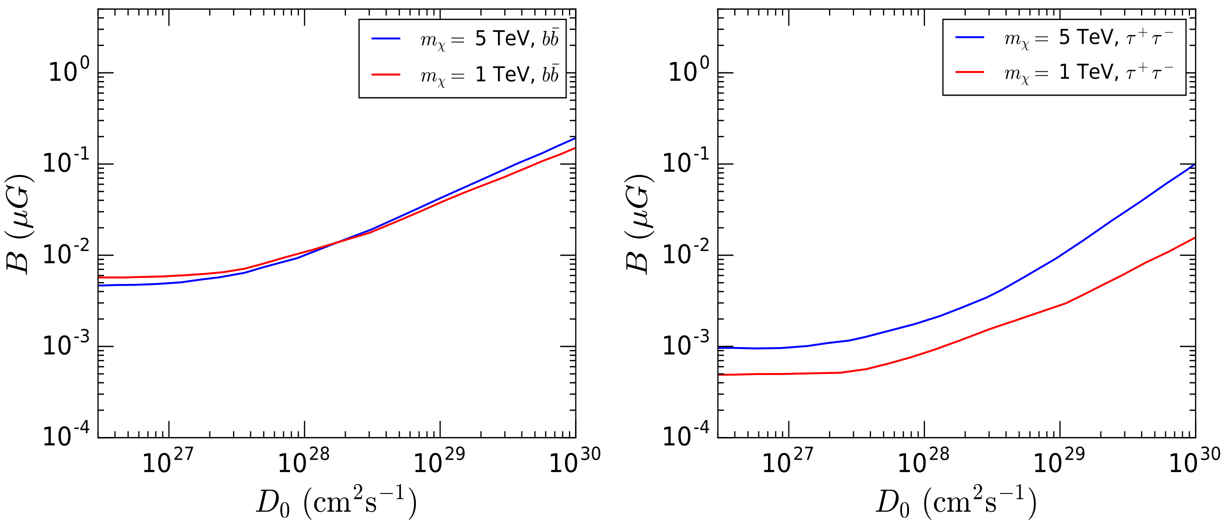

Figure 4.13: Limits in the $B - D_0$ plane to observe a radio signal from Draco dSph with 100 hours of observation at SKA for m_χ = 5 TeV (blue curves) and 1 TeV (red curves). Annihilation channels are $b\bar{b}$ (left panel) and $\tau^+\tau^-$ (right panel). The DM annihilation rate ($\langle\sigma v\rangle$) in each cases has been assumed to be the 95% C.L. upper limit as obtained from cosmic-ray antiproton observation [83].

rate in this case is higher ($\sim 9 \times 10^{-26}$cm^{3}s^{-1}) than that in Model A1a ($\sim 3 \times 10^{-27}$cm^{3}s^{-1}). In general, $\langle\sigma v\rangle$ should have a $\frac{1}{m_\chi^2}$ suppression, because of the energies of the colliding DM particles [27]. In spite of that, Model E (higher m_χ) has greater $\langle\sigma v\rangle$[5] than Model A1a (lower m_χ) mainly due to the closer proximity to a s-channel resonance mediated by CP-odd pseudoscalar in the annihilation process like $\chi_1^0\chi_1^0 \to b\bar{b}$. For detailed information reader is referred to see reference [174]

As discussed earlier, the higher value of $\langle\sigma v\rangle$ partially offsets the effect of larger DM mass and consequently we get $\frac{\langle\sigma v\rangle}{m_\chi^2}$ (which appears in the source function; Eq. 2.1.1) for Model A1a and Model E as 2.7 and 1.26 (in units of 10^{-33}GeV^{-2}cm^{3}s^{-1}), respectively, though the latter model has larger m_χ ($\sim$ 8.5 TeV) compared to the former ($\sim$ 1 TeV). Thus a 72-fold suppression due to m_χ^2 results in a suppression just by a factor of ≈ 2 at the level of $\frac{\langle\sigma v\rangle}{m_\chi^2}$. Also, note that the $b\bar{b}$ annihilation channel dominates for both models. These observations, together with the discussion in section 4.4 and the contents of Figure 4.10, explains a higher mass DM particle generating higher radio flux for scenarios where the $b\bar{b}$ annihilation channel

[5]higher value of $\langle\sigma v\rangle$ for higher m_χ is also needed to keep the relic density under the observed limit, even when there is scope of co-annihilation in the early universe.

dominates over $\tau^+\tau^-$.

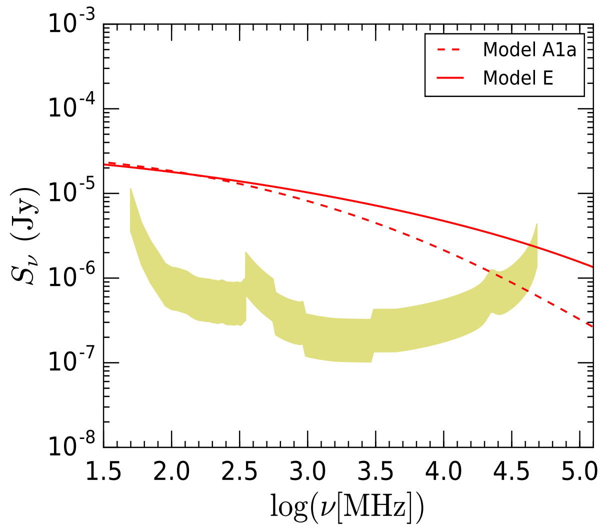

Figure 4.14: Radio synchrotron flux (S_ν) vs. frequency (ν) plot for Draco dSph using two MSSM benchmark points A1a and E from table 4.1. The yellow shaded band denotes the SKA sensitivity corresponding to the variation of observation time from 10 hours (upper part of the band) to 100 hours (lower part of the band) [143, 174]. Diffusion coefficient $D_0 = 3 \times 10^{28}\mathrm{cm}^2\mathrm{s}^{-1}$ and magnetic field $B = 1\ \mu G$.

4.6 Conclusions

The aim of this chapter has been establishing the broad applicability of the claim that pair-annihilation of trans-TeV WIMP DM in dSphs can be detectable in the upcoming SKA radio telescope. We have analysed not only the particle physics aspects of DM annihilation and subsequent cascades leading to $e^\pm$ pairs, but have also included the relevant astrophysical processes the electrons/positrons pass through before emitting radio waves, upon acceleration by the galactic magnetic field. We have set out to identify the mechanism whereby a trans-TeV DM candidate can thus be visible in radio search. We found that in the SKA frequency range, enhancement of the radio flux for this case is possible mainly due to the following reasons:

- Larger cross section or annihilation rate (required to maintain relic density under the observed limit for a trans-TeV DM) facilitated by the dynamics of the particle physics model. This helps in compensating the $\frac{1}{m_\chi^2}$ suppression due to large DM mass.

- Presence of energetic $e^\pm$ in the DM annihilation spectrum in greater abundance. This partially reduces the $\frac{1}{m_\chi^2}$ suppression effect and on the other hand enhances, through the energy loss term, the electron/positron density at low energies which helps to produce large radio flux.

- Dominance of the annihilation channel $b\bar{b}$ which yields a comparatively larger abundance of $e^\pm$ in all of the energy range of the spectrum produced by DM annihilation.

Simultaneously, effect of various astrophysical parameters (e.g. D_0, $b(E)$, B) on the radio synchrotron flux produced from the annihilation of a trans-TeV DM particle has been studied in detail.

Using SKA sensitivity we have drawn the limits in the $\langle\sigma v\rangle - m_\chi$ plane to observe radio flux from Draco with 100 hours of observation. We found that, these limits are much more stronger than the previously obtained bounds on $\langle\sigma v\rangle$ from Fermi-LAT γ-ray [70] or AMS-02 cosmic-ray antiproton observation [83]. Even for a conservative choice of astrophysical parameters ($D_0 = 3 \times 10^{28}\mathrm{cm}^2\mathrm{s}^{-1}$ and $B = 1\ \mu G$), we found that these limits can go as low as $\langle\sigma v\rangle \sim 3 \times 10^{-29}\mathrm{cm}^3\mathrm{s}^{-1}$ for a $m_\chi \sim 1$ TeV. This indicates towards a large region of WIMP parameter space which can be probed through the upcoming SKA. Along with these, we have also shown the limits in the $B - D_0$ plane. We found that, for a DM mass in the trans-TeV range, magnetic field as low as $B \sim 10^{-3}\ \mu G$ and diffusion coefficient as high as $D_0 \sim 10^{30}\mathrm{cm}^2\mathrm{s}^{-1}$ are well enough to produce radio flux above SKA sensitivity in 100 hours of observation time.

Taking the minimal supersymmetric standard model (MSSM) as an illustration, we have shown that benchmark points with lightest neutralino masses ($m_{\chi_1^0}$) in the range 1 - 8 TeV, which satisfy all the constraints from observed relic density, direct DM searches, collider searches and existing indirect searches like AMS-02, Fermi-LAT etc., can lead to detectable signals at the SKA with 100 hours observation, even with conservative choice of B and D_0. We have illustrated how the effects mentioned earlier can lead to a larger radio flux for a high mass DM benchmark point compared to a low mass case, thus establishing the credibility of the search for heavy DM through radio observation in SKA.

Chapter 5

Constraints on dark matter annihilation in dwarf spheroidal galaxies from low frequency radio observations

5.1 Introduction

We saw in Chapters 3 and 4 that the synchrotron radiation produced from self-annihilating dark matter (DM) candidate particles in dwarf spheroidal (dSph) galaxies (objects with high mass-to-light ratios indicating a high abundance of DM) can be a promising probe of DM models. In Chapter 3, we explore the use of the Square Kilometre Array (SKA) for the detection of synchrotron signatures from dSphs Draco, Segue I, and Ursa Major II [174]. It has been demonstrated there that the SKA could significantly exceed the reach of the Large Hadron Collider (LHC) in the search for self-annihilating DM candidate particles that produce charged particles and hence synchrotron emission due to an in-situ magnetic field. Such predicted synchrotron signals were discussed earlier by [148], but for masses within the LHC reach. In Chapter 4, we discuss in detail the mechanism involving various particle physics and astrophysical phenomena by which the radio flux generated from the pair-annihilation of heavy DM particles gets enhanced and thus can be detectable at the SKA. In the current chapter, we analyse the already available data obtained from the observations of 14 dSph galaxies by the Murchison Widefield Array (MWA) radio telescope [149] (a precursor to the upcoming telescope SKA) along with the Giant Metre-wave Radio Telescope (GMRT) [150], and derive constraints on the self-annihilating DM models.

5.2 Sample and data processing

Using Green Bank Telescope (GBT) observations at 1.4 GHz, [117] derive upper limits on radio synchrotron emission from Segue I and conclude that annihilation to e^+e^- is strongly disfavoured for DM particle masses < 50 GeV, but that other annihilation channels are not strongly constrained. [110, 111] used the Australia Telescope Compact Array to search for similar signals from nearby dSph galaxies accessible from the Southern Hemisphere.

These observations were conducted at trans-GHz frequencies, whereas the synchrotron signal is expected to be stronger at lower frequencies [174]. However, robust attempts to measure the DM annihilation synchrotron signal at low frequencies are currently lacking in the literature. The work described in this chapter addresses this deficiency for the first time, heralded by the emergence of modern low frequency facilities such as the MWA, a precursor for the even larger future SKA. The synchrotron signal expected to accompany DM annihilation is diffuse in nature, following the DM distribution. Therefore, high surface brightness radio observations are required. The observations with the GBT, a single dish, have excellent surface brightness sensitivity. The observations with the ATCA, as a relatively sparse interferometer, are not as sensitive to diffuse structures, but if the angular scales of interest are appropriate to the interferometer spacings, an interferometer can be effective.

The MWA ([149]) operates in the frequency range 80 - 300 MHz, with maximum baselines (during the period that describes this chapter) of 3 km, and with an array configuration that emphasises short baselines and high surface brightness sensitivity. The MWA shares many physical characteristics with the low frequency SKA, via scaling relations (for example ratio of station diameter to maximum baseline length), and is therefore an excellent instrument with which to make a first exploration of SKA science. In particular, given the predictions of [174], it is worth exploring DM annihilation scenarios at low frequencies with the MWA, as a precursor study to SKA investigations. An additional advantage of the MWA for DM studies of dSph galaxies is the survey efficiency, which has led to the ability to report here results for a large sample (relative to prior study sample sizes).

We analyse MWA radio synchrotron data for 14 dSph galaxies, for the first time at frequencies less than 1 GHz. The limits on such synchrotron emission are presented. We compare these limits to signals predicted from different DM annihilation channels, also considering the future potential of the MWA after recent upgrades.

No new observations or data processing were performed. Data were extracted from existing survey image databases for analysis, specifically the MWA GLEAM survey [141,181] and the TGSS ADR1 [150].

Our sample consists of the 14 dSph galaxies from Table 2 of [182] between declinations $+30°$ and $-55°$, being the northern and southern limits of the GLEAM and TGSS ADR1 surveys, respectively. The sample is listed in Table 5.1.

The Full width at half maximum (FWHM) of the MWA synthesised beam for the GLEAM survey varies across its 72 - 231 MHz frequency range and in the 170 - 231 MHz band used in this work is typically 2 - 3 arcmin. Thus, in order to separate point sources from the potential diffuse radio structures of interest, we utilise the TGSS ADR1 survey conducted with the GMRT, at a similar frequency to GLEAM but with an approximate 6 arcsec angular resolution.

For each of the galaxies in Table 5.1, we downloaded a $5° \times 5°$ image from the GLEAM image server[1] and a $1° \times 1°$ image from the TGSS ADR1 image server[2].

The GLEAM images were regridded to match the TGSS ADR1 images, using the MIRIAD [188] task regrid. The TGSS ADR1 images were then convolved with an appropriate Gaussian beam such that the final resolution matched the corresponding GLEAM image, using the MIRIAD task convol. A scaled version of the convolved TGSS ADR1 image was then subtracted from the regridded GLEAM image, to subtract the point sources detected with TGSS ADR1 from the GLEAM images, using the MIRIAD task maths.

Ideally, this process would produce a difference image that contains only the diffuse emission. In practise, a range of effects mean that some errors in the difference images are likely. For example, different ionospheric conditions and applied corrections for the GLEAM and TGSS ADR1 data will cause small mismatches in the positions of point sources, and therefore residual errors in the difference image. Assuming a single scaling (amounting to a single assumed spectral index) between the GLEAM and TGSS ADR1 images will lead to residual errors in the difference image, due to a range of spectral indices across the population of point sources.

However, we find that generally this process works very well, with very few examples of significant errors. We are most interested in the difference images in the vicinity of the

[1] http:mwa-web.icrar.orggleam_postageqform

[2] https:vo.astron.nltgssadrq_fitscutoutform

TARGET	RA (hms)	DEC (dms)	Dist. (kpc)	r_{half} (pc)	S_{RMS} (mJy/beam)	$S_{pred.}$ (mJy/beam)	Refs.
Sc1	01h00m09.35s	−33d42m32.5s	72	260	14	0.03	[183, 184]
LeoT	09h34m53.4s	17d03m05s	407	178	27	0.08(0.06)	[183, 185]
LeoIV	11h32m57s	−00d32m00s	160	116	32	0.006	[183, 185]
Com	12h26m59s	23d55m09s	44	77	63	0.1	[183, 185]
LeoI	10h08m27.4s	12d18m27s	198	246	32	0.04	[183, 184]
LeoII	11h13m29.2s	22d09m17s	207	151	35	0.04	[183, 184]
Car	06h41m36.7s	−50d57m58s	85	241	31	0.005	[183, 184]
For	02h39m59.3s	−34d26m57s	120	668	23	0.05	[183, 184]
Sex	10h13m02.9s	−01d36m53s	83	682	20	0.01	[183, 184]
Boo	14h00m06s	14d30m00s	66	242	47	0.15	[183, 185]
Herc	16h31m02s	02d12m47s	132	330	35	0.001	[183, 185]
LeoV	11h31m09.6s	02d13m12s	180	42	22	0.02	[183, 186]
Seg	10h07m04s	16d04m55s	23	29	30	0.04(0.03)	[183, 185]
Seg2	02h19m16s	20d10m31s	30	34	26	0.05	[183, 187]

Table 5.1: List of target galaxies

Column 1 - Target galaxy name; Column 2 - Right Ascension (hms) of galaxy centroid; Column 3 - Declination (dms) of galaxy centroid; Column 4 - Distance (kpc); Column 5 - Half light radius of galaxy (pc); Column 6 - Measured surface brightness RMS in difference image (mJy/beam); Column 7 - Peak value (in mJy/beam) of the predicted surface brightness (convolved with the Phase I MWA beam), arising due to dark matter annihilation.

target galaxies and in these regions we find no significant errors. In general, across the 14 galaxies, we find noise-like difference images that reflect the confusion-limited signals and diffuse emission expected from the MWA, once point sources are removed.

Figure 5.1 shows examples of the images and difference images, covering a range of dSph galaxy mass-to-light ratios. The RMS values measured in each of the 14 difference images are listed in Table 5.1. No excess diffuse emission was detected at the locations of the 14 galaxies.

For a sample of 14 objects, each being a non-detection, an obvious technique to explore is stacking, whereby the 14 difference images are averaged together to reduce the noise-like contributions. All of the difference images were regridded such that the galaxy centroid coordinates were centred on the middle pixel of a 512×512 pixel image, with 6 arcsec pixel sizes, using the MIRIAD task regrid. All 14 centroided difference images were averaged, using the MIRIAD task maths, obtaining an RMS of approximately 9 mJy/beam, with a beam area (defined by the FWHM of the elliptical Gaussian beam) of approximately 4 square arcmin, giving an RMS surface brightness of approximately 2 mJy/arcmin^2. No diffuse emission is detected above this level in the stacked image.

5.3 Modeling of synchrotron emission from dark matter annihilation

The energy distribution of the $e^{\pm}$ originating from DM annihilation in a dSph, which depends on DM mass m_χ, the velocity averaged annihilation rate $\langle \sigma v \rangle$ inside the galaxy, and the DM density profile $\rho_\chi(r)$, can be obtained for any annihilation channel by using Eq. 2.1.1 of Chapter 2. Following Eq. 2.2.1 there, these $e^{\pm}$ pairs then diffuse and lose energy through the interstellar medium of the galaxy up to large distances and attain a steady state depending on the diffusion parameter ($D(E) = D_0(E/1 \text{ GeV})^{0.3}$ ([128, 156])) and the energy loss coefficient ($b(E)$). These charged particles accelerate in the presence of the in-situ magnetic field (B) which leads to the synchrotron radiation [101, 108]. See Chapter 2 for detailed discussions. The surface brightness expected to be observed by the MWA telescope is obtained by convolving the theoretical signal with the synthesised beam of the telescope; see Appendix B.

The nature and properties of particle DM, if it exists, are yet unknown. In view of the consequent lack of knowledge in its annihilation rate in a dSph, the best one can do is to

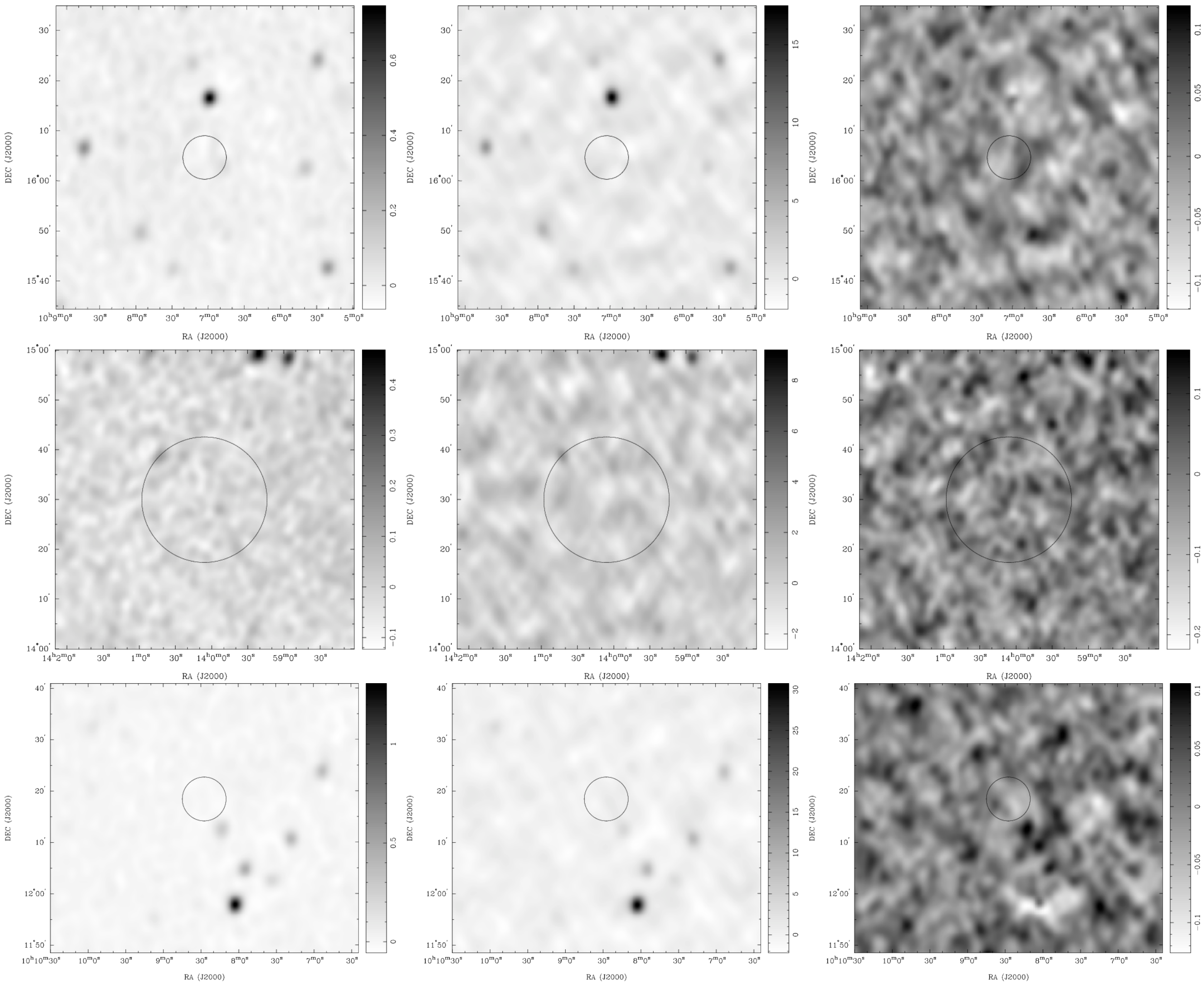

Figure 5.1: GLEAM images (left panels), TGSS ADR1 images convolved to GLEAM resolution (middle panels), the difference images (right panels), for three example target galaxies of varying mass to light ratios [182]: Segue1 (top: $M/L \sim 1400$); Bootes (middle: $M/L \sim 200$); and LeoI (bottom: $M/L \sim 7$). The intensity scales for the convolved TGSS ADR1 images are artificially high, as they are not normalised after convolution. However, the normalisation is absorbed into the scaling applied to match the GLEAM intensity scale.

use the available data to constrain the DM parameter space. Such constraints crucially depend on $\rho_\chi(r)$, B, and D_0. For the dark matter density, we use the NFW profile [125] with $\delta_{\rm dSph} = 1$ for Sc1, LeoT, LeoIV, LeoI, LeoII, Car, For, Sex, Herc, and Seg galaxies while for the remaining galaxies, we choose the Einasto profile [126] with $\alpha_{\rm dSph} = 0.4$ [123] [3]. For the latter class, well-constrained NFW parameters are mostly not available. In the former category, we have checked that NFW and Einasto best-fit parameters [4] lead to fluxes of the same order. The study neglects substructure effects within DM halos, predicted to be small in dSph galaxies ([116, 189]). The radius of the diffusion zone (typically twice the size of the luminous extent of a galaxy) has been set by scaling with respect to either Seg (for smaller galaxies like Com, LeoV, Seg, and Seg2 in Table 5.1) or Draco (for larger galaxies) using the guidelines discussed in [108, 117, 128, 156]. As mentioned earlier in section 2.2 of Chapter 2, it is extremely challenging to gain observational insights into the magnetic field properties of dSph galaxies. The lack of any strong observational lower limits suggests that the magnetic fields could be, in principle, extremely low. On the other hand, there may be numerous effects that can give rise to significant magnetic field strengths in dSph. Various theoretical arguments are proposed for values of $\sim \mu G$ levels. For detailed discussions readers are referred to [110, 135, 169]. Similarly, little is known about the value of the diffusion coefficient, D_0, for dSph galaxies; it could be as low as an order of magnitude smaller than that for the Milky Way [116, 117, 137]. Thus, in the absence of any direct knowledge of magnetic field and diffusion coefficient values for dSph galaxies, we take their values to be $B = 1 - 2\ \mu G$ [5] and $D_0 = 3 \times 10^{26} \mathrm{cm}^2\mathrm{s}^{-1}$. This leads to the largest possible values of flux that one could get from the current analysis. Stronger magnetic fields and lower values of D_0 are disfavoured by already existing observations [108, 116, 117, 135, 156]. DSph's which have larger D_0 and smaller magnetic fields (i.e. more conservative choices) would lead to much lower signals. As will be seen below, our benchmark astrophysical parameters help in probing the maximum allowed range of the DM parameter space which can be constrained by MWA observations.

[3] Functional forms of the above-mentioned NFW and Einasto profiles are provided in Chapter 2.

[4] These best-fit halo parameters are obtained from stellar kinematic data as described in [123].

[5] Note that, while Milky Way magnetic field $\sim 2\ \mu G$ can be realistic for nearby dwarf galaxies like Seg or Seg2, it might not be the case for other more distant dSphs where this value can be as low as a fraction of μG [135].

5.4 Results and discussions

Figure 5.2 represents a model-independent description of DM scenarios that can be compared to the MWA data presented here (from MWA Phase I observations), as well as those data expected from its next phase of operations (Phase II operations). Phase II of the MWA contains a new short-baseline array providing even higher surface brightness sensitivity at approximately 15 arcmin angular resolution [190]. The higher surface brightness of MWA Phase II allows the integration of lower surface brightness synchrotron emission to larger radii, meaning that the limits are improved on Phase I in proportion to the change in angular resolution. These Phase II limits have been derived integrating the modeled synchrotron emission over the realistic beam produced from an idealised Phase II observation. These limits are illustrative only, and observational limits would depend on the exact details of any given observation.

We present results for Boo in Figure 5.2, for which our predictions are most encouraging for detection among the 14 dSphs in Table 5.1. The figure shows the minimum $\langle \sigma v \rangle$ corresponding to any m_χ, which will produce radio synchrotron emission at the RMS thresholds from our Phase I observations, for magnetic fields (B) of 1 μG (left panel) and 2 μG (right panel). This is separately estimated for two channels of DM annihilation, namely, $b\bar{b}$ and $\tau^+\tau^-$. The corresponding plots for the W^+W^- and $t\bar{t}$ channels fall in between these two curves. It may be concluded that any candidate DM scenario yielding $\langle \sigma v \rangle$ above the curve for MWA Phase I is excluded by current data, for the choice of astrophysical parameters indicated in the caption. At the same time, the broken lines indicate the maximum values of $\langle \sigma v \rangle$ consistent with Fermi-LAT and cosmic ray data. Limits from the Phase II MWA exclude more of the parameter space.

We find that, for $B = 1 - 2$ μG, the predictions for minimum $\langle \sigma v \rangle$ are already above the upper limits, even for a non-conservative choice of diffusion coefficient, $D_0 = 3 \times 10^{26}\mathrm{cm}^2\mathrm{s}^{-1}$. Thus all particle DM scenarios which satisfy the (Fermi-Lat + CR) data are consistent with the Phase I MWA data. The minimum $\langle \sigma v \rangle$ lines with Phase II for 1 μG, on the other hand, are consistent with the CR/Fermi-Lat limits, for $m_\chi \lesssim 200$ GeV in the $b\bar{b}$ channel and $m_\chi \lesssim 1000$ GeV (or 1600 GeV for $B = 2$ μG) in the $\tau^+\tau^-$ channel. We also find that higher values of D_0, such as $3 \times 10^{28}\mathrm{cm}^2\mathrm{s}^{-1}$, which is a rather conservative choice for dSphs considered here [128], can not possibly constrain any DM scenario for both Phase I and Phase II, as shown in the two lower panels of Figure 5.2. [6]

[6] However, we have explicitly checked that (not shown in the current chapter) for higher magnetic field such as $B = 5$ μG, Phase II MWA data can constrain models up to at least $m_\chi \sim 500$ GeV in the $b\bar{b}$ channel

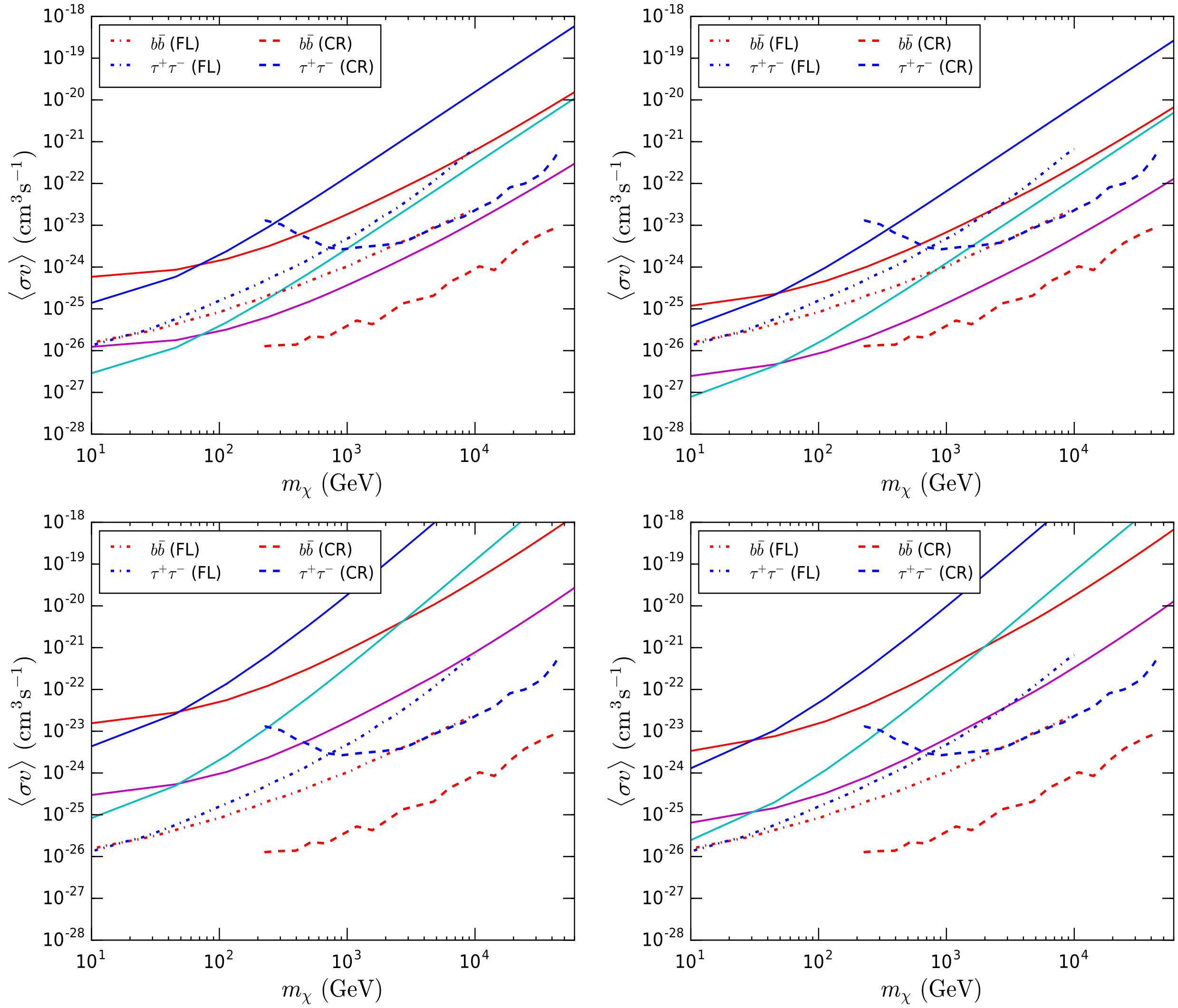

Figure 5.2: *Upper panel:* Lower limit (solid lines) in the $\langle \sigma v \rangle - m_\chi$ plane to observe a signal with the Phase I MWA from Boo galaxy for two different DM annihilation channels, $b\bar{b}$ (solid red) and $\tau^+\tau^-$ (solid blue). The values of the diffusion coefficient and magnetic fields are $D_0 = 3\times10^{26}$ cm^{2}s^{-1} and $B = 1\,\mu$G (left) and $B = 2\,\mu$G (right). The dashed and dash-dotted lines represent the 95% C.L. upper limits from cosmic-ray (CR) antiproton observation [83] and 6 years of Fermi-LAT (FL) gamma-ray data of 15 dSphs [70] respectively. The solid magenta ($b\bar{b}$) and solid cyan ($\tau^+\tau^-$) lines show the corresponding limits in Phase II MWA. *Lower panel:* Same as upper panel but with $D_0 = 3 \times 10^{28}$ cm^{2}s^{-1}.

Column 7 of Table 5.1 shows the predicted peak surface brightness for Phase I MWA due to DM annihilation for all 14 galaxies with minimal supersymmetric standard model (MSSM) benchmark B3 from [174] (shown in Chapter 3). For some galaxies (for which we have assumed NFW profile), corresponding predictions for Einasto are within brackets. These results are for the choice $D_0 = 3 \times 10^{26}\text{cm}^2\text{s}^{-1}$ and $B = 1\ \mu G$ and the numbers clearly show that the predictions due to this benchmark is always lower than the RMS values for all 14 galaxies.

5.5 Conclusions

Detectability at Phase I MWA, in the DM mass range 10 GeV - 50 TeV, requires annihilation cross sections that are already ruled out by gamma-ray and cosmic-ray antiproton observations. Phase II MWA can do significantly better and probe regions still allowed, especially if targeted to sources such as Boo. And ultimately the SKA will challenge a very wide range of DM annihilation models. On the whole, in addition to the exploitation of low-frequency flux, our study improves on existing knowledge in the following way: any positive signal in Phase II will point towards either magnetic field on the higher side ($> 2\ \mu G$) or a diffusion coefficient at the lower end ($\approx 3 \times 10^{26}\text{cm}^2\text{s}^{-1}$). An exception can be in the form of $\langle\sigma v\rangle$ higher than what is predicted in our benchmark [174] by about two orders of magnitude, which in turn contradicts the WIMP hypothesis itself.

---

and $m_\chi \sim 2500$ GeV in the $\tau^+\tau^-$ channel. Higher D_0 ($= 3 \times 10^{28}\text{cm}^2\text{s}^{-1}$) can bring down these explorable limits of m_χ to about 200 GeV or 50 GeV respectively. Note that $B = 5\ \mu G$ magnetic field is somewhat less realistic for the dSph galaxies considered here [135].

Chapter 6

Dark matter annihilation in ω Centauri: astrophysical implications derived from the MWA radio data

6.1 Introduction

In Chapter 5, we have reported the results of the first low radio frequency search for the synchrotron emission signal expected from the annihilation of dark matter (DM) particles [178]. Such radio signals arise from electrons and positrons, produced in DM annihilation cascades, undergoing cycloidal motion in the ambient magnetic field. We targeted 14 DM-rich dwarf spheroidal (dSph) galaxies using observations from the Murchison Widefield Array (MWA [149]) and the Giant Metre-wave Radio Telescope (GMRT [150]) to place limits on diffuse synchrotron emission from these galaxies for various models. While this represented a significant step toward much deeper observations by the future Square Kilometre Array (SKA) [148, 174, 191, 192], the results placed only limited constraints on DM models. Similar results have also been reported by a team using another low frequency interferometer, LOFAR, for the dSph galaxy Canes Venatici I [142]. One fundamental factor affecting our previous results and the LOFAR results is, of course, the large distances to dSph galaxies. In the present chapter, we deal with the MWA radio data on the Milky Way globular cluster Omega Centauri (ω Cen) which is almost ten times closer to us than any known dSph [124]. We interpret the observational input in terms of the DM annihilation inside ω Cen.

ω Cen is possibly a stripped dwarf spheroidal galaxy core captured by our Galaxy, in which the dark matter (DM) density may be high. Two groups have recently analysed the γ-ray data from Fermi-LAT for this object, to suggest best-fit values of the DM mass and annihilation rates in various dominant channels. We take advantage of the proximity of ω Cen and calculate the expected radio synchrotron surface brightness arising from DM annihilation in the ambient magnetic field, corresponding to each of the fits. In each case, Murchison Widefield Array (MWA) data constrain the magnetic field - diffusion coefficient plane for ω Cen. It is of particular significance that some knowledge of the magnetic field is used here to constrain the diffusion coefficient, which is difficult to estimate.

6.2 Observations of Omega Centauri (ω Cen)

A case has been recently made by Ref. [124] and Ref. [193] that ω Cen, historically classified as the largest globular cluster associated with our Galaxy, is the captured and stripped core of a dSph galaxy and has a significant DM component to its mass. These characteristics potentially make ω Cen a suitable object for studying DM annihilation models, since it is only 5.4 kpc from the Earth.

Ref. [124] and Ref. [193] analyze the Fermi-LAT data on γ-ray emission from the direction of ω Cen and claim consistency of the signal with DM annihilation. Ref. [124] claims the best fit to be $m_\chi = 31 \pm 4$ GeV and a velocity-averaged annihilation cross-section of $\log_{10}[\langle\sigma \mathrm{v}\rangle\ (\mathrm{cm}^3\mathrm{s}^{-1})] = -28.2\pm^{0.6}_{1.2}$, with $b\bar{b}$ as the principal annihilation channel. The fit by Ref. [193], on the other hand, favours $m_\chi = 9.1\pm^{0.69}_{0.62}$ GeV and $\log_{10}[\langle\sigma \mathrm{v}\rangle \mathrm{J}\ (\mathrm{GeV}^2\mathrm{cm}^{-2}\mathrm{s}^{-1})] = -5.5 \pm 0.03$ for the $q\bar{q}$ channel[1], or $m_\chi = 4.3\pm^{0.09}_{0.08}$ GeV and $\log_{10}[\langle\sigma \mathrm{v}\rangle \mathrm{J}\ (\mathrm{GeV}^2\mathrm{cm}^{-2}\mathrm{s}^{-1})] = -4.34 \pm 0.03$) for a $\mu^+\mu^-$ channel. The quantity J represents the astrophysical J-factor, a definition of which is given later in this chapter. These best-fit values assume that the γ-ray signal from ω Cen is arising solely due to DM annihilation. Since our emphasis is on the corresponding radio synchrotron signals, we have used this at face value.

No obvious populations of conventional high energy astrophysical objects are known to be associated with ω Cen to readily explain the γ-ray emission, although a more comprehensive examination of possible high energy photon sources is clearly required. For example, Ref. [194] find 30 objects in ω Cen with X-ray luminosities and colors consistent with a millisecond pulsar interpretation and suggest that these objects could be the source of the γ-ray emission seen with Fermi-LAT.

In order to predict synchrotron emission due to DM annihilation, the ambient magnetic

[1]The notation $q(\bar{q})$ denotes the first two generations of up and down type quarks(antiquarks) together.

field strength is an important parameter. The determination of magnetic field strength in dSph galaxies is not straightforward. However, measurements of the magnetic field in globular clusters are possible through the observation of pulsars, in particular via measurement of their dispersion measure and rotation measure. For example, Ref. [195] find evidence for magnetic fields possibly as high as 200 μG in the globular cluster 47 Tucanae. While a similar analysis is not currently possible for ω Cen (no pulsars are known in ω Cen), approximate estimates of its magnetic field strength are possible by virtue of its location within our Galaxy.

Using the best-fit DM annihilation models, suggested by Ref. [124] and Ref. [193] noted above (obtained by using the best-fit J-factor, as explained later in this chapter), the proximity of ω Cen, and the prospect of independently estimating the magnetic field strength within ω Cen (as outlined below), we re-visit the techniques used in the previous chapter to compute the corresponding radio synchrotron annihilation signals at low frequencies. The reader is referred to Ref. [178] for the details of our observational approach, a summary of the relevant literature, and our results for dSph galaxies. Finally, we compare our radio data with the theoretical expectations.

As has been mentioned above, our emphasis is on the correlation between gamma-ray and radio signals from a nearby globular cluster like Omega Centauri. The new step that we take in this study is the calculation of the radio flux for the same dark matter profile(s), based on which gamma-ray data have been interpreted, and its comparison with the MWA data. Thus [124] and [193] serve as our reference models for gamma-ray emission from dark matter annihilation in Omega Centauri. Going beyond them in a study like this would have taken us to territories where the aforementioned correlation would be impossible. Thus we found it sensible to confine ourselves to the modelling in [9] and [10]. We are thus able to relate the interpretation of gamma-ray data in each of these analyses to the corresponding radio data and their implication for the astrophysical parameters in Omega Centauri. While models differing from those in Ref. [124] and Ref. [193] can certainly be there, our approach can be used to predict and analyse the concomitantly altered radio synchrotron flux for each of them. Thus the adherence to particular models used in the recent literature enables us to lay out a general principle.

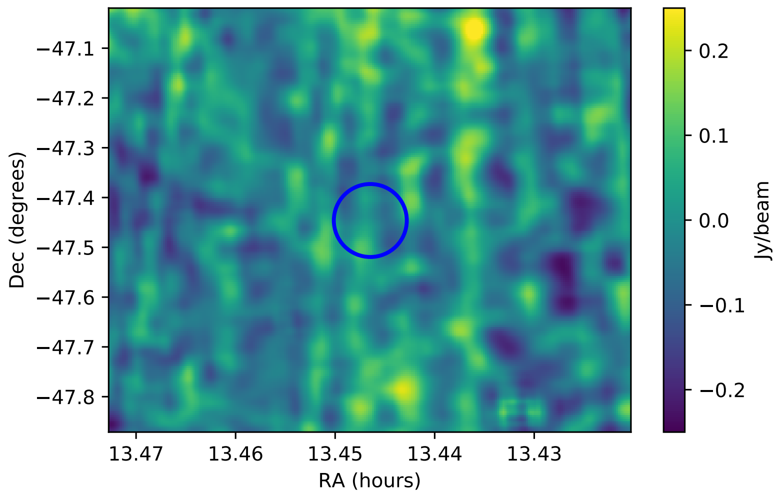

Figure 6.1: Difference image for ω Cen using MWA and TGSS ADR1 data. The blue circle denotes the optical half-light diameter for ω Cen.

6.3 Radio data analysis

Following Ref. [178], we produce an image for ω Cen that represents only extended, diffuse radio emission at 200 MHz, via the difference between an MWA image (sensitive to diffuse emission) and an image from the GMRT TGSS ADR1 (sensitive to compact emission). ω Cen is located close to the powerful radio galaxy Centaurus A (Cen A) and the MWA GLEAM data utilised in Ref. [178] cannot be utilised here, the reason being the difficulties of producing high quality images in the vicinity of extremely bright and complex objects such as Cen A. Thus, for ω Cen, we utilise MWA images that were produced specifically for Cen A, by [196]. We note that the GMRT data for ω Cen are not affected by Cen A in the same way that the MWA data are, due to the fact that the GMRT field of view is far smaller than the MWA field of view, meaning that the structure of Cen A that challenges MWA imaging is greatly attenuated by the primary beam response of the GMRT.

The difference image resulting from our analysis of the MWA data from Ref. [196] and the GMRT TGSS ADR1 data of [150] is shown in Figure 6.1.

While the images of the Cen A region by [196] are of a very high quality, imaging artefacts at a low level are still apparent in Figure 6.1. These artefacts are in the form of radial stripes that originate near the peak intensity regions of Cen A. At the location of ω Cen, these stripes appear largely in a north-south orientation. The RMS of the pixel values in Figure 6.1 is 72 mJy/beam, somewhat higher than the range of 14 - 63 mJy/beam achieved for 14 dSph galaxies by Ref. [178] (shown in Chapter 5). Thus, we make some effort to remove the artefacts and lower the RMS.

Two approaches for artefact removal were employed. First, we applied a positional warp to the pixels of the image which varied as a function of pixel location, then applied a cubic interpolation function over the pixel brightness distribution at their new locations, effectively straightening the stripes in a north-south direction. We averaged across the pixel columns to calculate an average stripe profile, and subtracted this from every pixel row. Finally, the pixels were warped back to their original locations, and the image re-interpolated. Thus, with this approach some regions of the image are lost.

The second approach calculates a generalized Hough transform of Figure 6.1 that assumes the linear stripes converge at a single right ascension and declination coordinate pair. The transform finds the mean value of pixels along radial lines emerging from the assumed convergence point, producing a function of (average) surface brightness as a function of angle. The stripes are then reconstructed by interpolating the angular function at the location of each pixel, and the reconstructed stripes are then subtracted from Figure 6.1.

Both residuals are shown in Figure 6.2, where an excellent correspondence between the two approaches is evident, each producing a residual RMS of 58 mJy/beam, representing a 25% improvement over the image in Figure 6.1 and bringing the ω Cen observational limits within the range achieved by Ref. [178]. At these limits, no evidence of diffuse synchrotron emission associated with ω Cen is evident.

6.4 Radio emission model calculation

The synchrotron surface brightness distribution generated via DM annihilation inside ω Cen is estimated for any annihilation channel (like $b\bar{b}$, $\mu^+\mu^-$, $q\bar{q}$ etc.), following the same mechanism described earlier in Chapter 2. The annihilation rate of DM particles, having a mass m_χ, is determined by the velocity-averaged quantity $\langle\sigma v\rangle$. Like in the case of dSphs, the radio synchrotron flux produced inside ω Cen depends on the energy loss parameter $b(E)$ as well as on the diffusion term $D(E)$. The diffusion term can be parameterised as $D(E) = D_0 \, (\frac{E}{\mathrm{GeV}})^{0.3}$, where D_0 is the diffusion coefficient [108,128,174,191,197]. The size of the diffusion zone for ω Cen is assumed to be ~ 0.4 kpc, obtained by scaling with respect to the Segue I dSph [108,117]. Using the procedure shown in Appendix B, the surface brightness distribution, arising due to DM annihilation, is convolved with the Phase I MWA beam and the peak value is compared with the observation [136,178]. As mentioned in Chapter 5, the

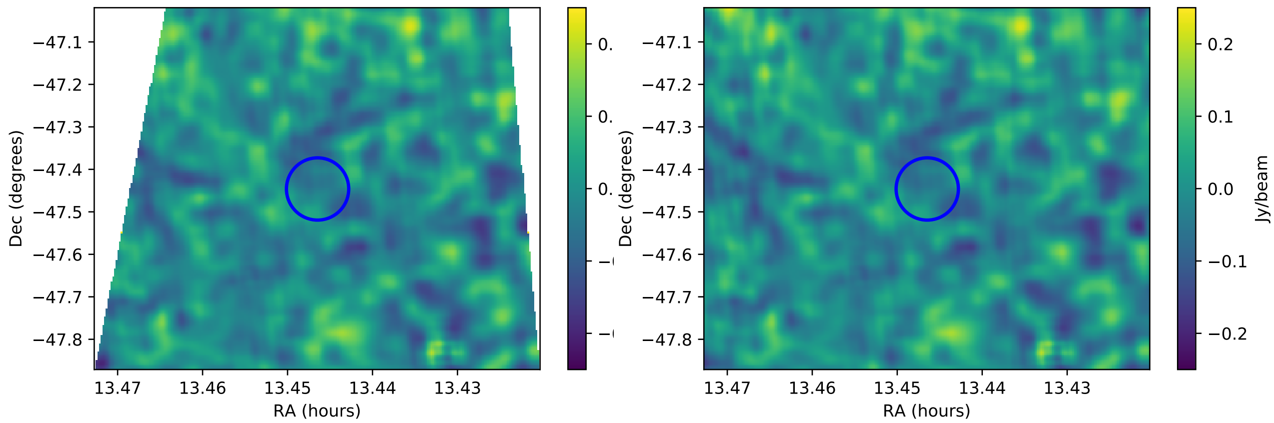

Figure 6.2: Difference images for ω Cen following estimation and removal of artefacts. The left panel shows the warp, average, and de-warp approach described in the text. The right panel shows the residuals for the Hough transform approach described in the text. The blue circles again denote the optical half-light diameter for ω Cen.

Full width at half maximum (FWHM) of the Phase I MWA beam is about 2 - 3 arcmin for the frequency range considered here.

One of the primary ingredients in our calculation is the DM halo profile ($\rho_\chi(r)$) for ω Cen (see Eq. 2.1.1). In this analysis, we have assumed the canonical NFW profile [125] to describe the DM distribution associated with ω Cen. The analytic form of this NFW profile, involving the parameters r_s (halo scale radius) and ρ_s (halo scale density), is shown in Chapter 2. The astrophysical J-factor, which determines the number of DM pairs available to annihilate inside ω Cen, is defined as the line-of-sight (los) integration of $\rho_\chi^2(r)$,

$$\mathrm{J} = \int_{\Delta\Omega} d\Omega \int_{\mathrm{los}} \rho_\chi^2(r(l,\Omega))dl, \tag{6.4.1}$$

where $\Delta\Omega$ is the angular size for the DM distribution in ω Cen [124]. Using stellar kinematics data for ω Cen, Ref. [124] has obtained r_s and the J-factor within 68% confidence limits.

The implications of the claims made by Ref. [124] and Ref. [193] for MWA data can be best assessed if one uses the same J-factor to study both. We thus use the best-fit J-factor (assuming a NFW profile) obtained from stellar kinematics in Ref. [124], via a method independent of radio or γ-ray data. This value is used also in the case of Ref. [193], where the best-fit value of $\langle\sigma v\rangle$J is listed. The best-fit value of $\langle\sigma v\rangle$ is thus extracted, assuming a diagonal correlation matrix. The corresponding value is already extracted in the analysis of

Ref. [124]. These quantities, together with the DM mass m_χ and the dominant annihilation channel, comprise the model inputs.

In our calculations for the expected synchrotron signal from DM annihilation, we have used three different sets of r_s and ρ_s which are denoted as $[r_{s_0},\rho_{s_0}]$, $[r_{s_{max}},\rho_{s_{min}}]$, and $[r_{s_{min}},\rho_{s_{max}}]$. Here, r_{s_0}, $r_{s_{max}}$, and $r_{s_{min}}$ are the best-fit and 68% maximum and minimum values of r_s from Ref. [124], respectively [2]. They produce the same best-fit J-factor found in the analysis of Ref. [124]. One can verify numerically that to a close approximation the J-factor scales as $\rho_s^2 r_s^3$. At the same time, the Green's function, relevant to the calculation of the peak radio surface brightness, scales in the same manner. Thus, once one adopts the best-fit value of the J-factor, and changes r_s with ρ_s altered concomitantly to keep J the same, one should obtain the same peak surface brightness, as can be seen in Table 6.1, using illustrative values of the diffusion coefficient D_0 and the magnetic field B. The results presented henceforth use the best-fit values of the NFW parameters, but are valid over the 68% confidence interval.

6.5 Magnetic field estimate for ω Cen

As noted earlier, an important element in modeling the synchrotron emission due to DM annihilation is the ambient magnetic field strength. In the case of the DM annihilation in dSph galaxies (as discussed in the previous chapters), producing estimates of the magnetic field strength was difficult. In the current chapter, because ω Cen belongs to our Galaxy, we can use the best available models of the Galactic magnetic field to make independent estimates, thereby constraining our DM annihilation models.

We estimate the interstellar magnetic field at the location of ω Cen using two leading Galactic magnetic field models: the model by Jansson and Farrar [198,199] (hereafter JF12) and the model by Jaffe *et al.* [200] (hereafter J13). These are two of the most advanced models of the magnetic field in the Milky Way. They both consist of a regular magnetic field component, an isotropic turbulent component, and an anisotropic turbulent component which has a random direction but a fixed orientation along the regular magnetic field. The two models are in many ways similar, but each have their strengths and weaknesses.

The regular magnetic field is assumed to have a spiral shape in both models, with slightly different parameterizations. The magnetic field runs along the spiral arm and its strength is allowed to vary between segments. The two approaches make partially different choices

[2] $\{r_{s_0}, r_{s_{max}}, r_{s_{min}}\} = \{1.63, 4.63, 0.11\}$ (in pc);
$\{\rho_{s_0}, \rho_{s_{min}}, \rho_{s_{max}}\} = \{2.87 \times 10^5, 6.03 \times 10^4, 1.64 \times 10^7\}$ (in GeVcm^{-3}).

D_0 ($\mathrm{cm^2 s^{-1}}$)	B (μG)	channel	I (mJy/beam) with $[r_{s_0},\rho_{s_0}]$	I (mJy/beam) with $[r_{s_{max}},\rho_{s_{min}}]$	I (mJy/beam) with $[r_{s_{min}},\rho_{s_{max}}]$
3×10^{26}	5	$b\bar{b}$	15.1	14.9	15.2
		$q\bar{q}$	9.8	9.7	9.7
		$\mu^+\mu^-$	1962.4	1922.3	1979.6
3×10^{27}	10	$b\bar{b}$	4.6	4.6	4.7
		$q\bar{q}$	3.9	3.9	4.0
		$\mu^+\mu^-$	480.4	475.1	482.6

Table 6.1: Columns 1 and 2: Some illustrative values of diffusion coefficient (D_0) and magnetic field (B) in ω Cen; Column 3: Different best-fit annihilation channels from [124] ($b\bar{b}$) and [193] ($q\bar{q}$ and $\mu^+\mu^-$); Columns 4 - 6: Predicted peak synchrotron surface brightnesses (I (mJy/beam)), convolved with the MWA beam, corresponding to those values of D_0 and B (mentioned in columns 1 and 2) for different choices of $[r_s,\rho_s]$ which produce the same best-fit J-factor for ω Cen as quoted in [124]. The DM mass (m_χ) and annihilation rate ($\langle\sigma v\rangle$) in each case have been fixed at the values obtained from Ref. [124] and Ref. [193].

of data to fit the models to, resulting in different uncertainties (see Ref. [201] for a detailed discussion). JF12 includes also an out-of-plane component of the regular magnetic field, which is ubiquitously observed in edge-on nearby spiral galaxies as the so-called X-shaped field. J13 does not have an out-of-plane component, but fits also to dust polarization, allowing differentiation between locations of the synchrotron arms and the dust arms. For both models, we use the updated best-fit parameter values which match the Planck synchrotron data [201].

For both models, we use the Hammurabi software package [202] to calculate the Galactic magnetic field at the location of ω Cen (assumed to be at $(\ell, b) = (309°, 15°)$ and at a distance of 5 kpc). We use the best-fit parameters of these models to calculate the regular magnetic

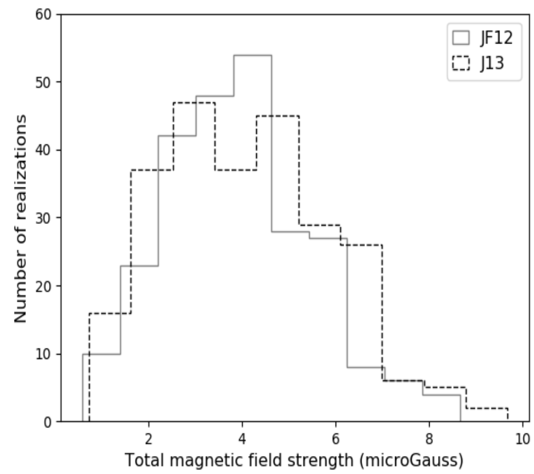

Figure 6.3: Histograms of the total magnetic field strength at the location of ω Cen, in 250 realizations of the random field component, for the Galactic magnetic field models of JF12 and J13

field component, which is consistent between the two models at a value of $B_{reg} \approx 1$ μ G at this location. For both models, we ran 250 realizations of the random magnetic field component to gauge the range of possible magnetic field values at the location of ω Cen. These distributions are shown in Figure 6.3.

We adopt magnetic fields between 1 and 10 μG as a plausible range over which to calculate our DM annihilation models.

6.6 Results

Figure 6.4 shows the constraints on the $B - D_0$ plane for ω Cen, obtained from our MWA data. The shaded areas correspond to cases where the predicted peak surface brightness is higher than 58 mJy/beam, the observational limit. As estimated earlier, the upper limit on the magnetic field (B) at ω Cen is taken to be 10 μG and the lower limit is taken to be 1 μG (shown by the horizontal dashed lines). The $\mu^{\pm}$ annihilation scenario of [193] is tightly constrained, which is relaxed for the $q\bar{q}$ channel. The $b\bar{b}$ channel suggested in [124] falls in between, having a slightly larger exclusion region than in the second case above.

Figure 6.4 is instructive since it places limits on relatively low values of D_0 in ω Cen, whose vicinity to the Milky Way would make such values otherwise plausible, in contrast

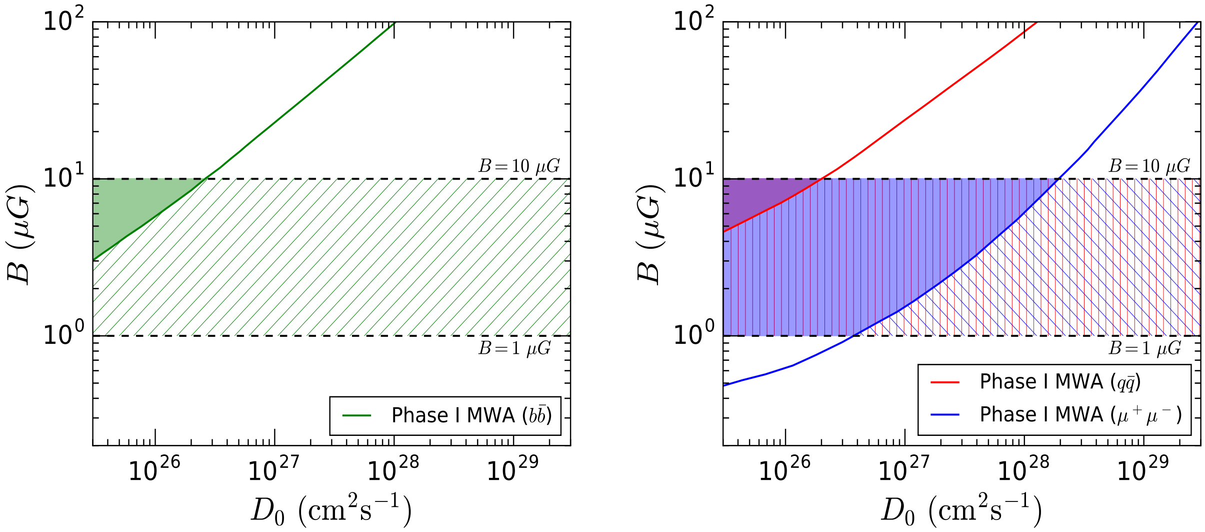

Figure 6.4: Areas in the $B - D_0$ plane (denoted by shaded colors) which are ruled out by the Phase I MWA data on ω Cen. *Left panel:* Corresponds to the findings of [124] where the DM annihilates dominantly into $b\bar{b}$. *Right panel:* Shows the corresponding regions, based on [193], for DM annihilation into $q\bar{q}$ (red) and $\mu^+\mu^-$ (blue). The range of B is taken as 1 - 10 μG (see the foregoing analysis). In each case, the hatched area between 1 - 10 μG indicates the region which is still allowed by the MWA I data.

to dSph galaxies [116, 135]. We can also use it to explore the effect of deeper observational limits on the synchrotron emission. For example, if a limit ten times deeper (5 mJy/beam) could be achieved, values of $D_0 \simeq 10$ times larger could be ruled out for $B = 10\mu G$. We note that our early processing of data using the upgraded MWA [190] at the position of ω Cen indicates that improvements of this order appear likely, which will be explored in a future publication. A limit 100 times deeper (0.5 mJy/beam) would strengthen the limit correspondingly, bringing the models into serious conflict with observations. In this case, such improvements will only likely be made using the future capabilities of the SKA. Improved knowledge of the magnetic field would assist us even further in this respect.

Using the best-fit values of m_χ and $\langle\sigma v\rangle$ we can briefly revisit the analysis of the Boo dSph galaxy from our previous work [178]. Note that, among the 14 dSph studied previously, we obtained largest predicted radio signal for Boo. In the current chapter, with the best-fit DM annihilation model corresponding to the γ-ray observation, we find that the predicted synchrotron signal for Boo still lies below the threshold for detection with the MWA we reported. The parameters that produce a prediction closest to our observational limits are

($B \gtrsim 10\mu G, D_0 \lesssim 10^{26}\mathrm{cm}^2\mathrm{s}^{-1}$), for the model corresponding to annihilation into $\mu^+\mu^-$.

6.7 Conclusions

We conclude that, following the studies in [124] and [193], objects such as ω Cen are likely to provide some of the best environments in which to test DM annihilation models with γ-ray and radio synchrotron observations in tandem, plus studies of magnetic field strength. ω Cen produces a much stronger predicted synchrotron signal than typical dSph galaxies, for the same annihilation models, and the prospects for understanding the magnetic field strength in galactic objects such as ω Cen is better. We therefore derive significant limits on model parameters from current MWA data. Also, observations deeper than those used here can subject DM annihilation models to serious tests.

The results presented here provide one avenue among a rich and growing set of investigations into the presence and nature of DM, now including multi-wavelength and multi-messenger approaches [203]. In general, a diverse set of empirical approaches is required, as DM properties are unclear and a wide span of theoretical model parameter space confronts observations. As such, exploratory studies of electromagnetic and non-electromagnetic signatures of DM processes are required to match this theoretical uncertainty.

Chapter 7

Constraints on MeV dark matter and primordial black holes: Inverse Compton signals at the SKA

7.1 Introduction

All of our previous analyses, presented in Chapters 3 - 6, were mainly focused on the study of radio signals resulting due to the annihilation of relatively heavy dark matter (DM) particles, i.e., DM mass m_χ ranges from few GeV to tens of TeV. However, it may be equally worthwhile to look for possible signals that arise from weakly interacting, stable (on a cosmological time scale), MeV range beyond standard model (BSM) particles, depending on the fact that such particles are often proposed as viable candidates for DM [30, 33, 80, 204, 205]. Since no compelling evidence of usual weakly interacting massive particles (WIMP), having masses in the GeV (or TeV) scale, has been found yet in any terrestrial DM search [49, 60, 162] or indirect search experiment [71, 197, 206], studies of sub-GeV DM particles have been objects of recent interest [207].

The study of annihilating DM signals, described in the preceding chapters, assumes that the DM particles are fully stable. However, this may not be always an ultimate scenario. As mentioned earlier in Chapter 1, the DM content of the universe can be explained by the population of a weakly interacting particle which decays into pairs of lighter Standard Model (SM) particles. If such a decaying particle exists, then its lifetime must be larger than the age of the universe. The precise limits on the DM lifetime depend on its mass, dominant decay modes and the internal degrees of freedom. For the kind of MeV DM particles considered here, stringent constraints on the lifetime can be obtained from the experiments like Planck [208].

On a separate note, primordial black holes (PBHs) [37, 38] are also used to explain the observed DM abundance of our universe. This idea has been explored through past several decades in the context of various cosmological and astrophysical observations [39, 40]. In order to ensure that the lifetime of PBHs exceeds the age of the universe, so that they can describe the DM abundance of today's universe, their masses must be larger than $\sim 10^{15}$ g [40]; for updated constraints see refs. [209–212].

Inside a DM halo, surrounding a galaxy or a galaxy cluster, the annihilation of MeV DM particles produces low energy $e^{\pm}$. They may also originate in the decay of MeV DM particles (provided the fact that the decay lifetime is large compared to the age of the universe) as well as in the Hawking radiation from PBHs in the range 10^{15}–10^{17} g [40]. All these cases are in contrary to what have been shown in Chapters 3 and 4, where the heavy DM particles, upon annihilating, generate ultra-relativistic $e^{\pm}$ pairs. Observing signals from the low energy $e^{\pm}$ in indirect detection experiments is a major challenge. The existing constraints from COMPTEL [213] and INTEGRAL [214] exploit the photons produced from $e^{\pm}$. The Planck data on the cosmic microwave background (CMB) also provide stringent constraints on DM particle masses as low as ~ 1 MeV (in case of e^+e^- final state) [93, 208] and for PBH masses in the range 10^{15} to 10^{17} g [209].

In this chapter, we describe the prospects for constraining the annihilation and decay rates of MeV DM particles as well as the abundance of PBHs in the search for photon signals generated through Inverse Compton (IC) scattering. The low energy $e^{\pm}$, emitted in the annihilation/decay of MeV DM particles or in the Hawking radiation from PBHs, produce those signals when scattering off the ambient photon bath. While interactions with energetic CMB photons and other more energetic components of the bath such as infrared (IR) and starlight (SL) lead to X-ray and soft γ-ray emissions [215, 216], scattering on the low-energy part of the CMB photon distribution can give rise to comparatively low frequency signals. Our aim is to study the possibility of detecting such low frequency signals with the help of the upcoming radio telescope Square kilometer Array (SKA), which has been studied previously in Chapters 3 and 4 in the context of DM searches [148, 174, 191, 217–219].

To this point, galactic and extragalactic synchrotron fluxes have been studied using current and upcoming radio telescopes, which appear to be more effective in the case of annihilation or decay of heavier DM particles [110, 136, 148, 173, 174, 178, 191, 219]. However, this method starts losing sensitivity (even for electron-positron dominated annihilations or decays) if masses of DM particles become $\lesssim$ a GeV. This is also true in the case of Hawking radiation [220] (equivalent to the DM decay [210]) from PBHs with masses heavier than 10^{15} g.

We consider 100 hours of SKA observation of two local dwarf spheroidal (dSph) galaxies, namely, Segue I [117] and Ursa Major II [116], the globular cluster ω-cen [124, 193] and the Coma cluster [101] to determine the viable regions in the parameter spaces of MeV DM and PBH. We compare our constraints with the existing constraints obtained from Planck [93, 208, 209], COMPTEL [81], INTEGRAL [81, 82, 215], and Voyager 1 [92, 221]. We exhibit how the radio survey of nearby dwarf galaxies through the SKA telescope can be translated into the limits on the diffusion of sub-GeV electrons inside those targets. Finally, we discuss the scope of the future observations of e-ASTROGAM [222] in the context of MeV DM and PBH parameter spaces.

The chapter is organized as follows. In section 7.2, we discuss IC fluxes from MeV DM and PBHs. In section 7.3, we discuss the source functions for DM and PBHs; the associated IC flux calculation is shown in 7.4. In section 7.5, we present our results, and we conclude in section 7.6.

7.2 IC Fluxes from MeV DM and PBHs: radio signals for the SKA

Studies of the particle nature of DM using SKA are based on its annihilation and decay properties [148, 219]. These annihilations or decays inside a dSph or galaxy cluster produce charged particles like electrons/positrons or neutral particles like photons. As mentioned above, these particles may also arise due to the Hawking radiation of PBHs, if it is assumed that a fraction of the DM abundance is made of them. The $e^{\pm}$, upon interacting electromagnetically in the dSph or cluster medium, give rise to various types of photon fluxes such as Inverse Compton (IC), synchrotron etc [101, 108]. Depending on the value of the DM particle mass m_χ or PBH mass $M_{\rm PBH}$, peaks of these flux distributions may shift towards the higher or lower frequency side.

As we saw in the earlier chapters, the synchrotron flux, produced from GeV (or TeV) DM particles in any dSph or galaxy cluster, appears as a radio signal. Some previous works have studied this effect to constrain the GeV (or TeV) scale DM particles in the context of the upcoming radio observation at the SKA [148, 174, 191, 217, 219]; we have discussed some of these in Chapters 3 and 4. Nevertheless, it is difficult to detect the synchrotron flux in any radio telescope including the SKA if the DM particle mass reaches the MeV range. In this case, since the annihilation or decay spectra are lack of energetic $e^{\pm}$ which can interact with the magnetic field (B) present inside typical dSphs or galaxy clusters, the corresponding synchrotron emission is very weak in frequency. Thus, constraining MeV DM particles, using the synchrotron radiation as a signal for the radio telescopes, is difficult. This should also be true for PBHs which exist today and are able to emit $e^{\pm}$, i.e., with mass $M_{\rm PBH}$ in the range $10^{15}{\rm g} \lesssim M_{\rm PBH} \lesssim 10^{17}{\rm g}$ [40].

On the other hand, the photon flux generated in the IC scattering of electrons/positrons on CMB photons present inside a galaxy or galaxy cluster, is comparatively higher in frequency than the usual radio waves when one is looking for a m_χ in the GeV or TeV scale [101, 108, 109] or a $M_{\rm PBH}$ which is much smaller than 10^{15} g (cannot exist today). In the current chapter we show that if m_χ and $M_{\rm PBH}$ are, respectively, in the range ~ 1 to few tens of MeV and $\sim 10^{15}$ to 10^{17} g, the corresponding IC fluxes (or at least a part of their frequency distributions) can be observed at the SKA for DM particle and PBH parameter spaces that are consistent with existing experiments including the Planck and various radio observations. Interestingly, IC fluxes do not depend on the B-field of the parent galaxy or galaxy cluster, as strongly as in the case of synchrotron fluxes.

In addition to the IC flux that we consider, one can also try to look for the photon fluxes generated directly in the annihilation/decay of MeV DM particles or in the evaporation of PBHs with masses in the aforementioned range [40, 80, 216]

7.3 Source functions for DM and PBHs

In order to estimate the IC flux, one first requires the electron/positron energy spectrum originating from DM particles or PBHs inside an astrophysical object. In case of DM pair-annihilation, this is obtained by using the source function $Q_e(E, r)$ [101, 108, 110] given in Eq. 2.1.1 of Chapter 2. The arguments E and r denote the energy (in MeV) of the produced $e^{\pm}$ and the radial distance of a point inside the target galaxy or galaxy cluster, respectively. We assume that all the MeV DM particles (denoted by χ) annihilate directly into e^+e^- final state and thus the weight factor B_f in Eq. 2.1.1 is 1 (or 100%) for the e^+e^- channel and zero for other SM channels. The source function for annihilation depends on $\langle\sigma v\rangle$, m_χ and the square of the DM density profile $\rho_\chi(r)$. For a scenario involving decaying DM, the expression of the source function used for annihilation changes a bit, while for the PBH evaporation, it is mainly governed by the Hawking radiation formula for a black hole.

The source function corresponding to a population of DM particles, decaying dominantly into e^+e^- final state, takes the following form [110],

$$Q_e^{\text{dec}}(E,r) = \Gamma \left(\frac{\rho_\chi(r)}{m_\chi}\right) \frac{dN^e}{dE}, \tag{7.3.1}$$

where Γ is the decay rate (in s^{-1}) of the DM particle χ and $\frac{dN^e}{dE}$ represents the electron (positron) energy distribution produced per DM decay in the e^+e^- channel. In order to satisfy the requirements of dark matter in our universe, the lifetime (Γ^{-1}) of χ is expected to exceed the age of the universe by several orders of magnitude [208]. In a decay scenario, each DM particle present inside a halo can decay individually, while in the case of pair-annihilation, two DM particles should come together to annihilate. This fact is reflected in the replacement of ρ_χ^2 and m_χ^2 in Eq. 2.1.1 by ρ_χ and m_χ, respectively, in Eq. 7.3.1. The presence of m_χ^2 or m_χ in the denominator of the equation of source function enhances the $e^\pm$ spectrum for MeV DM and thus causes amplification in the signal.

For PBHs, the electron/positron flux generated in the Hawking radiation can be estimated as [40, 223, 224],

$$Q_e^{\text{PBH}}(E,r) = f_{\text{PBH}} \left(\frac{\rho_\chi(r)}{M_{\text{PBH}}}\right) \frac{d\dot{N}^e}{dE}, \tag{7.3.2}$$

with

$$\frac{d\dot{N}^e}{dE} = \frac{1}{2\pi\hbar} \frac{\Gamma_e}{e^{\frac{E}{T_{\text{PBH}}}} + 1}. \tag{7.3.3}$$

Here $\frac{d\dot{N}^e}{dE}$ describes the electron/positron energy spectrum originating per unit time from the Hawking radiation of a single PBH. $\Gamma_e(E, M_{\text{PBH}})$ is the absorption coefficient for spin-$\frac{1}{2}$ particles like electrons. An approximated analytic expression of $\Gamma_e(E, M_{\text{PBH}})$ can be found in [223, 224]. T_{PBH} represents the black hole temperature and is expressed as $T_{\text{PBH}} = 1.06$ GeV $\times \frac{10^{13}\text{g}}{\text{M}_{\text{PBH}}}$ [210]. The quantity f_{PBH} (in Eq. 7.3.2) denotes the PBH fraction of the total DM density $\rho_\chi(r)$. All the PBHs are assumed to have the same mass M_{PBH} and their lifetime is taken to be larger than the age of the universe. The latter assumption is satisfied by the values of M_{PBH} considered here [40].

7.4 IC flux calculation

The $e^{\pm}$, after being emitted in the DM annihilation/decay or in the evaporation of PBHs, propagate through the galactic or cluster medium and give rise to an equilibrium density $\frac{dn}{dE}(E,r)$ which one can obtain by solving the same transport equation [101, 108, 128] shown in Eq. 2.2.1. The IC flux $S(\nu)$, as a function of the observation frequency ν, is acquired by folding this $\frac{dn}{dE}$ with the IC power spectrum $P_{\rm IC}(\nu,E)$ and integrating over the emission region (Ω) of the target [101, 108],

$$S(\nu) = \frac{1}{4\pi}\int d\Omega \int_{\rm los} dl \left(2\int dE \frac{dn}{dE} P_{\rm IC}\right), \tag{7.4.1}$$

where l is the line-of-sight (los) co-ordinate. The IC power spectrum $P_{\rm IC}(\nu,E)$ can be obtained by multiplying the IC scattering cross section ($\sigma_{\rm IC}(\nu,\epsilon,E)$) with the CMB photon number density ($\eta(\epsilon)$) and integrating over the appropriate range of energy ϵ,[1] [84, 101, 108, 215] (see Appendix A).

In case of MeV electrons, we have parameterised the diffusion term ($D(E)$) in Eq. 2.2.1 as [108, 116, 117],

$$D(E) = D_0\left(\frac{E}{E_0}\right)^{\gamma}, \tag{7.4.2}$$

where D_0 and γ are, respectively, the diffusion coefficient and diffusion index and $E_0 = 1$ GeV. Values of these parameters inside any galactic system are not very well constrained for sub-GeV electrons [216]. We have used some illustrative values of them, as well as scanned the possible range of parameter space. As discussed earlier, the term $b(E)$ in Eq. 2.2.1 describes the energy loss processes of the $e^{\pm}$ due to various types of electromagnetic effects such as IC scattering, synchrotron radiation, coulomb interaction, and bremsstrahlung. Readers are referred to [101, 108, 128, 136, 191] for the detailed parameterisation of $b(E)$ inside various targets like galaxy clusters, dSphs etc. It has also been discussed in detail in Chapter 2 (see Eq. 2.2.2). Note that the IC and synchrotron losses are proportional to the square of the electron energy (E) and hence are suppressed for MeV electrons in comparison to other loss processes. Due to the proximity of the local dSphs like the Segue I, the magnetic field strength and parameterisation of diffusion in them are influenced by the choices used for the Milky Way galaxy [117, 135, 137].

[1] CMB photon energy ϵ which produces the IC flux at $\nu = 10$ GHz for $E = 2$ MeV, lies typically in the range $\sim 7\times10^{-13} - \sim 4\times10^{-11}$ MeV (i.e. $\sim 0.2 - \sim 10$ GHz, if expressed in terms of the CMB photon frequency).

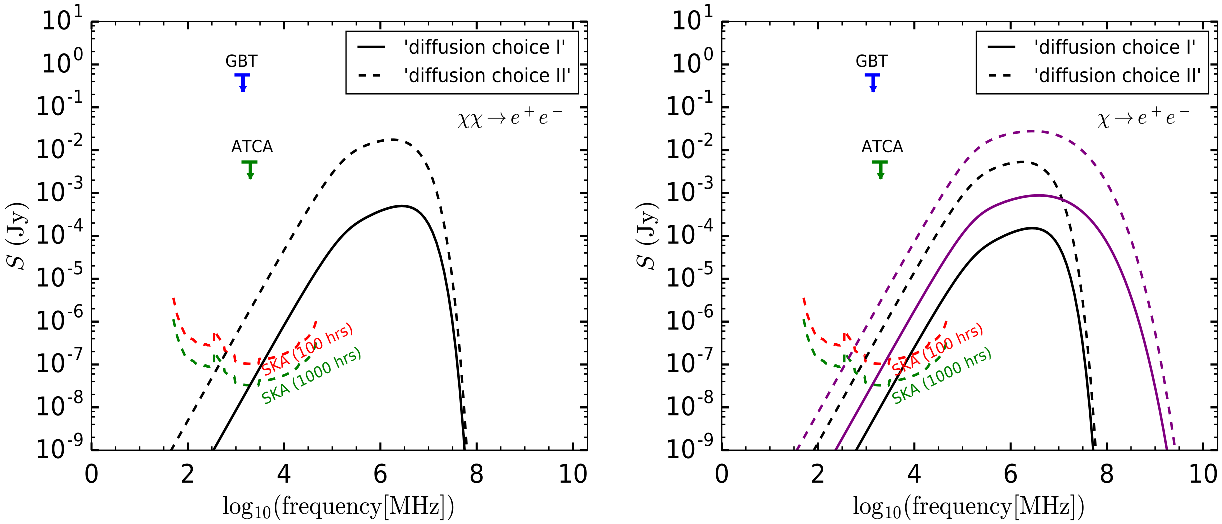

Figure 7.1: *Left panel*: IC fluxes S (black curves), generated in the annihilation of DM particles of mass 2 MeV inside Segue I. The annihilation channel is assumed to be $\chi\chi \to e^+e^-$ with an annihilation rate $\langle\sigma v\rangle = 10^{-28}\mathrm{cm}^3\mathrm{s}^{-1}$. Parameter choices for diffusion are shown in the inset. The red and green dashed lines represent the SKA sensitivities for 100 and 1000 hours, respectively [174]. The blue and green arrows indicate the upper limits on the radio flux obtained from GBT (1.4 GHz) [108, 117] and ATCA ($\sim$ 2 GHz) [135] observations, respectively, for Segue I or dSph identical to Segue I. *Right panel*: Similar fluxes as shown in the left panel, but originating from the IC scattering of the $e^{\pm}$ produced in a) the decay of 4 MeV DM ($\chi \to e^+e^-$) with a decay width $\Gamma = 10^{-25}\mathrm{s}^{-1}$ (black curves); and b) the evaporation of PBHs with mass $M_{\mathrm{PBH}} = 10^{16}$ g and a population of 5% of the total DM density of the dSph (purple curves).

In Figure 7.1, IC fluxes ($S(\nu)$) from the nearby dSph Segue I are shown for annihilating DM mass $m_\chi = 2$ MeV (left panel; black curves), decaying DM mass $m_\chi = 4$ MeV (right panel; black curves) and evaporating PBH mass $M_{\mathrm{PBH}} = 10^{16}$ g (right panel; purple curves). The DM distribution $\rho_\chi(r)$ for this dSph is assumed to follow a Einasto profile [126] with parameters similar to the ones found in [108, 117, 225]. The annihilation (decay) final state is assumed to be e^+e^- with a rate $\langle\sigma v\rangle = 10^{-28}\mathrm{cm}^3\mathrm{s}^{-1}$ ($\Gamma = 10^{-25}\mathrm{s}^{-1}$). In case of PBHs, it is assumed that these objects cover 5% of the total DM density of the dSph and all of them have the same mass M_{PBH}. Fluxes are estimated for two illustrative choices of D_0 and γ, namely, (I) $D_0 = 2.3 \times 10^{28}\mathrm{cm}^2\mathrm{s}^{-1}$; $\gamma = 0.46$ (solid curves) and (II) $D_0 = 3 \times 10^{27}\mathrm{cm}^2\mathrm{s}^{-1}$; $\gamma = 0.7$ (dashed curves) [108, 117]. We refer them as 'diffusion choice I' and 'diffusion choice II', respectively. These values are often used in the context of the Milky way galaxy [92,133,226]. The higher D_0 reduces the equilibrium electron/positron density $\left(\frac{dn}{dE}\right)$ in Eq. 2.2.1 and hence the flux in Eq. 7.4.1 (see reference [191]). Expected SKA sensitivities in the frequency range 50 MHz - 50 GHz for 100 and 1000 hours of observations are shown by the red and green dashed curves, respectively [174]. These sensitivities have been calculated using the documents provided in the SKA website [143]. See [191] for details of the analysis. Along with these, upper limits on the radio signal from the observations of Green Bank Telescope (GBT) [108, 117] and Australia Telescope Compact Array (ATCA) [135] towards Segue I or dSph similar to Segue I are also shown in both panels of the same figure by the blue and green arrows, respectively. It can be seen that, with parameter choices mentioned above, it is possible for the MeV DM or PBH induced IC fluxes to overcome the SKA threshold (mainly in the high frequency range, i.e., for $\nu \gtrsim 1$ GHz), by maintaining constraints from existing radio experiments.

One important point regarding the IC fluxes shown in Figure 7.1 is that, unlike synchrotron fluxes, they are weakly-dependent on the magnetic field (B). The main reason behind this is the absence of the B-field in the IC power spectrum $P_{\rm IC}$ [84,101,108], appearing in Eq. 7.4.1. There can be a B dependence in the $\frac{dn}{dE}$ itself, through the energy loss term $b(E)$ (see Eq. 2.2.1) pertaining to the synchrotron effect (which goes as B^2E^2) [101,108,128]. However, as pointed out earlier, this process is usually suppressed in case of MeV electrons for typical values of B present inside the galaxy clusters and dSphs [101, 135]. We have checked that the fluxes in Figure 7.1 vary at most by $\sim 6\%$ (at $\nu = 10$ GHz) for different values of B in the range 0 to 10 μG. Due to this very small variation, we can say that the results presented in this figure and hereafter are almost independent of the magnetic field B.

As a target for the MeV DM or PBH search in the context of SKA, we have mainly used the nearby ultra-faint dSphs such as Segue I and Ursa Major II [108,116,117]. As mentioned earlier in Chapter 3, these galaxies are appropriate for studying DM induced signals due to their low star formation rates which minimise the contribution of astrophysical processes. Their high DM contents (as inferred from their high mass-to-light ratios) and close proximity are of additional advantages. For comparison, we also present the results for the globular cluster ω-cen [124, 136, 193] and a galaxy cluster identical to the Coma cluster [101]. The ω-cen is almost ten times closer than any nearby dSph and may have DM density as high as any compact dwarf [124]. These make it useful for studies of DM [124, 136, 193]. The Coma cluster, on the other hand, also contains a significant amount of DM. As described in [101, 108], due to its large radius, the solution to the Eq. 2.2.1 is independent of diffusion inside this target.

7.5 Results

In Figure 7.2, thick solid and dashed curves show the threshold limits in the $\langle \sigma v \rangle - m_\chi$ (left column) and $\Gamma - m_\chi$ (right column) planes for observing any IC effect induced radio signal at the SKA with 100 hours of observation time. The DM annihilation and decay scenarios are $\chi\chi \to e^+e^-$ and $\chi \to e^+e^-$, respectively. The limits are shown for Segue I (green lines) and Ursa Major II (magenta lines) together with ω-cen (red lines) and Coma cluster (cyan lines). These limits are calculated following the analysis presented in [191]. As mentioned regarding the discussion of Figure 7.1, the DM density distribution for Segue I is described by a Einasto profile with profile information same as in [108, 117, 225]. For the other dSph Ursa major II and the globular cluster ω-cen, we assume the Navarro-Frenk-White (NFW) [125] DM profile following the parameterisations in references [116] and [124], respectively. In case of Coma we take a N04 profile [131] to represent the total DM distribution and along with this, add substructure contributions for the annihilation scenario (see [101] for details). Choices of diffusion parameters (D_0 and γ) for the dSph galaxies and the ω-cen are: $D_0 = 2.3 \times 10^{28} \mathrm{cm}^2\mathrm{s}^{-1}$; $\gamma = 0.46$ ('diffusion choice I' – thick solid curves) and $D_0 = 3 \times 10^{27} \mathrm{cm}^2\mathrm{s}^{-1}$; $\gamma = 0.7$ ('diffusion choice II' – thick dashed curves) [92, 108, 116, 117, 133]. The diffusion time-scale of MeV electrons in a big system like the Coma cluster is typically larger than their energy loss time-scale [101, 108]. As a result, the IC fluxes from Coma and hence the corresponding SKA limits (shown in this figure and the next) are independent of the diffusion. In addition to the SKA predictions, in each panel of Figure 7.2, constraints obtained using Planck's CMB data [93, 208], diffuse X-ray and γ-ray data from INTEGRAL [81, 215] and COMPTEL [81] and $e^\pm$ data from Voyager 1 [92] are indicated by various thin solid lines with different colors.

For dSphs and ω-cen, the SKA limits shown in Figure 7.2 depend on the choices of diffusion parameters but not on the magnetic field B (see the earlier discussions). For Coma they also are independent of the diffusion. In each case, the regions above the SKA limits and below the Planck and other existing constraints are the parameter spaces that are available for the future radio telescope SKA. In case of both annihilation and decay, these regions extend up to DM mass $m_\chi \simeq 20$ MeV.

Figure 7.3 demonstrates the SKA threshold limits (thick solid and dashed lines) on the

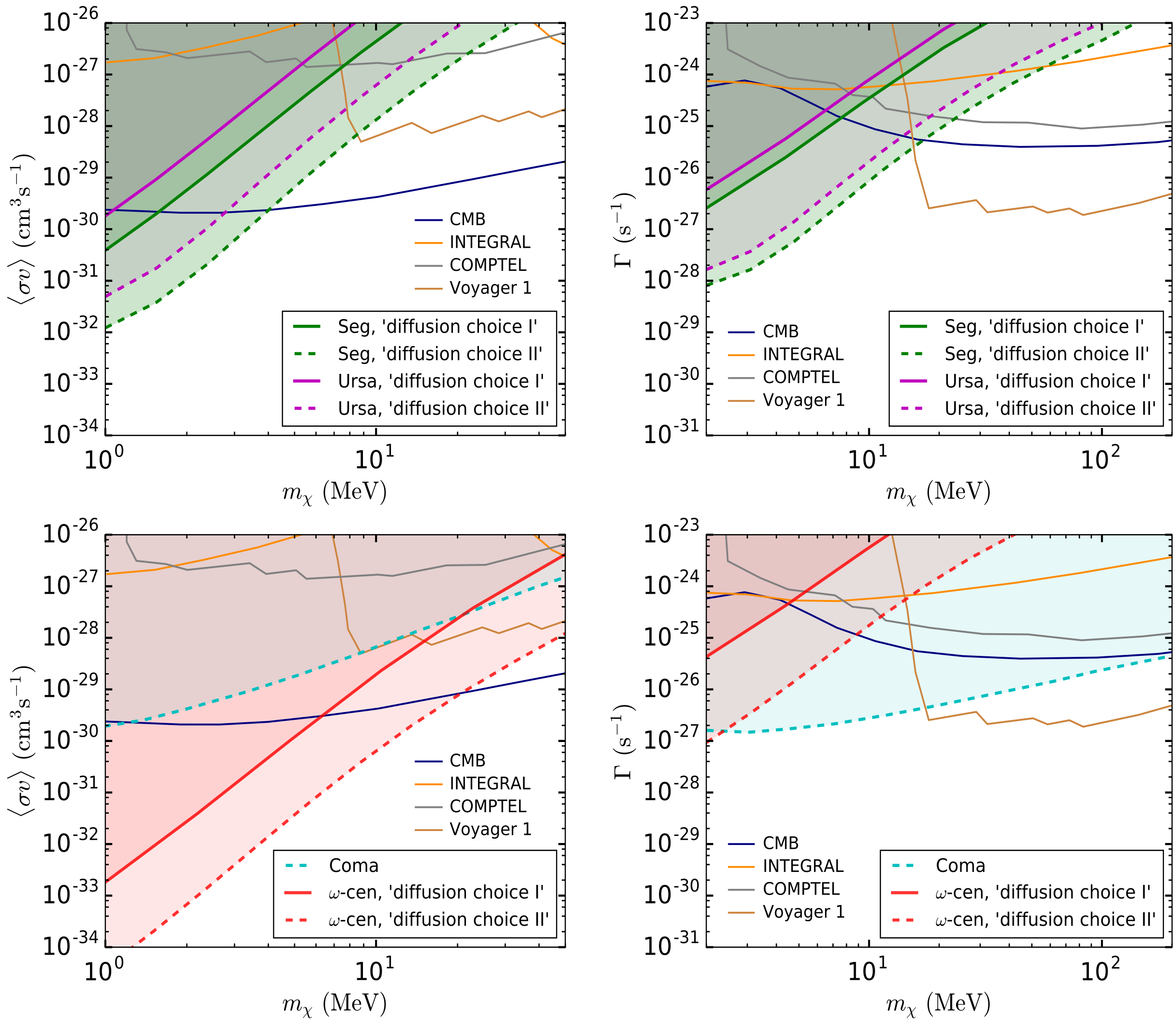

Figure 7.2: The thick solid and dashed lines (with shaded regions) represent the SKA threshold limits in the $\langle \sigma v \rangle - m_\chi$ (left column) and $\Gamma - m_\chi$ (right column) planes for detecting (in 100 hours observation) the DM induced IC fluxes produced in the e^+e^- channel. The limits are shown for different targets: Segue I (in green), Ursa Major II (in magenta), ω-cen (in red) and Coma cluster (in cyan). Parameter choices for diffusion are shown in the inset. In case of Coma, the limits are independent of D_0. Constraints coming from CMB data [93, 208], Voyager 1 [92], INTEGRAL [81, 215] and COMPTEL [81] are shown by various thin solid lines.

PBH fraction $f_{\rm PBH}$ as a function of the PBH mass ($M_{\rm PBH}$). Side-by-side, constraints estimated using CMB [209], extra-galactic (EG) γ-ray flux [227], 511 KeV line [228], Voyager

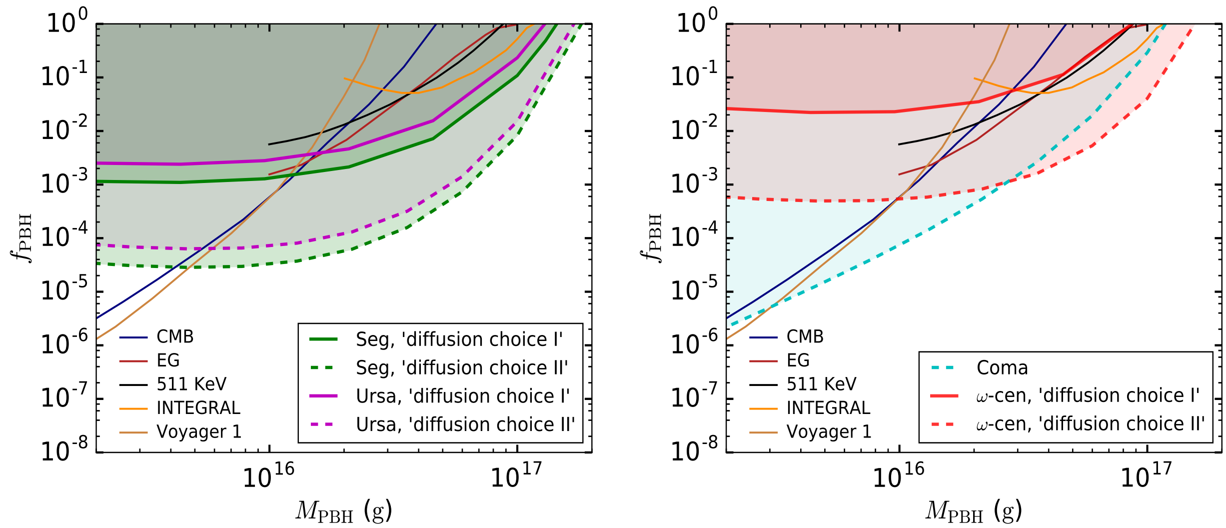

Figure 7.3: SKA 100 hours threshold limits (shown by the thick solid and dashed curves with shaded regions) in the $f_{\rm PBH} - M_{\rm PBH}$ plane for observing the IC fluxes which are produced by the IC scattering of the $e^{\pm}$ emitted in PBH evaporation. The limits are presented for different targets: Segue I and Ursa Major II (left panel), ω-cen and Coma cluster (right panel). Parameter choices for diffusion are in the inset. The limit in case of Coma is independent of D_0. Constraints from CMB [209], extra-galactic (EG) γ-ray emission [227], 511 keV line emission [228], INTEGRAL [82] and Voyager 1 [221] are shown by thin solid lines.

1 [221] and INTEGRAL [82] data are shown by different thin solid lines. The SKA limits for the dSphs Segue I and Ursa Major II are presented in the left panel of the figure, while the right panel depicts the limits for ω-cen and Coma cluster. Choices of all the astrophysical parameters are exactly the same as in Figure 7.2. The PBH parameter space that is consistent with existing data and can be constrained through the SKA is stretched over the PBH mass range $\sim 3 \times 10^{15} - \sim 10^{17}$ g. Note that PBHs with mass $M_{\rm PBH} < 10^{15}$ g do not exist in today's galactic halos, whereas for $M_{\rm PBH} > 10^{17}$ g, it is difficult to produce $e^{\pm}$ (which in turn generate the IC flux) in the Hawking radiation [40].

The SKA limits in Figures 7.2 and 7.3 assume some illustrative values of the diffusion coefficient D_0 and index γ. However, the lack of observational data makes it difficult to constrain these parameters in the MeV energy scale, for the galaxies including our own [216]. Keeping this fact in mind, we have varied those parameters over possible ranges and shown the allowed regions which can give rise to detectable signals at the SKA.

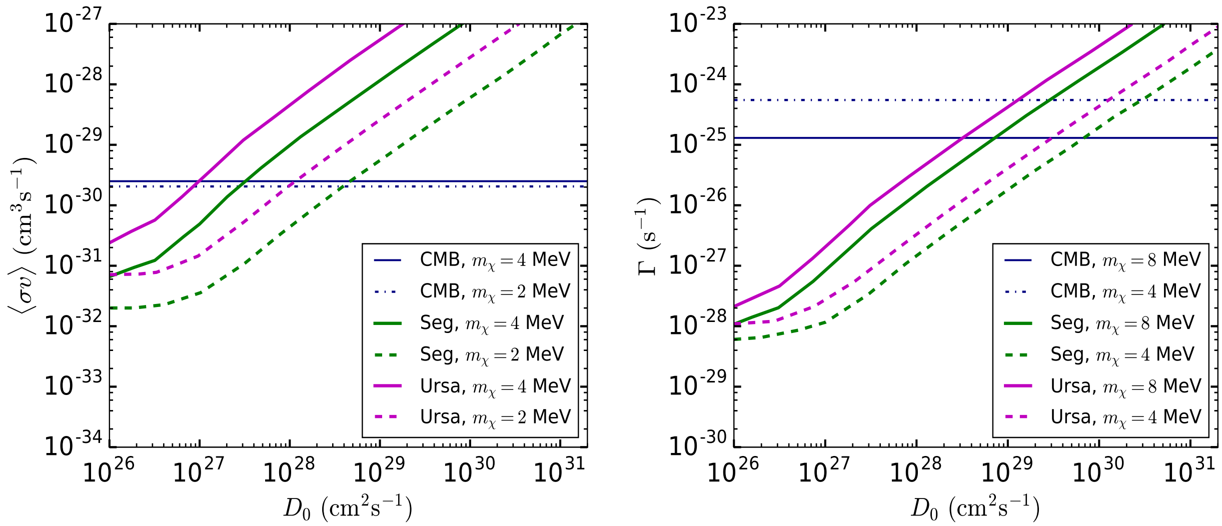

Figure 7.4: Limits in the $\langle \sigma v \rangle - D_0$ (left panel) and $\Gamma - D_0$ (right panel) planes to observe the DM induced IC fluxes at SKA (100 hours) from Segue I (green lines) and Ursa Major II (magenta lines) for different DM masses shown in the inset. The final state of annihilation and decay is e^+e^-. The limits are shown for $\gamma = 0.7$ [116, 117]. Corresponding CMB upper limits at those DM masses are indicated by the solid and dashed-dotted dark blue lines [93, 208].

In Figure 7.4, SKA threshold limits on DM annihilation rate $\langle \sigma v \rangle$ (left panel) and decay rate Γ (right panel) as a function of D_0 have been presented for the dSphs Segue I (green lines) and Ursa Major II (magenta lines), assuming $\gamma = 0.7$ [108, 116, 117]. These limits are for DM masses $m_\chi = 2$ and 4 MeV (in case of annihilation) and $m_\chi = 4$ and 8 MeV (in case of decay). Simultaneously, we have also shown the corresponding Planck's CMB constraints at those masses. The intersections of the SKA limits and the Planck's constraints indicate the ranges of D_0 (with $\gamma = 0.7$) which can be probed at the SKA for the dSphs under consideration. Detections of the IC effect induced radio signals for D_0 beyond these ranges would require such annihilation or decay rates that are already ruled out by the Planck. Similar types of plots can be obtained for the PBH fraction ($f_{\rm PBH}$) too.

Using some independent information on the MeV DM mass and the corresponding annihilation or decay rate, we identify the viable region in the $D_0 - \gamma$ plane, as has been shown in Figure 7.5. Here, the blue and red lines indicate the SKA limits in this plane for detecting the IC fluxes originating, respectively, from the annihilation and decay of DM particles into e^+e^- final state. These limits are estimated for the dSph Segue I. The DM

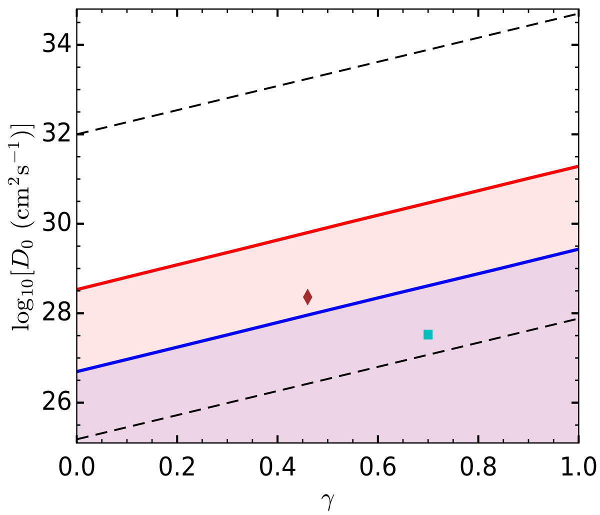

Figure 7.5: The blue (red) line represents the SKA 100 hours threshold limit in the $D_0 - \gamma$ plane for observing the IC flux produced by DM of mass $m_\chi = 2$ (4) MeV annihilating (decaying) into the e^+e^- channel from Segue 1. The corresponding $\langle\sigma v\rangle$ (Γ) is consistent with the upper limit obtained by Planck (see Figure 7.4). The shaded region below each line indicates the parameter space which can be probed or ruled out by the SKA. Two illustrative values of D_0 and γ, used in Figures 7.1, 7.2 and 7.3, are marked with brown and cyan points. The upper dashed line shows the maximum D_0 (at $E = 2$ MeV) allowed in a typical dwarf galaxy, while the lower dashed line depicts the limit on D_0 (at the same E), below which the IC flux from the galaxy is not sensitive to the diffusion (see the text for details).

masses are assumed to be $m_\chi = 2$ MeV (for annihilation) and $m_\chi = 4$ MeV (for decay). The corresponding $\langle\sigma v\rangle$ and Γ are kept fixed at the upper limits obtained from Planck's CMB observation. The index γ has been scanned over the range $0 \leq \gamma \leq 1$ [137, 216, 226]. For electron energies in the sub-GeV scale, the diffusion (in Eq. 7.4.2) gets stronger for lower γ and therefore suppresses the IC flux (see Eqs. 2.2.1 and 7.4.1). As a result, the limits in the $D_0 - \gamma$ plane become weaker for the smaller values of γ. The shaded region under each line in this figure represents the parameter space to be constrained by the SKA. For any γ, the values of D_0 above the blue (red) line will make the radio signals detectable at the SKA for $\langle\sigma v\rangle$ (Γ) larger than the Planck limit (see Figure 7.4). Note that, unlike in the case of synchrotron radiation [116, 117], radio limits presented here depend very feebly on the magnetic field B. Besides the SKA limits, we have shown another two possible bounds on D_0 in Figure 7.5. The upper black dashed line indicates the maximum D_0 (at electron energy $E = 2$ MeV) allowed in a dSph, having a length-scale ≈ 1 kpc. For D_0 above this line, the MeV electrons can have a diffusion velocity greater than the speed of light (c) (see the arguments of [135]). The lower black dashed line, on the other hand, shows the limit on D_0 (at $E = 2$ MeV), below which the diffusion time-scale of the $e^{\pm}$ in the dSph becomes larger than their energy loss time-scale and the corresponding IC fluxes are not sensitive to the diffusion anymore (see the discussion in [101]). One can repeat the whole analysis, described here, for the other dSph or ω-cen and simultaneously use the information on PBH in place of MeV DM. The measurements associated with the Segue I, Ursa Major II and the globular cluster ω-cen depend on D_0. However, the Coma cluster observations are independent of D_0. It is also possible to combine these measurements to determine D_0 and γ.

Apart from the SKA radio telescope project, various space based MeV range γ-ray experiments such as e-ASTROGAM [222], AMEGO [229], GRAMS [230], have been recently proposed and are expected to start their operations in the forthcoming years. These experiments will also play important roles in probing DM and PBHs in the mass domains considered in this chapter. For example, e-ASTROGAM, due its comparatively higher sensitivity [222], can constrain the DM annihilation rate and decay width (for e^+e^- final state) up to the values $\langle\sigma v\rangle \simeq 10^{-30}\text{cm}^3\text{s}^{-1}$ and $\Gamma \simeq 5\times10^{-27}\text{s}^{-1}$ respectively, for a DM mass (m_χ) $\simeq 2$ MeV [216]. These constraints are stronger by a few orders of magnitude in comparison to the corresponding limits coming from existing MeV γ-ray experiments like COMPTEL and INTEGRAL [81]. A similar conclusion also holds for PBHs with masses that lie between 10^{15} and 10^{17} g [222]. The future experiment AMEGO is predicted to give more or less same results as e-ASTROGAM [216, 227]. The GRAMS satellite mission, on the other hand, can have slightly better sensitivity (with a sufficient observation time) in measuring MeV photon signals [230] and thus may provide even more stringent constraints on both the DM and PBH parameter spaces. By comparing the aforementioned e-ASTROGAM estimations with the SKA limits from Figures 7.2 and 7.3, it can be seen that the SKA, in some cases, can have better constraints for $\langle\sigma v\rangle$ depending on the diffusion in the system, but independent of diffusion for Γ and f_{PBH} if one looks for a cluster scale object like Coma.

7.6 Conclusions

Investigating MeV scale signals for dark matter and PBHs is well motivated. For example, MeV scale dark matter searches are underway at ongoing and upcoming direct detection [231, 232], neutrino [233, 234] and various beam dump experiments, e.g., [235, 236]. There are also indirect detection proposals to probe the MeV sky by eAstrogram, GRAMS, AMEGO etc. The impact of MeV DM on ΔN_{eff} has been studied [237].

We present here a study of MeV DM and PBH searches at the upcoming SKA radio telescope, based on the observation of photon fluxes generated inside a galaxy or galaxy cluster via the IC scattering of MeV electrons-positrons on low energy CMB photons contained within that system. Both annihilation and decay of MeV DM are considered as sources for these MeV $e^{\pm}$. They may also be produced in the Hawking radiation from a population of PBHs in the mass range $10^{15} - 10^{17}$ g. We find that, depending on the DM particle and PBH masses and the values of astrophysical parameters, the corresponding IC fluxes can fall (at least partially) inside the SKA frequency band.

Assuming 100 hours of observation at the SKA and e^+e^- as the dominant final state, predicted threshold limits on DM annihilation rate and decay width are obtained for various DM masses in the MeV range. Similar limits on the PBH abundance are also presented. These limits are estimated using the aforementioned IC fluxes from the local ultra-faint galaxies Segue I and Ursa Major II, along with the globular cluster ω-cen and the Coma cluster, for illustrative choices of diffusion parameters D_0 and γ. Because of their production mechanism, IC fluxes and thus the SKA limits derived using them depend very weakly on the in-situ magnetic field. By juxtaposing the SKA limits with the Planck's CMB constraints, we find that the former experiment can provide better probe for DM particle masses up to few tens of MeV and for PBH masses above a factor times 10^{15} to 10^{17} g depending on the choices of diffusion parameters in the target systems. In parallel, we show that these SKA limits, even independently of the diffusion, can be stronger than the limits predicted by future MeV γ-ray experiments.

We additionally demonstrate how SKA observations can be used to constrain the diffusion parameter space of MeV electrons inside a dwarf galaxy. To illustrate this, we use some example values of the DM particle mass, together with its annihilation and decay rates which are kept fixed at the corresponding upper limits obtained from Plank's CMB data. Thus, the excluded regions in the aforementioned diffusion parameter space are expected to produce detectable signals at the SKA for annihilation or decay scenarios that are consistent with the CMB observation.

The SKA constraints, obtained in the MeV DM or PBH parameter space for targets like dSphs, are estimated using some well motivated choices of the diffusion parameters. At the same time, the regions in the diffusion parameter space of a dSph that are possible to exclude by the future SKA observation have been identified, using some illustrative MeV

DM scenarios consistent with existing indirect search constraints. The full multi-parameter space, spanned by the parameters of DM and diffusion, is difficult to constrain if one uses only the radio observation. However, some additional inputs from the observations of DM signals other than the radio signal may resolve the degeneracy. For example, if the future MeV γ-ray experiments like e-ASTROGAM, AMEGO, etc., observe any new γ-ray signal originating from DM, then by combining such observations with the SKA radio data from dSphs, one can constrain both the DM and the diffusion parameters simultaneously. In this regard, galaxy clusters such as Coma can be interesting places for the DM induced radio signal search, since the radio fluxes generated inside them do not depend on the diffusion.

Appendix A

Inverse Compton (IC) power

The power P_{IC}, emitted in the Inverse Compton (IC) scatterings of $e^{\pm}$ on background photons (for example, CMB), can be estimated as [84, 101, 108, 215],

$$P_{\text{IC}}(\nu, E) = c\, E_\nu \int d\epsilon\, \eta(\epsilon)\, \sigma_{\text{IC}}(E_\nu, \epsilon, E). \tag{A.0.1}$$

Here E is the energy of the incoming $e^{\pm}$, ν is the frequency of the scattered photon (the corresponding energy $E_\nu = h\nu$, h being the Planck constant), ϵ is the energy of the target photon and c is the speed of light. The function $\eta(\epsilon)$ denotes the number density of target photons per unit energy ϵ. For CMB photons, $\eta(\epsilon)$ is the black body spectrum at the temperature 2.73 K. The quantity σ_{IC} represents the IC scattering cross-section and is given by the following formula,

$$\sigma_{\text{IC}}(E_\nu, \epsilon, E) = \frac{3\sigma_T m_e^2}{4\epsilon E^2}\, \Lambda(q, \Gamma_e). \tag{A.0.2}$$

Here σ_T and m_e are the Thomson cross-section and the electron mass, respectively. $\Lambda(q, \Gamma_e)$ is given by:

$$\Lambda(q, \Gamma_e) = \left[2q\, ln\, q + (1 + 2q)(1 - q) + \frac{(\Gamma_e q)^2(1 - q)}{2(1 + \Gamma_e q)}\right], \tag{A.0.3}$$

where,

$$\Gamma_e = \frac{4\epsilon E}{m_e^2}, \qquad \text{and} \qquad q = \frac{E_\nu}{[\Gamma_e(E - E_\nu)]}. \tag{A.0.4}$$

The integration limits of ϵ in Eq. A.0.1 can be determined by using the following range of q, i.e., $m_e^2/4E^2 \leq q \leq 1$, which is set by the kinematics of the IC scattering process.

Appendix B

Convolution of the surface brightness with the telescope beam

Let $I(\nu, \Theta)$ be the surface brightness distribution corresponding to the radio synchrotron emission generated at a frequency ν due to DM annihilation inside a dwarf galaxy. Here Θ is the angular distance between the center of the source galaxy and an arbitrary point inside it. If the right ascension(RA) (a) and declination(DEC) (b) coordinates of the center and the point are ($a_{\rm C}$, $d_{\rm C}$) and ($a_{\rm P}$, $d_{\rm P}$) respectively, one can write:

$$cos(\Theta) = sin(d_{\rm C})sin(d_{\rm P}) + cos(d_{\rm C})cos(d_{\rm P})cos(a_{\rm C} - a_{\rm P}). \tag{B.0.1}$$

The surface brightness distribution (I), that should be seen by a radio telescope (like the Murchison Widefield Array (MWA)), is obtained by convolving the source signal $I(\nu, \Theta)$ with the telescope beam $G(a, d, w)$:

$$\mathrm{I}(a_i, d_j) = \sum_{m=-\infty}^{\infty} \sum_{n=-\infty}^{\infty} I(a_m, d_n)\, G(a_i - a_m, d_j - d_n, w). \tag{B.0.2}$$

Here $G(a, d, w)$ is a two-dimensional Gaussian profile which represents the telescope beam. The full width at half maximum (FWHM) of the beam is w. The indices $i(m)$ and $j(n)$ denote individual bins along the right ascension and declination coordinate axes, respectively. By comparing the convolved surface brightness (I) with the telescope data, one can put constraints on the DM parameter space.

Bibliography

[1] J. F. Donoghue, E. Golowich, and B. R. Holstein, *Dynamics of the standard model*, vol. 2. CUP, 2014.

[2] S. Weinberg, *A Model of Leptons*, *Phys. Rev. Lett.* **19** (1967) 1264–1266.

[3] S. L. Glashow, *Partial Symmetries of Weak Interactions*, *Nucl. Phys.* **22** (1961) 579–588.

[4] P. W. Higgs, *Broken symmetries and the masses of gauge bosons*, *Phys. Rev. Lett.* **13** (Oct, 1964) 508–509.

[5] G. S. Guralnik, C. R. Hagen, and T. W. B. Kibble, *Global conservation laws and massless particles*, *Phys. Rev. Lett.* **13** (Nov, 1964) 585–587.

[6] F. Englert and R. Brout, *Broken symmetry and the mass of gauge vector mesons*, *Phys. Rev. Lett.* **13** (Aug, 1964) 321–323.

[7] F. Zwicky, *Die Rotverschiebung von extragalaktischen Nebeln*, *Helv. Phys. Acta* **6** (1933) 110–127.

[8] S. Smith, *The Mass of the Virgo Cluster*, **83** (Jan., 1936) 23.

[9] V. C. Rubin and J. Ford, W. Kent, *Rotation of the Andromeda Nebula from a Spectroscopic Survey of Emission Regions*, **159** (Feb., 1970) 379.

[10] S. M. Faber and J. S. Gallagher, *Masses and mass-to-light ratios of galaxies*, *Annual Review of Astronomy and Astrophysics* **17** (1979), no. 1 135–187, [https://doi.org/10.1146/annurev.aa.17.090179.001031].

[11] V. C. Rubin, J. Ford, W. K., and N. Thonnard, *Rotational properties of 21 SC galaxies with a large range of luminosities and radii, from NGC 4605 (R=4kpc) to UGC 2885 (R=122kpc).*, **238** (June, 1980) 471–487.

[12] C.-L. Shan, *Theoretical Interpretation of Experimental Data from Direct Dark Matter Detection*, other thesis, 7, 2007.

[13] K. G. Begeman, A. H. Broeils, and R. H. Sanders, *Extended rotation curves of spiral galaxies: dark haloes and modified dynamics*, *Monthly Notices of the Royal Astronomical Society* **249** (04, 1991) 523–537, [https://academic.oup.com/mnras/article-pdf/249/3/523/18160929/mnras249-0523.pdf].

[14] S. M. Faber and R. E. Jackson, *Velocity dispersions and mass-to-light ratios for elliptical galaxies.*, **204** (Mar., 1976) 668–683.

[15] J. Binney and M. Merrifield, *Galactic Astronomy*. 1998.

[16] **WMAP** Collaboration, G. Hinshaw et al., *Five-Year Wilkinson Microwave Anisotropy Probe (WMAP) Observations: Data Processing, Sky Maps, and Basic Results*, *Astrophys. J. Suppl.* **180** (2009) 225–245, [arXiv:0803.0732].

[17] **Planck** Collaboration, P. A. R. Ade et al., *Planck 2015 results. XIII. Cosmological parameters*, *Astron. Astrophys.* **594** (2016) A13, [arXiv:1502.01589].

[18] D. Scott and G. F. Smoot, *Cosmic Microwave Background Mini-review*, *arXiv e-prints* (May, 2010) arXiv:1005.0555, [arXiv:1005.0555].

[19] D. Clowe, M. Bradac, A. H. Gonzalez, M. Markevitch, S. W. Randall, C. Jones, and D. Zaritsky, *A direct empirical proof of the existence of dark matter*, *Astrophys. J. Lett.* **648** (2006) L109–L113, [astro-ph/0608407].

[20] M. Markevitch, A. H. Gonzalez, D. Clowe, A. Vikhlinin, W. Forman, C. Jones, S. Murray, and W. Tucker, *Direct constraints on the dark matter self-interaction cross section from the merging galaxy cluster 1e 0657-56*, *The Astrophysical Journal* **606** (may, 2004) 819–824.

[21] D. Clowe, A. Gonzalez, and M. Markevitch, *Weak-Lensing Mass Reconstruction of the Interacting Cluster 1E 0657-558: Direct Evidence for the Existence of Dark Matter*, **604** (Apr., 2004) 596–603, [astro-ph/0312273].

[22] **Planck** Collaboration, N. Aghanim et al., *Planck 2018 results. VI. Cosmological parameters*, arXiv:1807.06209.

[23] **Planck** Collaboration, P. A. R. Ade et al., *Planck 2013 results. XVI. Cosmological parameters*, *Astron. Astrophys.* **571** (2014) A16, [arXiv:1303.5076].

[24] P. J. E. Peebles and B. Ratra, *The cosmological constant and dark energy*, *Rev. Mod. Phys.* **75** (Apr, 2003) 559–606.

[25] G. Jungman, M. Kamionkowski, and K. Griest, *Supersymmetric dark matter*, *Physics Reports* **267** (1996), no. 5 195–373.

[26] M. Drees and G. Gerbier, *Review of Particle Physics*, *Journal of Physics G Nuclear Physics* **33** (2006).

[27] P. Gondolo and G. Gelmini, *Cosmic abundances of stable particles: Improved analysis*, *Nucl. Phys.* **B360** (1991) 145–179.

[28] M. Drees, R. Godbole, and P. Roy, *Theory and phenomenology of sparticles: An account of four-dimensional N=1 supersymmetry in high energy physics*. 2004.

[29] S. P. Martin, *A Supersymmetry primer*, hep-ph/9709356. [Adv. Ser. Direct. High Energy Phys.18,1(1998)].

[30] D. Hooper and K. M. Zurek, *A Natural Supersymmetric Model with MeV Dark Matter*, *Phys. Rev. D* **77** (2008) 087302, [arXiv:0801.3686].

[31] M. Pospelov, A. Ritz, and M. B. Voloshin, *Secluded WIMP Dark Matter*, *Phys. Lett. B* **662** (2008) 53–61, [arXiv:0711.4866].

[32] C. Boehm, P. Fayet, and J. Silk, *Light and heavy dark matter particles*, *Phys. Rev. D* **69** (2004) 101302, [hep-ph/0311143].

[33] M. Dutra, M. Lindner, S. Profumo, F. S. Queiroz, W. Rodejohann, and C. Siqueira, *MeV Dark Matter Complementarity and the Dark Photon Portal*, *JCAP* **03** (2018) 037, [arXiv:1801.05447].

[34] Z. Kang, *View FImP miracle (by scale invariance) à la self-interaction*, *Phys. Lett. B* **751** (2015) 201–204, [arXiv:1505.06554].

[35] L. M. Krauss and F. Wilczek, *Discrete gauge symmetry in continuum theories*, *Phys. Rev. Lett.* **62** (Mar, 1989) 1221–1223.

[36] Y. Mambrini, S. Profumo, and F. S. Queiroz, *Dark Matter and Global Symmetries*, *Phys. Lett. B* **760** (2016) 807–815, [arXiv:1508.06635].

[37] S. Hawking, *Gravitationally Collapsed Objects of Very Low Mass*, *Monthly Notices of the Royal Astronomical Society* **152** (04, 1971) 75–78, [https://academic.oup.com/mnras/article-pdf/152/1/75/9360899/mnras152-0075.pdf].

[38] B. J. Carr and S. W. Hawking, *Black Holes in the Early Universe*, *Monthly Notices of the Royal Astronomical Society* **168** (08, 1974) 399–415, [https://academic.oup.com/mnras/article-pdf/168/2/399/8079885/mnras168-0399.pdf].

[39] G. F. Chapline, *Cosmological effects of primordial black holes*, **253** (Jan., 1975) 251–252.

[40] B. Carr, K. Kohri, Y. Sendouda, and J. Yokoyama, *New cosmological constraints on primordial black holes*, *Phys. Rev. D* **81** (2010) 104019, [arXiv:0912.5297].

[41] Y. Sofue, *Grand Rotation Curve and Dark Matter Halo in the Milky Way Galaxy*, *pasj* **64** (Aug., 2012) 75, [arXiv:1110.4431].

[42] J. Bovy and S. Tremaine, *On the local dark matter density*, *Astrophys. J.* **756** (2012) 89, [arXiv:1205.4033].

[43] F. Iocco, M. Pato, and G. Bertone, *Evidence for dark matter in the inner Milky Way*, *Nature Phys.* **11** (2015) 245–248, [arXiv:1502.03821].

[44] D. Y. Akimov et al., *WIMP-nucleon cross-section results from the second science run of ZEPLIN-III*, *Phys. Lett. B* **709** (2012) 14–20, [arXiv:1110.4769].

[45] **DEAP** Collaboration, R. Ajaj et al., *Search for dark matter with a 231-day exposure of liquid argon using DEAP-3600 at SNOLAB*, *Phys. Rev. D* **100** (2019), no. 2 022004, [arXiv:1902.04048].

[46] **DarkSide** Collaboration, P. Agnes et al., *Low-Mass Dark Matter Search with the DarkSide-50 Experiment*, *Phys. Rev. Lett.* **121** (2018), no. 8 081307, [arXiv:1802.06994].

[47] **PandaX-II** Collaboration, X. Cui et al., *Dark Matter Results From 54-Ton-Day Exposure of PandaX-II Experiment*, *Phys. Rev. Lett.* **119** (2017), no. 18 181302, [arXiv:1708.06917].

[48] **XENON** Collaboration, E. Aprile et al., *Dark Matter Search Results from a One Ton-Year Exposure of XENON1T*, *Phys. Rev. Lett.* **121** (2018), no. 11 111302, [arXiv:1805.12562].

[49] **LUX Collaboration** Collaboration, D. S. Akerib et al., *Limits on spin-dependent wimp-nucleon cross section obtained from the complete lux exposure*, *Phys. Rev. Lett.* **118** (Jun, 2017) 251302.

[50] **PICO** Collaboration, C. Amole et al., *Dark Matter Search Results from the Complete Exposure of the PICO-60 C_3F_8 Bubble Chamber*, *Phys. Rev. D* **100** (2019), no. 2 022001, [arXiv:1902.04031].

[51] E. Behnke et al., *Final Results of the PICASSO Dark Matter Search Experiment*, *Astropart. Phys.* **90** (2017) 85–92, [arXiv:1611.01499].

[52] **SuperCDMS** Collaboration, R. Agnese et al., *First Dark Matter Constraints from a SuperCDMS Single-Charge Sensitive Detector*, *Phys. Rev. Lett.* **121** (2018), no. 5 051301, [arXiv:1804.10697]. [Erratum: Phys.Rev.Lett. 122, 069901 (2019)].

[53] **CRESST** Collaboration, A. H. Abdelhameed et al., *First results from the CRESST-III low-mass dark matter program*, *Phys. Rev. D* **100** (2019), no. 10 102002, [arXiv:1904.00498].

[54] M. Schumann, *Direct Detection of WIMP Dark Matter: Concepts and Status*, *J. Phys. G* **46** (2019), no. 10 103003, [arXiv:1903.03026].

[55] M. Pierre, *Dark Matter phenomenology : from simplified WIMP models to refined alternative solutions*. PhD thesis, Orsay, 2018. arXiv:1901.05822.

[56] C. Savage, G. Gelmini, P. Gondolo, and K. Freese, *Compatibility of DAMA/LIBRA dark matter detection with other searches*, *JCAP* **04** (2009) 010, [arXiv:0808.3607].

[57] **Super-Kamiokande** Collaboration, K. Choi et al., *Search for neutrinos from annihilation of captured low-mass dark matter particles in the Sun by Super-Kamiokande*, *Phys. Rev. Lett.* **114** (2015), no. 14 141301, [arXiv:1503.04858].

[58] **IceCube** Collaboration, M. G. Aartsen et al., *Search for annihilating dark matter in the Sun with 3 years of IceCube data*, *Eur. Phys. J. C* **77** (2017), no. 3 146, [arXiv:1612.05949]. [Erratum: Eur.Phys.J.C 79, 214 (2019)].

[59] **CMS** Collaboration, A. M. Sirunyan et al., *Searches for physics beyond the standard model with the M_{T2} variable in hadronic final states with and without disappearing tracks in proton-proton collisions at $\sqrt{s}$ = 13 TeV*, *Eur. Phys. J. C* **80** (2020), no. 1 3, [arXiv:1909.03460].

[60] L. Shchutska, *Prospects for bsm searches at the high-luminosity lhc with the cms detector*, *Nuclear and Particle Physics Proceedings* **273-275** (2016) 656 – 661. 37th International Conference on High Energy Physics (ICHEP).

[61] **CMS** Collaboration, A. M. Sirunyan et al., *Searches for pair production of charginos and top squarks in final states with two oppositely charged leptons in proton-proton collisions at $\sqrt{s}$ = 13 TeV*, *JHEP* **11** (2018) 079, [arXiv:1807.07799].

[62] **DELPHI** Collaboration, J. Abdallah et al., *Searches for supersymmetric particles in e+ e- collisions up to 208-GeV and interpretation of the results within the MSSM*, *Eur. Phys. J. C* **31** (2003) 421–479, [hep-ex/0311019].

[63] **CMS** Collaboration, A. M. Sirunyan et al., *Search for dark matter produced in association with a leptonically decaying Z boson in proton-proton collisions at $\sqrt{s}$ = 13 TeV*, *Eur. Phys. J. C* **81** (2021), no. 1 13, [arXiv:2008.04735].

[64] **ATLAS** Collaboration, G. Aad et al., *Search for new phenomena in events with an energetic jet and missing transverse momentum in pp collisions at $\sqrt{s} = 13$ TeV with the ATLAS detector*, arXiv:2102.10874.

[65] E. Izaguirre, G. Krnjaic, P. Schuster, and N. Toro, *Analyzing the discovery potential for light dark matter*, *Phys. Rev. Lett.* **115** (Dec, 2015) 251301.

[66] F. C. van den Bosch and R. A. Swaters, *Dwarf galaxy rotation curves and the core problem of dark matter halos*, *Mon. Not. Roy. Astron. Soc.* **325** (2001) 1017, [astro-ph/0006048].

[67] K. Spekkens and R. Giovanelli, *The Cusp/core problem in Galactic halos: Long-slit spectra for a large dwarf galaxy sample*, *Astron. J.* **129** (2005) 2119–2137, [astro-ph/0502166].

[68] R. Jimenez, L. Verde, and S. P. Oh, *Dark halo properties from rotation curves*, *Mon. Not. Roy. Astron. Soc.* **339** (2003) 243, [astro-ph/0201352].

[69] E. L. Lokas and G. A. Mamon, *Dark matter distribution in the Coma cluster from galaxy kinematics: Breaking the mass - anisotropy degeneracy*, *Mon. Not. Roy. Astron. Soc.* **343** (2003) 401, [astro-ph/0302461].

[70] **The Fermi-LAT Collaboration** Collaboration, M. Ackermann et al., *Searching for dark matter annihilation from milky way dwarf spheroidal galaxies with six years of fermi large area telescope data*, *Phys. Rev. Lett.* **115** (Nov, 2015) 231301.

[71] **Fermi-LAT, DES** Collaboration, A. Albert et al., *Searching for Dark Matter Annihilation in Recently Discovered Milky Way Satellites with Fermi-LAT*, *Astrophys. J.* **834** (2017), no. 2 110, [arXiv:1611.03184].

[72] G. Weidenspointner, *The Origin of the Cosmic Gamma-Ray Background in the COMPTEL Energy Range*. Dissertation, Technische Universität München, München, 1999.

[73] S. C. Kappadath, *Measurement of the Cosmic Diffuse Gamma-Ray Spectrum from 800 KEV to 30 Mev*. PhD thesis, UNIVERSITY OF NEW HAMPSHIRE, Jan., 1998.

[74] D. J. Thompson, D. L. Bertsch, C. E. Fichtel, R. C. Hartman, R. Hofstadter, E. B. Hughes, S. D. Hunter, B. W. Hughlock, G. Kanbach, D. A. Kniffen, Y. C. Lin, J. R. Mattox, H. A. Mayer-Hasselwander, C. von Montigny, P. L. Nolan, H. I. Nel, K. Pinkau, H. Rothermel, E. J. Schneid, M. Sommer, P. Sreekumar, D. Tieger, and A. H. Walker, *Calibration of the Energetic Gamma-Ray Experiment Telescope (EGRET) for the Compton Gamma-Ray Observatory*, **86** (June, 1993) 629.

[75] **H.E.S.S.** Collaboration, H. Abdallah et al., *Search for dark matter annihilations towards the inner Galactic halo from 10 years of observations with H.E.S.S*, *Phys. Rev. Lett.* **117** (2016), no. 11 111301, [arXiv:1607.08142].

[76] J. Aleksić et al., *Optimized dark matter searches in deep observations of Segue 1 with MAGIC*, *JCAP* **02** (2014) 008, [arXiv:1312.1535].

[77] **HAWC** Collaboration, M. A. Mostafá, *The High-Altitude Water Cherenkov Observatory*, *Braz. J. Phys.* **44** (2014) 571–580, [arXiv:1310.7237].

[78] **CTA Consortium** Collaboration, B. S. Acharya et al., *Science with the Cherenkov Telescope Array*. WSP, 11, 2018.

[79] A. Viana, H. Schoorlemmer, A. Albert, V. de Souza, J. P. Harding, and J. Hinton, *Searching for Dark Matter in the Galactic Halo with a Wide Field of View TeV Gamma-ray Observatory in the Southern Hemisphere*, *JCAP* **12** (2019) 061, [arXiv:1906.03353].

[80] K. K. Boddy and J. Kumar, *Indirect Detection of Dark Matter Using MeV-Range Gamma-Ray Telescopes*, *Phys. Rev. D* **92** (2015), no. 2 023533, [arXiv:1504.04024].

[81] R. Essig, E. Kuflik, S. D. McDermott, T. Volansky, and K. M. Zurek, *Constraining Light Dark Matter with Diffuse X-Ray and Gamma-Ray Observations*, *JHEP* **11** (2013) 193, [arXiv:1309.4091].

[82] R. Laha, J. B. Muñoz, and T. R. Slatyer, *integral constraints on primordial black holes and particle dark matter*, *Phys. Rev. D* **101** (Jun, 2020) 123514.

[83] A. Cuoco, J. Heisig, M. Korsmeier, and M. Krämer, *Constraining heavy dark matter with cosmic-ray antiprotons*, *JCAP* **1804** (2018), no. 04 004, [arXiv:1711.05274].

[84] M. Cirelli, G. Corcella, A. Hektor, G. Hutsi, M. Kadastik, P. Panci, M. Raidal, F. Sala, and A. Strumia, *PPPC 4 DM ID: A Poor Particle Physicist Cookbook for Dark Matter Indirect Detection*, *JCAP* **1103** (2011) 051, [arXiv:1012.4515]. [Erratum: JCAP1210,E01(2012)].

[85] C. Evoli, D. Gaggero, A. Vittino, G. Di Bernardo, M. Di Mauro, A. Ligorini, P. Ullio, and D. Grasso, *Cosmic-ray propagation with DRAGON2: I. numerical solver and astrophysical ingredients*, *JCAP* **02** (2017) 015, [arXiv:1607.07886].

[86] C. Evoli, D. Gaggero, D. Grasso, and L. Maccione, *Cosmic-Ray Nuclei, Antiprotons and Gamma-rays in the Galaxy: a New Diffusion Model*, *JCAP* **10** (2008) 018, [arXiv:0807.4730]. [Erratum: JCAP 04, E01 (2016)].

[87] **AMS** Collaboration, M. Aguilar et al., *Antiproton Flux, Antiproton-to-Proton Flux Ratio, and Properties of Elementary Particle Fluxes in Primary Cosmic Rays Measured with the Alpha Magnetic Spectrometer on the International Space Station*, *Phys. Rev. Lett.* **117** (2016), no. 9 091103.

[88] O. Adriani, G. C. Barbarino, G. A. Bazilevskaya, R. Bellotti, M. Boezio, E. A. Bogomolov, L. Bonechi, M. Bongi, V. Bonvicini, S. Borisov, S. Bottai, A. Bruno, F. Cafagna, D. Campana, R. Carbone, P. Carlson, M. Casolino, G. Castellini,

L. Consiglio, M. P. de Pascale, C. de Santis, N. de Simone, V. di Felice, A. M. Galper, W. Gillard, L. Grishantseva, P. Hofverberg, G. Jerse, A. V. Karelin, S. V. Koldashov, S. Y. Krutkov, A. N. Kvashnin, A. Leonov, V. Malvezzi, L. Marcelli, A. G. Mayorov, W. Menn, V. V. Mikhailov, E. Mocchiutti, A. Monaco, N. Mori, N. Nikonov, G. Osteria, P. Papini, M. Pearce, P. Picozza, C. Pizzolotto, M. Ricci, S. B. Ricciarini, L. Rossetto, M. Simon, R. Sparvoli, P. Spillantini, Y. I. Stozhkov, A. Vacchi, E. Vannuccini, G. Vasilyev, S. A. Voronov, J. Wu, Y. T. Yurkin, G. Zampa, N. Zampa, V. G. Zverev, and PAMELA Collaboration, *PAMELA Results on the Cosmic-Ray Antiproton Flux from 60 MeV to 180 GeV in Kinetic Energy*, **105** (Sept., 2010) 121101, [arXiv:1007.0821].

[89] **BESS** Collaboration, S. Orito et al., *Precision measurement of cosmic ray anti-proton spectrum*, *Phys. Rev. Lett.* **84** (2000) 1078–1081, [astro-ph/9906426].

[90] K. Abe, H. Fuke, S. Haino, T. Hams, M. Hasegawa, A. Horikoshi, K. C. Kim, A. Kusumoto, M. H. Lee, Y. Makida, S. Matsuda, Y. Matsukawa, J. W. Mitchell, J. Nishimura, M. Nozaki, R. Orito, J. F. Ormes, K. Sakai, M. Sasaki, E. S. Seo, R. Shinoda, R. E. Streitmatter, J. Suzuki, K. Tanaka, N. Thakur, T. Yamagami, A. Yamamoto, T. Yoshida, and K. Yoshimura, *Measurement of the Cosmic-Ray Antiproton Spectrum at Solar Minimum with a Long-Duration Balloon Flight over Antarctica*, **108** (Feb., 2012) 051102, [arXiv:1107.6000].

[91] E. C. Stone, A. C. Cummings, F. B. McDonald, B. C. Heikkila, N. Lal, and W. R. Webber, *Voyager 1 Observes Low-Energy Galactic Cosmic Rays in a Region Depleted of Heliospheric Ions*, *Science* **341** (July, 2013) 150–153.

[92] M. Boudaud, J. Lavalle, and P. Salati, *Novel cosmic-ray electron and positron constraints on MeV dark matter particles*, *Phys. Rev. Lett.* **119** (2017), no. 2 021103, [arXiv:1612.07698].

[93] T. R. Slatyer, *Indirect dark matter signatures in the cosmic dark ages. I. Generalizing the bound on s-wave dark matter annihilation from Planck results*, *Phys. Rev. D* **93** (2016), no. 2 023527, [arXiv:1506.03811].

[94] C. A. Argüelles, A. Diaz, A. Kheirandish, A. Olivares-Del-Campo, I. Safa, and A. C. Vincent, *Dark Matter Annihilation to Neutrinos*, arXiv:1912.09486.

[95] B. Dasgupta and R. Laha, *Neutrinos in IceCube/KM3NeT as probes of Dark Matter Substructures in Galaxy Clusters*, *Phys. Rev. D* **86** (2012) 093001, [arXiv:1206.1322].

[96] A. Hektor, M. Raidal, A. Strumia, and E. Tempel, *The cosmic-ray positron excess from a local dark matter over-density*, *Physics Letters B* **728** (2014) 58 – 62.

[97] Y. Bai, J. Berger, and S. Lu, *Supersymmetric resonant dark matter: A thermal model for the ams-02 positron excess*, *Phys. Rev. D* **97** (Jun, 2018) 115012.

[98] I. Cholis, T. Linden, and D. Hooper, *A Robust Excess in the Cosmic-Ray Antiproton Spectrum: Implications for Annihilating Dark Matter*, arXiv:1903.02549.

[99] M.-Y. Cui, X. Pan, Q. Yuan, Y.-Z. Fan, and H.-S. Zong, *Revisit of cosmic ray antiprotons from dark matter annihilation with updated constraints on the background model from AMS-02 and collider data*, *JCAP* **1806** (2018), no. 06 024, [arXiv:1803.02163].

[100] M. Regis et al., *Local Group dSph radio survey with ATCA (III): constraints on particle dark matter*, **10** (Oct., 2014) 016, [arXiv:1407.4948].

[101] S. Colafrancesco, S. Profumo, and P. Ullio, *Multi-frequency analysis of neutralino dark matter annihilations in the Coma cluster*, *Astron. Astrophys.* **455** (2006) 21, [astro-ph/0507575].

[102] T. Daylan, D. P. Finkbeiner, D. Hooper, T. Linden, S. K. N. Portillo, N. L. Rodd, and T. R. Slatyer, *The characterization of the gamma-ray signal from the central Milky Way: A case for annihilating dark matter*, *Phys. Dark Univ.* **12** (2016) 1–23, [arXiv:1402.6703].

[103] F. Calore, I. Cholis, C. McCabe, and C. Weniger, *A Tale of Tails: Dark Matter Interpretations of the Fermi GeV Excess in Light of Background Model Systematics*, *Phys. Rev.* **D91** (2015), no. 6 063003, [arXiv:1411.4647].

[104] C. Karwin, S. Murgia, T. M. P. Tait, T. A. Porter, and P. Tanedo, *Dark Matter Interpretation of the Fermi-LAT Observation Toward the Galactic Center*, *Phys. Rev.* **D95** (2017), no. 10 103005, [arXiv:1612.05687].

[105] G. Beck and S. Colafrancesco, *A Multi-frequency analysis of possible Dark Matter Contributions to M31 Gamma-Ray Emissions*, *JCAP* **1710** (2017) 007, [arXiv:1707.09787].

[106] A. Achterberg, M. van Beekveld, W. Beenakker, S. Caron, and L. Hendriks, *Comparing Galactic Center MSSM dark matter solutions to the Reticulum II gamma-ray data*, *JCAP* **1512** (2015), no. 12 013, [arXiv:1507.04644].

[107] R. K. Leane, T. R. Slatyer, J. F. Beacom, and K. C. Y. Ng, *GeV-scale thermal WIMPs: Not even slightly ruled out*, *Phys. Rev. D* **98** (2018), no. 2 023016, [arXiv:1805.10305].

[108] A. McDaniel, T. Jeltema, S. Profumo, and E. Storm, *Multiwavelength Analysis of Dark Matter Annihilation and RX-DMFIT*, *JCAP* **1709** (2017), no. 09 027, [arXiv:1705.09384].

[109] G. Beck and S. Colafrancesco, *A Multi-frequency analysis of dark matter annihilation interpretations of recent anti-particle and γ-ray excesses in cosmic structures*, *JCAP* **1605** (2016), no. 05 013, [arXiv:1508.01386].

[110] M. Regis, L. Richter, and S. Colafrancesco, *Dark matter in the Reticulum II dSph: a radio search*, *JCAP* **1707** (2017), no. 07 025, [arXiv:1703.09921].

[111] M. Regis, S. Colafrancesco, S. Profumo, W. J. G. de Blok, M. Massardi, and L. Richter, *Local Group dSph radio survey with ATCA (III): Constraints on Particle Dark Matter*, *JCAP* **1410** (2014), no. 10 016, [arXiv:1407.4948].

[112] M. Drees and C.-L. Shan, *Reconstructing the Velocity Distribution of WIMPs from Direct Dark Matter Detection Data*, *JCAP* **06** (2007) 011, [astro-ph/0703651].

[113] R. C. Gilmore, *Mass limits on neutralino dark matter*, *Phys. Rev.* **D76** (2007) 043520, [arXiv:0705.2610].

[114] S. Colafrancesco and B. Mele, *Neutralinos and the origin of radio halos in clusters of galaxies*, *Astrophys. J.* **562** (2001) 24–41, [astro-ph/0008127].

[115] S. Rudaz and F. W. Stecker, *Cosmic-ray antiprotons, positrons, and gamma rays from halo dark matter annihilation*, *Astrophys. J.* **325** (feb, 1988) 16–25.

[116] A. Natarajan, J. B. Peterson, T. C. Voytek, K. Spekkens, B. Mason, J. Aguirre, and B. Willman, *Bounds on Dark Matter Properties from Radio Observations of Ursa Major II using the Green Bank Telescope*, *Phys. Rev.* **D88** (2013) 083535, [arXiv:1308.4979].

[117] A. Natarajan, J. E. Aguirre, K. Spekkens, and B. S. Mason, *Green Bank Telescope Constraints on Dark Matter Annihilation in Segue I*, arXiv:1507.03589.

[118] M. Kamionkowski and M. S. Turner, *Distinctive positron feature from particle dark-matter annihilations in the galatic halo*, *Phys. Rev. D* **43** (Mar, 1991) 1774–1780.

[119] T. Sjöstrand, S. Ask, J. R. Christiansen, R. Corke, N. Desai, P. Ilten, S. Mrenna, S. Prestel, C. O. Rasmussen, and P. Z. Skands, *An introduction to PYTHIA 8.2*, *Comput. Phys. Commun.* **191** (2015) 159–177, [arXiv:1410.3012].

[120] G. Bélanger, F. Boudjema, A. Pukhov, and A. Semenov. http://lapth.cnrs.fr/micromegas/.

[121] G. Belanger, F. Boudjema, P. Brun, A. Pukhov, S. Rosier-Lees, P. Salati, and A. Semenov, *Indirect search for dark matter with micrOMEGAs2.4*, *Comput. Phys. Commun.* **182** (2011) 842–856, [arXiv:1004.1092].

[122] A. Geringer-Sameth, S. M. Koushiappas, and M. Walker, *Dwarf galaxy annihilation and decay emission profiles for dark matter experiments*, *Astrophys. J.* **801** (2015), no. 2 74, [arXiv:1408.0002].

[123] J. Choquette, *Constraining Dwarf Spheroidal Dark Matter Halos With The Galactic Center Excess*, *Phys. Rev.* **D97** (2018), no. 4 043017, [arXiv:1705.09676].

[124] A. M. Brown, R. Massey, T. Lacroix, L. E. Strigari, A. Fattahi, and C. Bœhm, *The glow of annihilating dark matter in Omega Centauri*, *arXiv e-prints* (Jul, 2019) arXiv:1907.08564, [arXiv:1907.08564].

[125] J. F. Navarro, C. S. Frenk, and S. D. M. White, *The Structure of cold dark matter halos*, *Astrophys. J.* **462** (1996) 563–575, [astro-ph/9508025].

[126] J. Einasto, *On the Construction of a Composite Model for the Galaxy and on the Determination of the System of Galactic Parameters*, *Trudy Astrofizicheskogo Instituta Alma-Ata* **5** (Jan., 1965) 87–100.

[127] N. Hiroshima, M. Hayashida, and K. Kohri, *Dependence of accessible dark matter annihilation cross-sections on the density profiles of dwarf spheroidal galaxies with the Cherenkov Telescope Array*, *Phys. Rev. D* **99** (2019), no. 12 123017, [arXiv:1905.12940].

[128] S. Colafrancesco, S. Profumo, and P. Ullio, *Detecting dark matter WIMPs in the Draco dwarf: A multi-wavelength perspective*, *Phys. Rev.* **D75** (2007) 023513, [astro-ph/0607073].

[129] J. Diemand, M. Zemp, B. Moore, J. Stadel, and M. Carollo, *Cusps in cold dark matter haloes*, *Mon. Not. Roy. Astron. Soc.* **364** (2005) 665, [astro-ph/0504215].

[130] A. Burkert, *The Structure of dark matter halos in dwarf galaxies*, *IAU Symp.* **171** (1996) 175, [astro-ph/9504041]. [Astrophys. J.447,L25(1995)].

[131] J. F. Navarro, E. Hayashi, C. Power, A. Jenkins, C. S. Frenk, S. D. White, V. Springel, J. Stadel, and T. R. Quinn, *The Inner structure of Lambda-CDM halos 3: Universality and asymptotic slopes*, *Mon. Not. Roy. Astron. Soc.* **349** (2004) 1039, [astro-ph/0311231].

[132] T. Delahaye, F. Donato, N. Fornengo, J. Lavalle, R. Lineros, P. Salati, and R. Taillet, *Galactic secondary positron flux at the Earth*, *Astron. Astrophys.* **501** (2009) 821–833, [arXiv:0809.5268].

[133] J. Buch, M. Cirelli, G. Giesen, and M. Taoso, *PPPC 4 DM secondary: A Poor Particle Physicist Cookbook for secondary radiation from Dark Matter*, *JCAP* **09** (2015) 037, [arXiv:1505.01049].

[134] E. Carretti, R. M. Crocker, L. Staveley-Smith, M. Haverkorn, C. Purcell, B. M. Gaensler, G. Bernardi, M. J. Kesteven, and S. Poppi, *Giant Magnetized Outflows from the Centre of the Milky Way*, *Nature* **493** (2013) 66, [arXiv:1301.0512].

[135] M. Regis, L. Richter, S. Colafrancesco, S. Profumo, W. J. G. de Blok, and M. Massardi, *Local Group dSph radio survey with ATCA – II. Non-thermal diffuse emission*, *Mon. Not. Roy. Astron. Soc.* **448** (2015), no. 4 3747–3765, [arXiv:1407.5482].

[136] A. Kar, B. Mukhopadhyaya, S. Tingay, B. McKinley, M. Haverkorn, S. McSweeney, N. Hurley-Walker, S. Mitra, and T. R. Choudhury, *Dark matter annihilation in ω*

Centauri: Astrophysical implications derived from the MWA radio data, *Phys. Dark Univ.* **30** (2020) 100689, [arXiv:2005.11962].

[137] T. E. Jeltema and S. Profumo, *Searching for Dark Matter with X-ray Observations of Local Dwarf Galaxies*, *Astrophys. J.* **686** (2008) 1045, [arXiv:0805.1054].

[138] P. Rebusco, E. Churazov, H. Bohringer, and W. Forman, *Impact of stochastic gas motions on galaxy cluster abundance profiles*, *Mon. Not. Roy. Astron. Soc.* **359** (2005) 1041–1048, [astro-ph/0501141].

[139] P. Rebusco, E. Churazov, H. Boehringer, and W. Forman, *Effect of turbulent diffusion on iron abundance profiles*, *Mon. Not. Roy. Astron. Soc.* **372** (2006) 1840–1850, [astro-ph/0608491].

[140] M. S. Longair, *High energy astrophysics*, vol. 2. 1994.

[141] N. Hurley-Walker et al., *GaLactic and Extragalactic All-sky Murchison Widefield Array (GLEAM) survey - I. A low-frequency extragalactic catalogue*, **464** (Jan., 2017) 1146–1167, [arXiv:1610.08318].

[142] M. Vollmann, V. Heesen, T. Shimwell, M. J. Hardcastle, M. Brüggen, G. Sigl, and H. Röttgering, *Radio constraints on dark matter annihilation in Canes Venatici I with LOFAR*, *arXiv e-prints* (Sep, 2019) arXiv:1909.12355, [arXiv:1909.12355].

[143] R. Braun et al. https://astronomers.skatelescope.org/wp-~content/uploads/2017/10/SKA-~TEL-~SKO-~0000818-~01_SKA1_Science_Perform.pdf, 2017.

[144] R. Ghara, T. R. Choudhury, and K. K. Datta, *21-cm signature of the first sources in the Universe: Prospects of detection with SKA*, *Mon. Not. Roy. Astron. Soc.* **460** (2016), no. 1 827–843, [arXiv:1511.07448].

[145] A. R. Thompson, J. M. Moran, and G. W. Swenson, *Interferometry and synthesis in radio astronomy*. 1986.

[146] R. Braun, T. L. Bourke, J. A. Green, E. Keane, and J. Wagg, *Advancing Astrophysics with the Square Kilometre Array*, *PoS* **AASKA14** (2015) 174.

[147] C. Power, C. Lagos, B. Qin, C. Baugh, D. Cunnama, J. Fu, H. Kim, C. Lacey, L. Li, D. Obreschkow, J. Wang, Y. Wang, and M. Zhu, *Galaxy Formation & Dark Matter Modelling in the Era of the Square Kilometre Array*, *PoS* **AASKA14** (2015) 133.

[148] S. Colafrancesco, M. Regis, P. Marchegiani, G. Beck, R. Beck, H. Zechlin, A. Lobanov, and D. Horns, *Probing the nature of Dark Matter with the SKA*, *PoS* **AASKA14** (2015) 100, [arXiv:1502.03738].

[149] S. J. Tingay et al., *The Murchison Widefield Array: The Square Kilometre Array Precursor at Low Radio Frequencies*, *Publications of the Astronomical Society of Australia* **30** (Jan., 2013) e007, [arXiv:1206.6945].

[150] H. T. Intema, P. Jagannathan, K. P. Mooley, and D. A. Frail, *The GMRT 150 MHz all-sky radio survey. First alternative data release TGSS ADR1*, **598** (Feb., 2017) A78, [arXiv:1603.04368].

[151] *Search for Supersymmetry at the high luminosity LHC with the ATLAS experiment*, Tech. Rep. ATL-PHYS-PUB-2014-010, CERN, Geneva, Jul, 2014.

[152] **CMS Collaboration** Collaboration, *Study of the Discovery Reach in Searches for Supersymmetry at CMS with 3000/fb*, Tech. Rep. CMS-PAS-FTR-13-014, CERN, Geneva, 2013.

[153] *Prospects for benchmark Supersymmetry searches at the high luminosity LHC with the ATLAS Detector*, Tech. Rep. ATL-PHYS-PUB-2013-011, CERN, Geneva, Sep, 2013.

[154] **CMS** Collaboration, A. M. Sirunyan et al., *Search for supersymmetry in multijet events with missing transverse momentum in proton-proton collisions at 13 TeV*, *Phys. Rev. D* **96** (2017), no. 3 032003, [arXiv:1704.07781].

[155] **ATLAS** Collaboration, M. Aaboud et al., *Search for squarks and gluinos in events with an isolated lepton, jets, and missing transverse momentum at $\sqrt{s} = 13$ TeV with the ATLAS detector*, *Phys. Rev.* **D96** (2017), no. 11 112010, [arXiv:1708.08232].

[156] K. Spekkens, B. S. Mason, J. E. Aguirre, and B. Nhan, *A Deep Search for Extended Radio Continuum Emission From Dwarf Spheroidal Galaxies: Implications for Particle Dark Matter*, *Astrophys. J.* **773** (2013) 61, [arXiv:1301.5306].

[157] G. Belanger, F. Boudjema, A. Pukhov, and A. Semenov, *MicrOMEGAs: A Program for calculating the relic density in the MSSM*, *Comput. Phys. Commun.* **149** (2002) 103–120, [hep-ph/0112278].

[158] G. Beck and S. Colafrancesco, *Multi-frequency search for Dark Matter: the role of HESS, CTA, and SKA*, *PoS* **HEASA2016** (2017) 010, [arXiv:1704.08029].

[159] **ATLAS** Collaboration, M. Aaboud et al., *Search for electroweak production of supersymmetric particles in final states with two or three leptons at* $\sqrt{s} = 13$ *TeV with the ATLAS detector*, *Eur. Phys. J. C* **78** (2018), no. 12 995, [arXiv:1803.02762].

[160] **CMS** Collaboration, A. M. Sirunyan et al., *Combined search for electroweak production of charginos and neutralinos in proton-proton collisions at* $\sqrt{s} =$ *13 TeV*, *JHEP* **03** (2018) 160, [arXiv:1801.03957].

[161] **ATLAS** Collaboration, M. Aaboud et al., *Search for additional heavy neutral Higgs and gauge bosons in the ditau final state produced in 36 fb*$^{-1}$ *of pp collisions at* $\sqrt{s} = 13$ *TeV with the ATLAS detector*, *JHEP* **01** (2018) 055, [arXiv:1709.07242].

[162] **XENON** Collaboration, E. Aprile et al., *First Dark Matter Search Results from the XENON1T Experiment*, *Phys. Rev. Lett.* **119** (2017), no. 18 181301, [arXiv:1705.06655].

[163] J. Harz, B. Herrmann, M. Klasen, K. Kovarik, and P. Steppeler, *Theoretical uncertainty of the supersymmetric dark matter relic density from scheme and scale variations*, *Phys. Rev.* **D93** (2016), no. 11 114023, [arXiv:1602.08103].

[164] M. Klasen, K. Kovarik, and P. Steppeler, *SUSY-QCD corrections for direct detection of neutralino dark matter and correlations with relic density*, *Phys. Rev.* **D94** (2016), no. 9 095002, [arXiv:1607.06396].

[165] B. C. Allanach, A. Djouadi, J. L. Kneur, W. Porod, and P. Slavich, *Precise determination of the neutral Higgs boson masses in the MSSM*, *JHEP* **09** (2004) 044, [hep-ph/0406166].

[166] **LHCb** Collaboration, R. Aaij et al., *Measurement of the* $B_s^0 \to \mu^+\mu^-$ *branching fraction and effective lifetime and search for* $B^0 \to \mu^+\mu^-$ *decays*, *Phys. Rev. Lett.* **118** (2017), no. 19 191801, [arXiv:1703.05747].

[167] **Belle-II** Collaboration, S. Sandilya, *Prospects for Rare Decays at Belle II*, *PoS* **CKM2016** (2017) 080, [arXiv:1706.01027].

[168] W. J. M. A. Hoecker. http://pdg.lbl.gov/2018/reviews/rpp2018-b̃rev-b̃g-b̃2-b̃muon-b̃anom-b̃mag-b̃moment.pdf, 2017.

[169] K. T. Chyży, M. Weżgowiec, R. Beck, and D. J. Bomans, *Magnetic fields in Local Group dwarf irregulars*, **529** (May, 2011) A94, [arXiv:1101.4647].

[170] A. Kar, S. Mitra, B. Mukhopadhyaya, and T. R. Choudhury, *Dark matter, extra-terrestrial gamma-rays and the MSSM: a viability study*, *JCAP* **1802** (2018), no. 02 045, [arXiv:1711.11477].

[171] A. Kar, S. Mitra, B. Mukhopadhyaya, and T. R. Choudhury, *Do astrophysical data disfavour the minimal supersymmetric standard model?*, arXiv:1711.09069.

[172] **Fermi-LAT** Collaboration, M. Ackermann et al., *The Fermi Galactic Center GeV Excess and Implications for Dark Matter*, *Astrophys. J.* **840** (2017), no. 1 43, [arXiv:1704.03910].

[173] M. Cirelli and M. Taoso, *Updated galactic radio constraints on Dark Matter*, *JCAP* **1607** (2016), no. 07 041, [arXiv:1604.06267].

[174] A. Kar, S. Mitra, B. Mukhopadhyaya, and T. R. Choudhury, *Can Square Kilometre Array phase 1 go much beyond the LHC in supersymmetry search?*, *Phys. Rev.* **D99** (2019), no. 2 021302(R), [arXiv:1808.05793].

[175] L. E. Strigari, J. S. Bullock, M. Kaplinghat, J. D. Simon, M. Geha, B. Willman, and M. G. Walker, *A common mass scale for satellite galaxies of the Milky Way*, *Nature* **454** (2008) 1096–1097, [arXiv:0808.3772].

[176] M. Geha, B. Willman, J. D. Simon, L. E. Strigari, E. N. Kirby, D. R. Law, and J. Strader, *The Least Luminous Galaxy: Spectroscopy of the Milky Way Satellite Segue 1*, *Astrophys. J.* **692** (2009) 1464–1475, [arXiv:0809.2781].

[177] T. Linden, S. Profumo, and B. Anderson, *The Morphology of the Galactic Dark Matter Synchrotron Emission with Self-Consistent Cosmic Ray Diffusion Models*, *Phys. Rev.* **D82** (2010) 063529, [arXiv:1004.3998].

[178] A. Kar, S. Mitra, B. Mukhopadhyaya, T. R. Choudhury, and S. Tingay, *Constraints on dark matter annihilation in dwarf spheroidal galaxies from low frequency radio observations*, arXiv:1907.00979.

[179] E. Storm, T. E. Jeltema, M. Splettstoesser, and S. Profumo, *Synchrotron Emission from Dark Matter Annihilation: Predictions for Constraints from Non-detections of Galaxy Clusters with New Radio Surveys*, *Astrophys. J.* **839** (2017), no. 1 33, [arXiv:1607.01049].

[180] F. Donato, N. Fornengo, D. Maurin, P. Salati, and R. Taillet, *Antiprotons in cosmic rays from neutralino annihilation*, **69** (Mar, 2004) 063501, [astro-ph/0306207].

[181] R. B. Wayth et al., *GLEAM: The GaLactic and Extragalactic All-Sky MWA Survey*, **32** (June, 2015) e025, [arXiv:1505.06041].

[182] M. L. M. Collins et al., *The Masses of Local Group Dwarf Spheroidal Galaxies: The Death of the Universal Mass Profile*, **783** (Mar., 2014) 7, [arXiv:1309.3053].

[183] M. G. Walker et al., *A Universal Mass Profile for Dwarf Spheroidal Galaxies?*, **704** (Oct., 2009) 1274–1287, [arXiv:0906.0341].

[184] M. Irwin and D. Hatzidimitriou, *Structural parameters for the Galactic dwarf spheroidals*, *MNRAS* **277** (Dec., 1995) 1354–1378.

[185] N. F. Martin, J. T. A. de Jong, and H.-W. Rix, *A Comprehensive Maximum Likelihood Analysis of the Structural Properties of Faint Milky Way Satellites*, **684** (Sept., 2008) 1075–1092, [arXiv:0805.2945].

[186] V. Belokurov et al., *Leo V: A Companion of a Companion of the Milky Way Galaxy?*, **686** (Oct., 2008) L83, [arXiv:0807.2831].

[187] V. Belokurov et al., *The discovery of Segue 2: a prototype of the population of satellites of satellites*, **397** (Aug., 2009) 1748–1755, [arXiv:0903.0818].

[188] R. J. Sault, P. J. Teuben, and M. C. H. Wright, *A Retrospective View of MIRIAD*, in *Astronomical Data Analysis Software and Systems IV* (R. A. Shaw, H. E. Payne, and J. J. E. Hayes, eds.), vol. 77 of *Astronomical Society of the Pacific Conference Series*, p. 433, 1995. astro-ph/0612759.

[189] L. E. Strigari, *Galactic searches for dark matter*, *Physics Reports* **531** (2013), no. 1 1 – 88. Galactic searches for dark matter.

[190] R. B. Wayth, S. J. Tingay, C. M. Trott, D. Emrich, M. Johnston-Hollitt, B. McKinley, B. M. Gaensler, A. P. Beardsley, T. Booler, B. Crosse, T. M. O. Franzen, L. Horsley, D. L. Kaplan, D. Kenney, M. F. Morales, D. Pallot, G. Sleap, K. Steele, M. Walker, A. Williams, C. Wu, I. H. Cairns, M. D. Filipovic, S. Johnston, T. Murphy, P. Quinn, L. Staveley-Smith, R. Webster, and J. S. B. Wyithe, *The Phase II Murchison Widefield Array: Design overview*, **35** (Nov., 2018) 33, [arXiv:1809.06466].

[191] A. Kar, S. Mitra, B. Mukhopadhyaya, and T. R. Choudhury, *Heavy dark matter particle annihilation in dwarf spheroidal galaxies: radio signals at the SKA telescope*, arXiv:1905.11426.

[192] J. A. R. Cembranos, [U+FFFD] De La Cruz-Dombriz, V. Gammaldi, and M. Méndez-Isla, *SKA-Phase 1 sensitivity for synchrotron radio emission from multi-TeV Dark Matter candidates*, arXiv:1905.11154.

[193] J. Reynoso-Cordova, O. Burgueño, A. Geringer-Sameth, A. X. Gonzalez-Morales, S. Profumo, and O. Valenzuela, *On the origin of the gamma-ray emission from Omega Centauri: Milisecond pulsars and dark matter annihilation*, arXiv:1907.06682.

[194] S. Henleywillis, A. M. Cool, D. Haggard, C. Heinke, P. Callanan, and Y. Zhao, *A Deep X-ray Survey of the globular cluster Omega Centauri*, **479** (Sep, 2018) 2834–2852, [arXiv:1803.04822].

[195] F. Abbate, A. Possenti, C. Tiburzi, W. van Straten, E. Barr, A. Ridolfi, and P. Freire, *Polarization study of the pulsars in the globular cluster 47 Tucanae*, in *MeerKAT Science: On the Pathway to the SKA*, p. 36, 2016.

[196] B. McKinley, S. J. Tingay, E. Carretti, S. Ellis, J. Bland-Hawthorn, R. Morganti, J. Line, M. McDonald, S. Veilleux, R. Wahl Olsen, M. Sidonio, R. Ekers, A. R. Offringa, P. Procopio, B. Pindor, R. B. Wayth, N. Hurley-Walker, G. Bernardi, B. M. Gaensler, M. Haverkorn, M. Kesteven, S. Poppi, and L. Staveley-Smith, *The jet/wind outflow in Centaurus A: a local laboratory for AGN feedback*, **474** (Mar, 2018) 4056–4072, [arXiv:1711.01751].

[197] C. Blanco and D. Hooper, *Constraints on decaying dark matter from the isotropic gamma-ray background*, **2019** (Mar., 2019) 019, [arXiv:1811.05988].

[198] R. Jansson and G. R. Farrar, *A New Model of the Galactic Magnetic Field*, **757** (Sep, 2012) 14, [arXiv:1204.3662].

[199] R. Jansson and G. R. Farrar, *The Galactic Magnetic Field*, **761** (Dec, 2012) L11, [arXiv:1210.7820].

[200] T. R. Jaffe, K. M. Ferrière, A. J. Banday, A. W. Strong, E. Orlando, J. F. Macías-Pérez, L. Fauvet, C. Combet, and E. Falgarone, *Comparing polarized*

synchrotron and thermal dust emission in the Galactic plane, **431** (May, 2013) 683–694, [arXiv:1302.0143].

[201] Planck Collaboration, A. Abergel, P. A. R. Ade, N. Aghanim, M. I. R. Alves, G. Aniano, M. Arnaud, M. Ashdown, J. Aumont, C. Baccigalupi, A. J. Band ay, R. B. Barreiro, J. G. Bartlett, E. Battaner, K. Benabed, A. Benoit-Lévy, et al., *Planck intermediate results. XVII. Emission of dust in the diffuse interstellar medium from the far-infrared to microwave frequencies*, **566** (Jun, 2014) A55, [arXiv:1312.5446].

[202] A. Waelkens, T. Jaffe, M. Reinecke, F. S. Kitaura, and T. A. Enßlin, *Simulating polarized Galactic synchrotron emission at all frequencies. The Hammurabi code*, **495** (Feb, 2009) 697–706, [arXiv:0807.2262].

[203] A. Albert, M. André, M. Anghinolfi, G. Anton, M. Ardid, J. J. Aubert, J. Aublin, B. Baret, S. Basa, B. Belhorma, V. Bertin, S. Biagi, M. Bissinger, J. Boumaaza, S. Bourret, M. Bouta, M. C. Bouwhuis, H. Brânzaş, R. Bruijn, J. Brunner, J. Busto, A. Capone, L. Caramete, J. Carr, S. Celli, M. Chabab, T. N. Chau, R. Cherkaoui El Moursli, T. Chiarusi, M. Circella, A. Coleiro, M. Colomer, R. Coniglione, H. Costantini, P. Coyle, A. Creusot, A. F. Díaz, G. de Wasseige, A. Deschamps, C. Distefano, I. Di Palma, A. Domi, C. Donzaud, D. Dornic, D. Drouhin, T. Eberl, I. El Bojaddaini, N. El Khayati, D. Elsässer, A. Enzenhöfer, A. Ettahiri, F. Fassi, P. Fermani, G. Ferrara, F. Filippini, L. Fusco, P. Gay, H. Glotin, R. Gozzini, R. Gracia Ruiz, K. Graf, C. Guidi, S. Hallmann, H. van Haren, A. J. Heijboer, Y. Hello, J. J. Hernández-Rey, J. Hößl, J. Hofestädt, G. Illuminati, C. W. James, M. de Jong, P. de Jong, M. Jongen, M. Kadler, O. Kalekin, U. Katz, N. R. Khan-Chowdhury, A. Kouchner, M. Kreter, I. Kreykenbohm, V. Kulikovskiy, R. Lahmann, R. Le Breton, D. Lefèvre, E. Leonora, G. Levi, M. Lincetto, D. Lopez-Coto, S. Loucatos, G. Maggi, J. Manczak, M. Marcelin, A. Margiotta, A. Marinelli, J. A. Martínez-Mora, R. Mele, K. Melis, P. Migliozzi, M. Moser, A. Moussa, R. Muller, L. Nauta, S. Navas, E. Nezri, C. Nielsen, A. Nuñez-Castiñeyra, B. O'Fearraigh, M. Organokov, G. E. Păvălaş, C. Pellegrino, M. Perrin-Terrin, P. Piattelli, C. Poirè, V. Popa, T. Pradier, L. Quinn, N. Rand azzo, G. Riccobene, A. Sánchez-Losa, A. Salah-Eddine, D. F. E. Samtleben, M. Sanguineti, P. Sapienza, F. Schüssler, M. Spurio, T. Stolarczyk, B. Strandberg, M. Taiuti, Y. Tayalati, T. Thakore, S. J. Tingay, A. Trovato, B. Vallage, V. Van Elewyck,

F. Versari, S. Viola, D. Vivolo, J. Wilms, D. Zaborov, A. Zegarelli, J. D. Zornoza, and J. Zúñiga, *Search for dark matter towards the Galactic Centre with 11 years of ANTARES data*, *Physics Letters B* **805** (June, 2020) 135439.

[204] A. Berlin and N. Blinov, *Thermal neutrino portal to sub-MeV dark matter*, *Phys. Rev. D* **99** (2019), no. 9 095030, [arXiv:1807.04282].

[205] B. Dutta, S. Ghosh, and J. Kumar, *A sub-GeV dark matter model*, *Phys. Rev. D* **100** (2019) 075028, [arXiv:1905.02692].

[206] L. A. Cavasonza, H. Gast, M. Krämer, M. Pellen, and S. Schael, *Constraints on leptophilic dark matter from the AMS-02 experiment*, *Astrophys. J.* **839** (2017), no. 1 36, [arXiv:1612.06634]. [Erratum: Astrophys.J. 869, 89 (2018)].

[207] M. Battaglieri et al., *US Cosmic Visions: New Ideas in Dark Matter 2017: Community Report*, in *U.S. Cosmic Visions: New Ideas in Dark Matter*, 7, 2017. arXiv:1707.04591.

[208] T. R. Slatyer and C.-L. Wu, *General Constraints on Dark Matter Decay from the Cosmic Microwave Background*, *Phys. Rev. D* **95** (2017), no. 2 023010, [arXiv:1610.06933].

[209] H. Poulter, Y. Ali-Haïmoud, J. Hamann, M. White, and A. G. Williams, *CMB constraints on ultra-light primordial black holes with extended mass distributions*, arXiv:1907.06485.

[210] S. Clark, B. Dutta, Y. Gao, L. E. Strigari, and S. Watson, *Planck Constraint on Relic Primordial Black Holes*, *Phys. Rev. D* **95** (2017), no. 8 083006, [arXiv:1612.07738].

[211] B. Carr, F. Kuhnel, and M. Sandstad, *Primordial Black Holes as Dark Matter*, *Phys. Rev. D* **94** (2016), no. 8 083504, [arXiv:1607.06077].

[212] B. Dasgupta, R. Laha, and A. Ray, *Neutrino and positron constraints on spinning primordial black hole dark matter*, *Phys. Rev. Lett.* **125** (2020), no. 10 101101, [arXiv:1912.01014].

[213] **COMPTEL** Collaboration, V. Schoenfelder, *The first comptel source catalogue*, *Astron. Astrophys. Suppl. Ser.* **143** (2000) 145, [astro-ph/0002366].

[214] **INTEGRAL** Collaboration, W. Hermsen and C. Winkler, *The INTEGRAL Mission*, in *22nd Moriond Astrophysics Meeting: The Gamma Ray Universe*, (Hanoi), pp. 393–400, The Gioi, 2002.

[215] M. Cirelli, N. Fornengo, B. J. Kavanagh, and E. Pinetti, *Integral X-ray constraints on sub-GeV Dark Matter*, arXiv:2007.11493.

[216] R. Bartels, D. Gaggero, and C. Weniger, *Prospects for indirect dark matter searches with MeV photons*, *JCAP* **05** (2017) 001, [arXiv:1703.02546].

[217] S. Colafrancesco, P. Marchegiani, and G. Beck, *Evolution of Dark Matter Halos and their Radio Emissions*, *JCAP* **02** (2015) 032, [arXiv:1409.4691].

[218] A. Caputo, C. P. Garay, and S. J. Witte, *Looking for Axion Dark Matter in Dwarf Spheroidals*, *Phys. Rev. D* **98** (2018), no. 8 083024, [arXiv:1805.08780]. [Erratum: Phys.Rev.D 99, 089901 (2019)].

[219] A. Ghosh, A. Kar, and B. Mukhopadhyaya, *Search for decaying heavy dark matter in an effective interaction framework: a comparison of γ-ray and radio observations*, *JCAP* **09** (2020) 003, [arXiv:2001.08235].

[220] S. W. Hawking, *Black hole explosions?*, **248** (Mar., 1974) 30–31.

[221] M. Boudaud and M. Cirelli, *Voyager 1 $e^{\pm}$ Further Constrain Primordial Black Holes as Dark Matter*, *Phys. Rev. Lett.* **122** (2019), no. 4 041104, [arXiv:1807.03075].

[222] **e-ASTROGAM** Collaboration, M. Tavani et al., *Science with e-ASTROGAM: A space mission for MeV–GeV gamma-ray astrophysics*, *JHEAp* **19** (2018) 1–106, [arXiv:1711.01265].

[223] F. Halzen, B. Keszthelyi, and E. Zas, *Neutrinos from primordial black holes*, *Phys. Rev. D* **52** (1995) 3239–3247, [hep-ph/9502268].

[224] J. H. MacGibbon and B. R. Webber, *Quark- and gluon-jet emission from primordial black holes: The instantaneous spectra*, *Phys. Rev. D* **41** (May, 1990) 3052–3079.

[225] **MAGIC** Collaboration, J. Aleksic et al., *Searches for Dark Matter annihilation signatures in the Segue 1 satellite galaxy with the MAGIC-I telescope*, *JCAP* **06** (2011) 035, [arXiv:1103.0477].

[226] J. Lavalle, D. Maurin, and A. Putze, *Direct constraints on diffusion models from cosmic-ray positron data: Excluding the minimal model for dark matter searches*, *Phys. Rev. D* **90** (2014) 081301, [arXiv:1407.2540].

[227] G. Ballesteros, J. Coronado-Blázquez, and D. Gaggero, *X-ray and gamma-ray limits on the primordial black hole abundance from Hawking radiation*, *Phys. Lett. B* **808** (2020) 135624, [arXiv:1906.10113].

[228] R. Laha, *Primordial Black Holes as a Dark Matter Candidate Are Severely Constrained by the Galactic Center 511 keV γ -Ray Line*, *Phys. Rev. Lett.* **123** (2019), no. 25 251101, [arXiv:1906.09994].

[229] **AMEGO** Collaboration, R. Caputo et al., *All-sky Medium Energy Gamma-ray Observatory: Exploring the Extreme Multimessenger Universe*, arXiv:1907.07558.

[230] T. Aramaki, P. Hansson Adrian, G. Karagiorgi, and H. Odaka, *Dual MeV Gamma-Ray and Dark Matter Observatory - GRAMS Project*, *Astropart. Phys.* **114** (2020) 107–114, [arXiv:1901.03430].

[231] **SENSEI** Collaboration, L. Barak et al., *SENSEI: Direct-Detection Results on sub-GeV Dark Matter from a New Skipper-CCD*, arXiv:2004.11378.

[232] R. Essig, J. Pradler, M. Sholapurkar, and T.-T. Yu, *Relation between the Migdal Effect and Dark Matter-Electron Scattering in Isolated Atoms and Semiconductors*, *Phys. Rev. Lett.* **124** (2020), no. 2 021801, [arXiv:1908.10881].

[233] B. Dutta, D. Kim, S. Liao, J.-C. Park, S. Shin, and L. E. Strigari, *Dark matter signals from timing spectra at neutrino experiments*, *Phys. Rev. Lett.* **124** (2020), no. 12 121802, [arXiv:1906.10745].

[234] **MiniBooNE DM** Collaboration, A. Aguilar-Arevalo et al., *Dark Matter Search in Nucleon, Pion, and Electron Channels from a Proton Beam Dump with MiniBooNE*, *Phys. Rev. D* **98** (2018), no. 11 112004, [arXiv:1807.06137].

[235] D. Banerjee et al., *Dark matter search in missing energy events with NA64*, *Phys. Rev. Lett.* **123** (2019), no. 12 121801, [arXiv:1906.00176].

[236] **LDMX** Collaboration, T. Akesson et al., *Light Dark Matter eXperiment (LDMX)*, arXiv:1808.05219.

[237] M. Escudero, *Neutrino decoupling beyond the Standard Model: CMB constraints on the Dark Matter mass with a fast and precise $N_{\rm eff}$ evaluation*, *JCAP* **02** (2019) 007, [arXiv:1812.05605].

Thesis Highlight

Name of the Student: Arpan Kar

Name of the CI/OCC: Harish-Chandra Research Institute, Prayagraj

Enrolment No.: PHYS08201504001

Thesis Title: Dark matter and new fundamental physics

Discipline: Physical Sciences **Sub-Area of Discipline:** High Energy Physics Phenomenology

Date of viva voce: 14.07.2021

While existing direct search and collider experiments have not yet found any signature of a dark matter (DM) candidate and thus impose constraints on its microscopic properties, I show in my thesis that the indirect search of DM based on the observation of radio signals which are induced by $e^{\pm}$ generated from DM initiated processes inside galaxies or galaxy clusters may become an alternative avenue for unveiling the nature of DM. I find that the Square Kilometre Array (SKA), mostly with 100 hours of observation, should be able to detect radio synchrotron signals of minimal supersymmetric standard model (MSSM) DM annihilation, for cases where the superparticle masses are well above the reach of the LHC. This observation holds even for conservative values of astrophysical parameters, and thus underscores a new potential of the SKA. I show that the enhancement of trans-TeV DM induced radio signals is possible mainly due to: (a) abundance of energetic $e^{\pm}$ in the annihilation spectra of heavier DM particles, (b) dominant annihilation to a pair of bottom quarks and (c) a sizable annihilation rate. Simultaneously, effects of various astrophysical parameters (e.g., magnetic field (B), diffusion (D0)) on radio synchrotron signals produced from the annihilation of trans-TeV DM particles have been studied in detail. In addition to these, I use the Murchison Widefield Array (MWA) radio telescope data to constrain DM annihilation in 14 dwarf spheroidal (dSph) galaxies. I find that, for μG level B-fields in dSphs, MWA I data provide constraints that are comparable to existing limits from gamma-ray and cosmic-ray observations; however, MWA II can give better constraints for a large region of the DM parameter space extended from a few GeV DM mass to a DM mass which is at the TeV scale. I also use the MWA I data on the globular cluster ω Cen as well as its γ-ray observation by Fermi-LAT to constrain the astrophysical parameter space (i.e. B – D0 plane) in ω Cen. Through this analysis, I show that the current MWA data can already provide significant limits on model parameters and thus improves the prospects for understanding various astrophysical parameters in galactic objects such as ω Cen. Apart from these, I study the prospects of constraining the MeV DM particles and primordial black holes (PBHs) at the upcoming SKA telescope. By comparing the SKA limits with existing indirect detection bounds (e.g., Planck's CMB constraints) on MeV DM and PBH DM abundance, I find that, even for conservative choices of D0 in dSphs, the SKA can provide better probe for MeV DM particle with masses up to few tens of MeV and for PBHs with masses that are above a factor times 10^{15} to 10^{17} g. In parallel, I show that these SKA limits, even independently of D0, can be stronger than those predicted by future MeV γ-ray experiments. Additionally, regions in the diffusion parameter space of MeV $e^{\pm}$ (produced from MeV DM or PBHs) inside a dSph, that give rise to observable signals at the SKA are also marked out.